

Design of Nanostructured Vanadium Pentoxide Scaffolds Inspired by Natural Cuttlebone

Von der Fakultät Chemie der Universität Stuttgart zur
Erlangung der Würde eines Doktors der
Naturwissenschaften (Dr. rer. nat.) genehmigte
Abhandlung

Vorgelegt von
Andrea Knöller
aus Stuttgart

Hauptberichter: Prof. Dr. Joachim Bill
Mitberichter: Prof. Dr. Siegfried Schmauder
Prüfungsvorsitzender: Prof. Dr. Thomas Schleid

Tag der mündlichen Prüfung: 29. Januar 2018

Institut für Materialwissenschaft
Universität Stuttgart

2018

dedicated to my family

Declaration of Authorship

I hereby certify that the dissertation entitled

“Design of Nanostructured Vanadium Pentoxide Scaffolds Inspired by Natural Cuttlebone”

is entirely my own work except where otherwise indicated. Passages and ideas from other sources have been clearly indicated.

Name: _____

Signature: _____

Date: _____

Publications

This thesis was supervised by Prof. Dr. Joachim Bill and Dr. Žaklina Burghard at the Institute for Materials Science of the University of Stuttgart. The experimental work resulted in two scientific publications, which were prepared in collaboration with scientists from the Max-Planck-Institute for Solid State Research (MPI-FKF) in Stuttgart and the Department of Chemistry of the University of California, Berkeley as well as with contributions from colleagues of the Institute for Materials Science in Stuttgart.

- A Knöller, T Runčevski, RE Dinnebier, J Bill, and Z Burghard. Cuttlebone-like V_2O_5 nanofibre scaffolds - advances in structuring cellular solids. *Scientific Reports*, 7:42951 (2017).

<https://www.nature.com/articles/srep42951>

(TR and RED provided the XRPD measurements)

- A Knöller, S Kilper, AM Diem, M Widenmeyer, T Runčevski, RE Dinnebier, J Bill, and Z Burghard. Ultrahigh damping capacities in lightweight structural materials. *Nano Letters*, (2018).

<https://pubs.acs.org/articlesonrequest/AOR-4gJGC32yvcJjQJDxWTNS>

(SK was involved in programming the damping test method, AMD helped with *in situ* SEM investigations, MW conducted the TGA/DSC measurements, TR and RED provided the XRPD measurements)

This thesis has a noncumulative style. The content of the first publication is implemented in the sections 5.1 and 5.2, while the content of the second publication is implemented in the sections 5.3 and 5.4.

Further related publications:

- A Knöller, CP Lampa, F von Cube, TH Zeng, DC Bell, MS Dresselhaus, Z Burghard, and J Bill. Strengthening of ceramic-based artificial nacre *via* synergistic interactions of 1D vanadium pentoxide and 2D graphene oxide building blocks. *Scientific Reports*, 7:40999, (2017).
- B Wicklein, AM Diem, A Knöller, MS Cavalcante, L Bergström, J Bill, and Z Burghard. Dual-fiber approach towards flexible multifunctional hybrid materials. *Advanced Functional Materials*, 170427 (2017).
- AM Diem, A Knöller, Z Burghard, and J Bill. Free-Standing Nanostructured Vanadium Pentoxide Films for Metal-Ion Batteries. *in preparation*
- TH Jahnke, A Knöller, S Kilper, M Widenmeyer, Z Burghard, and J Bill. Coalescence in hybrid materials - the key to high capacity electrodes. *in preparation*

Contents

1	Abstract	1
2	Zusammenfassung	5
3	Introduction	9
3.1	Bioinspiration	9
3.2	Vanadium Pentoxide	11
3.3	Fabricating Porous Materials	15
3.4	Mechanical Properties of Porous Materials	16
3.5	Mechanical Damping	19
3.6	Fundamental Techniques	21
3.6.1	Atomic Force Microscopy	21
3.6.2	Scanning Electron Microscopy	21
3.6.3	Brunauer-Emmett-Teller	22
3.6.4	Optical Dilatometry	22
3.6.5	Thermogravimetric Analysis	23
3.6.6	Differential Scanning Calorimetry	23
3.6.7	X-Ray Powder Diffraction	24
4	Experimental Part	25
4.1	Scaffold Fabrication	25
4.1.1	Synthesis of the V_2O_5 Nanofibers	25
4.1.2	Fabrication of the Molds	26
4.1.3	Ice-Templating	26
4.1.4	Drying	28
4.1.5	Post-Treatment	28
4.1.6	Natural Cuttlebone and Polyurethane Foams	29
4.2	Scaffold Characterization	30
4.2.1	Structural and Compositional Investigation	30

4.2.2	Mechanical Investigation	33
4.2.3	Contributions	35
5	Results and Discussion	37
5.1	Natural Cuttlebone	37
5.2	Cuttlebone-like V_2O_5 Scaffolds	40
5.2.1	V_2O_5 Nanofiber Building Blocks	40
5.2.2	Ice-Templating of V_2O_5 Nanofibers	42
5.2.3	Artificial Cuttlebone	48
5.2.4	Structure-Mechanics Relation	53
5.3	Towards All-Ceramic Scaffolds	59
5.3.1	Thermal Stability	59
5.3.2	Phase Transformation	61
5.3.3	Phase Pure V_2O_5 Scaffolds	64
5.4	Dynamic Mechanical Behavior	66
5.4.1	Elastic Deformation	66
5.4.2	Damping of PU foams	70
5.4.3	Damping of V_2O_5 Scaffolds	73
5.4.4	Assessment of Damping Capacities	80
6	Conclusion	83
	Bibliography	85
	Danksagung	101

List of Abbreviations and Symbols

A	Cross-section area
AFM	Atomic force microscopy
BET	Brunauer-Emmett-Teller
C_2	Constant (= 1)
C_7	Constant (= 0.65)
d	Interlayer distance
D_0	Dissociation energy
E	Young's modulus
E'	Storage modulus
E''	Loss modulus
E_s	Young's modulus of the cell walls
$\frac{E}{E_s}$	Relative Young's modulus
δ	Phase angle
DSC	Differential scanning calorimetry
ϵ	Strain
H-bond	Hydrogen bond
l	Height
L	Load
λ	Wavelength
LIB	Lithium-ion battery
n	Diffraction order
n	Water fraction
P	Porosity
PBS	Phosphate-buffered saline
PU	Polyurethane
PVP	Polyvinylpyrrolidone

θ	Diffraction angle
ρ	Density (of the scaffold)
ρ_s	Density of the cell walls
$\frac{\rho}{\rho_s}$	Relative density
σ	Stress
σ_f	Modulus of rupture
σ_{f*}	Crushing strength
SEM	Scanning electron microscopy
t	Time
T	Temperature
T_H	Homologous temperature
T_s	Melting temperature
$\tan \delta$	Loss factor
TGA	Thermogravimetric analysis
V_2O_5	Vanadium pentoxide
XRPD	X-ray powder diffraction

1 Abstract

Ceramics are widely used functional materials for various applications, such as catalysis, sensing and energy storage. For these purposes, ceramics need to exhibit a high surface area and good permeability for atoms and/or molecules, both of which can be achieved through the fabrication of porous microstructures. However, an increased porosity usually comes along with a reduced mechanical stability. Additionally, the poor toughness of ceramics increases the risk of abrupt failure, when being exposed to mechanical stresses. These characteristics can dramatically shorten the ceramics' functional lifetime. The necessity to enhance the ceramics' mechanical performance, thus their lifetime, triggers scientists to take a look at nature. Biological structures evolved over billions of years and brought their mechanical performance to perfection. Therefore, learning from nature's structural design principles and transferring them to artificial systems, can help developing functional materials with exceptional mechanical performance.

One interesting biological role model is cuttlebone, the buoyancy tank found in cuttlefish (sepia). It unites ultrahigh porosity (93%) with an extraordinary mechanical stability (compressive strength of about 1 MPa), a truly remarkable achievement for these two properties with opposing trends. The key to this unique combination is a hierarchical assembly of aragonite (CaCO_3) fibers and a small fraction of organic phase into a lamellar microstructure. The lamellas are mechanically supported by a regular array of interconnecting pillars. Interestingly, even though the microstructure is highly anisotropic, the mechanical stability behaves predominantly direction independent. The latter is crucial for the cuttlefish, as it has to resist the hydrostatic pressure, which arises from the surrounding water.

Cuttlebone is known for about 180 years, but only in recent years it started attracting the attention of the scientific community. While mainly investigating its formation, structure and mechanical properties is in the focus of current research, there is only limited work done, which addresses mimicking its sophisticated microstructure. This dissertation contributes to the development of functional ceramics, which exhibit a cuttlebone-inspired microstructure, using vanadium pentoxide (V_2O_5) nanofibers as building blocks. V_2O_5 is a versatile functional material for the application in the fields of catalysis, sensing and energy storage. Moreover, it can be synthesized in various shapes and dimensions, opening a variety of structuring possibilities. The highly porous cuttlebone-inspired V_2O_5 scaffolds are obtained through a multi-step process, involving the synthesis of V_2O_5 nanofibers, the structuring *via* ice-templating, the subsequent drying and thermal post-treatment.

The sol-gel-derived ribbon-like V_2O_5 nanofibers of high aspect ratio exhibit a layered structure with intercalated water molecules. Furthermore, the oxygen-containing functional groups on the nanofibers' surface render their homogeneous dispersability in aqueous solutions, hence making these colloidal suspensions suitable for ice-templating. To this end, the V_2O_5 nanofiber suspension is shock frozen with liquid nitrogen, such that the formed plate-like ice crystals serve as templates for the assembly of the nanofibers. Subsequent drying results in self-supporting scaffolds, whose microstructure closely resembles that of cuttlebone, albeit with much smaller dimensions. In this manner, artificial ceramic scaffolds with a porosity of up to 99.8% become accessible. This ultrahigh porosity significantly outperforms that of natural cuttlebone (93%). Compression tests revealed that the cuttlebone-like structure imparts a better mechanical stability in comparison to V_2O_5 scaffolds with a random microstructure. Moreover, tuning the cuttlebone-like microstructure through the initial V_2O_5 nanofiber concentration allows further enhancing the mechanical stability even further, so that it approaches the wall modulus of cuttlebone. In addition, it could be demonstrated that thermal treatment of the V_2O_5 scaffolds allows to remove the intercalated water and preserves their microstructure as well as a comparable mechanical performance.

The use of the V_2O_5 nanofibers as scaffold constituents opens new opportunities for tailoring the mechanical characteristics. In particular, owing to their small

size (in the nanometer range) and high aspect ratio, these nanofibers have a pronounced mechanical flexibility, which upon assembly is not only preserved, but transferred to the macroscopic level. Dynamic mechanical measurements show a reversible deformation up to about 3%, which is unusually high for ceramic materials. Investigation of the underlying deformation mechanisms by a SEM-based *in situ* mechanical deformation technique revealed a cell wall buckling similar to what is found in polyurethane foams, which find widespread use due to their high damping capacity for mechanical vibrations. Comparative damping measurements evidenced that the viscoelastic properties of the V_2O_5 scaffolds are very similar to those of polyurethane foams, and depending on their microstructure, thermal treatment, compressive strain and applied frequency, the V_2O_5 scaffolds reach a loss factor $\tan \delta$ of up to 0.47, even outperforming polyurethane foams by up to 300 %.

The developed novel fabrication scheme enables the simultaneous implementation of ultrahigh porosity, improved mechanical stability and excellent vibration resistance into ceramic-based materials. Thus the obtained V_2O_5 scaffolds are of great potential for applications in catalysis, sensing and energy storage, where mechanical stability is an essential requirement. In addition, the achievements of this work provide useful guidelines for the design of a wide range of mechanically stable and vibration-resistant functional materials.

2 Zusammenfassung

Funktionskeramiken finden in vielen Bereichen, z.B. der Katalyse, Sensorik und Energiespeicherung, Anwendung. Hierfür sind eine große spezifische Oberfläche und gute Permeabilität des Materials für Atome und/oder Moleküle unerlässlich. Beides kann durch die Herstellung von porösen Strukturen erreicht werden, jedoch geht eine Erhöhung der Porosität in der Regel mit einer Verringerung der mechanischen Stabilität einher. Zudem sind Keramiken sehr spröde und können abrupt brechen, wenn sie mechanischen Belastungen ausgesetzt sind, wodurch sich die Lebensdauer der keramischen Funktionsmaterialien verringert. Um die mechanische Stabilität und damit auch die Lebensdauer zu verbessern, lohnt es sich, einen Blick in die Natur zu werfen. Über Milliarden von Jahren hat die Evolution biologische Materialien hervorgebracht, die aufgrund ihres raffinierten Designs einzigartige mechanische Eigenschaften aufweisen. Aus diesem kann die Erforschung biologischer Bauprinzipien die Entwicklung von beständigen Funktionskeramiken vorantreiben.

Eines dieser biologischen Materialien ist die natürliche Sepiaschale (Schulp). Dabei handelt es sich um das Auftriebsorgan in Tintenfischen (Sepia). Die Sepiaschale zeichnet sich durch eine extrem hohe Porosität (93 %) aus und besitzt dennoch eine exzellente mechanische Stabilität (Druckfestigkeit: 1 MPa). Es ist diese Kombination zweier gegenläufiger Eigenschaften, welche für die Entwicklung von Funktionskeramiken für die Katalyse, Sensorik und Energiespeicherung von Interesse sind. Diese Kombination erreicht die Sepiaschale durch die hierarchische Organisation von Aragonitfasern gemeinsam mit einem geringen Anteil einer organischer Phase in eine lamellare Mikrostruktur. Die Lamellen sind zudem durch eine Vielzahl an regelmäßig angeordneten Säulen miteinander verbunden. Angesichts der ausgeprägten anisotropen Mikrostruktur der Sepiaschale ist es bemerkenswert, dass ihre mechanische Stabilität nahezu richtungsunabhängig ist. Dieses Merkmal ist für das Überleben des Tintenfisches

äußerst wichtig, da er stets dem hydrostatischen Druck des umgebenden Wassers ausgesetzt ist.

Vor ca. 180 Jahren wurde die Sepiaschale bereits in der Literatur erwähnt, doch erst in den letzten Jahren findet sie in der Naturwissenschaft stärkere Beachtung. Standen bisher vor allem die Entstehung der Sepiaschale, sowie ihre Struktur und mechanischen Eigenschaften im Vordergrund, so wurde die Übertragung der gewonnenen Erkenntnisse auf künstliche Materialsysteme nur ansatzweise verfolgt. Diese Dissertation leistet ihren Forschungsbeitrag im Bereich bioinspirierter Materialien durch die Entwicklung der künstliche Sepiaschale aus V_2O_5 -Nanofasern. Vanadiumpentoxid (V_2O_5) ist eine vielseitig nutzbare Funktionskeramik, die in der Katalyse, Sensorik und Energiespeicherung Einsatz findet. Darüber hinaus können aus diesem Oxid unterschiedliche Arten von nanostrukturierten Materialien gewonnen werden. Dies wurde in der vorliegenden Arbeit ausgenutzt, um gezielt hochporöse Sepiaschalen ähnliche V_2O_5 -Gerüste herzustellen. Der hierfür entwickelte mehrstufige Prozess umfasst die Synthese der V_2O_5 -Nanofasern, deren Strukturierung mittels Ice-Templating und schließlich die Trocknung und thermische Nachbehandlung des gewonnenen Materials.

Die durch ein Sol-Gel-Verfahren synthetisierten bänderartigen V_2O_5 -Nanofasern weisen einen sehr hohen Formfaktor und eine schichtartige Struktur mit eingelagerten Wassermolekülen auf. Darüber hinaus befinden sich auf der Oberfläche der Nanofasern zahlreiche funktionelle Gruppen, welche die Nanofasern gut in Wasser dispergierbar und somit für das Ice-Templating zugänglich machen. Für letzteres wird eine wässrige V_2O_5 -Nanofaser-Suspension durch flüssigen Stickstoff schnell eingefroren, wobei die sich bildenden Eiskristalle als strukturgebende Template für die Nanofasern fungieren. Anschließendes Trocknen führt zu mechanisch stabilen Gerüsten, die ähnlich wie die Sepiaschale aufgebaut sind, jedoch mit deutlich kleineren Strukturabmessungen und einer Porosität von bis zu 99,8%. Damit übertrifft die Porosität der V_2O_5 -Gerüste die der Sepiaschale (93%) noch deutlich. Beim Ausüben von mechanischem Druck auf die V_2O_5 -Gerüste führt die Sepiaschalen ähnliche Anordnung der Nanofasern zu einer im Vergleich zu regellos angeordneten V_2O_5 -Gerüsten wesentlich höheren mechanischen Stabilität. Diese kann durch Erhöhung der anfänglichen Konzentration der kolloidalen V_2O_5 -Nanofaser-Suspension noch weiter gesteigert wer-

den, wobei fast der E-Modul der Zellwände der Sepiaschale erreicht wird. Die im letzten Schritt durchgeführte thermische Nachbehandlung entfernt das interkalierte Wasser unter Bewahrung sowohl der Mikrostruktur als auch der mechanischen Eigenschaften des Gerüsts.

Die V_2O_5 -Nanofasern bieten ferner Zugang zu Materialsystemen, die über die reine Nachahmung der natürlichen Sepiaschale hinausgehen. Aufgrund ihres geringen Querschnitts (im Nanometerbereich) und dem hohen Formfaktor weisen die V_2O_5 -Nanofasern eine beachtliche mechanische Flexibilität auf. Beim Zusammenschluss der Nanofasern während dem Ice-Templating überträgt sich diese Flexibilität auf die makroskopische Struktur. Dynamische Druckversuche zeigen, dass die V_2O_5 -Gerüste bis zu 3% reversibel verformbar sind, ein Ausmaß, welches für Keramiken sehr beachtlich ist. Die hohe Verformbarkeit kann durch *in situ* REM Untersuchungen direkt veranschaulicht werden. Dabei tritt ein ähnlicher Deformationsmechanismus wie in Polyurethanschäumen zutage, ein Material, da für seine guten Dämpfungseigenschaften und exzellente Vibrationsbeständigkeit bekannt ist. Vergleichende Dämpfungsmessungen ergaben bessere Eigenschaften der V_2O_5 -Gerüste gegenüber den Polyurethanschäumen. So erreichen erstere in Abhängigkeit von der Mikrostruktur, der thermischen Nachbehandlung und der Kompression der Gerüste sowie der angelegten Frequenz einen Verlustfaktor $\tan \delta$ von bis zu 0,47, womit sie die gemessenen Verlustfaktoren der Polyurethanschäume um bis zu 300% übertreffen.

Der neue Herstellungsprozess gestattet es den in V_2O_5 -Gerüsten extrem hoher Porosität, verbesserte mechanischer Stabilität und exzellente Vibrationsbeständigkeit zu vereinen. Die Sepiaschalen ähnlichen V_2O_5 basierten Strukturen besitzen großes Anwendungspotential als haltbare Bauelemente in der Katalyse, Sensorik und Energiespeicherung. Die in dieser Arbeit gewonnenen Erkenntnisse sollten sich auch auf andere Systeme übertragen lassen, sodass diese Arbeit als Leitschnur für die Entwicklung unterschiedlicher poröser, mechanisch stabiler und vibrationsbeständiger Funktionsmaterialien dienen kann.

3 Introduction

3.1 Bioinspiration

Nature provides mankind with a diversity of biological systems that can help developing functional materials with an exceptional combination of properties. In this scope, the field of bioinspired structuring focuses on the transfer of biological design principles to artificial systems. One of the most prominent examples of natural role models in this field is nacre, the iridescent layer found in numerous mollusk shells.^[1–5] Its structural design, composed of hard aragonite (CaCO_3) platelets (95 %) embedded in a small fraction of soft biopolymer (5 %), enables excellent shock-resistance. This so-called "brick-and-mortar" structure of the two components promotes crack deflection along the interfaces, while a solid ceramic block would abruptly fail (figure 3.1). Such a hierarchical microstructure therefore yields a unique combination of high stiffness (Young's modulus of 60-70 GPa)^[1] and good resilience (fracture toughness of about $7 \text{ MPa m}^{1/2}$).^[2] The latter outperforms the fracture toughness of monolithic aragonite by 20-30 times.^[6] In addition, the small size of nacre's building blocks (the thickness of the aragonite plates is in the range of a few hundred nanometers) makes this biomaterial more insensitive to flaws,^[7] proving the sophistication of nature's design. The investigation of nacre and other biomaterials helps identifying the key design principles crucial to achieve a unique combination of mechanical properties.^[3,8] These principles rely on the composition and structural organization, in particular (i) on the combination of hard and soft materials (different Young's moduli), (ii) the use of nanostructures with high aspect ratio (platelets or fibers), (iii) a well-defined composition as well as (iv) on their hierarchical assembly into a sophisticated microstructure. Applying these principles yields man-made ceramic-based materials with exceptional mechanical performance.^[4,9]

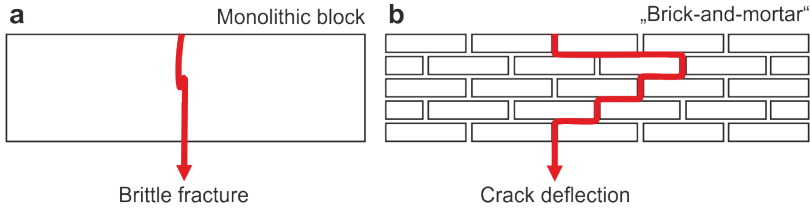


Figure 3.1: Schematics of (a) straight crack propagation through a monolithic ceramic block and (b) crack deflection in natural nacre due to the "brick-and-mortar" assembly of aragonite platelets embedded in an organic phase.

The example above shows that a defined structuring can give rise to remarkable combinations of properties, inspiring the materials science community to investigate further biological systems, such as wood^[10] or bone.^[11,12] These systems belong to the category of cellular solids, which unite high stiffness and strength with low weight.^[13] Another interesting cellular biomaterial is natural cuttlebone, the aragonite-based buoyancy tank in cuttlefish (*sepia officinalis*, figures 3.2a,b).^[14–18] It consists of two parts, the dorsal shield, which covers the top of the bone, and the internal lamellar matrix. While the dorsal shield is thick and dense, the lamellar matrix is porous. Among natural cellular solids, cuttlebone's lamellar matrix stands out due to an ultrahigh porosity of 93%,^[14] outperforming most other porous biomaterials, including wood^[10] (<70%) or even bone^[11,12] (<79%). It achieves its high porosity coupled with a remarkable mechanical stability through the sophisticated hierarchical organization of the building blocks it is composed of. Micrometer-sized aragonite fibers with different dimensions and orientations^[18] as well as about 4.5 wt.% of organic matter^[14] are assembled into ceramic-based, regularly stacked lamellas (also called septa), as depicted in the high magnification photograph of figure 3.2c. Closer inspection using SEM (figure 3.2d) revealed that the lamellas are several micrometers in thickness and several hundreds of micrometers apart from each other. Evenly distributed pillars bridge these gaps, and connect the neighboring lamellas, therefore serve as mechanical support. It should be mentioned that depending on the sepia species, the cuttlebone's size (also the size of the structural features) and density varies. Downscaling the size and lamella distance as well as increasing the density, tend to enhance the stability,^[17] thus allowing some species to live in greater depths than others.^[15] In case of the *sepia officinalis*, a microstructure as displayed in figure 3.2d results in a compressive strength of

about 1 MPa at 93% porosity.^[14] The combination of materials and the defined structuring (analog to the identified key design principles introduced for natural nacre) therefore enables the highly porous natural cuttlebone to resist great external pressures. Even though this biomaterial has great potential to serve as natural role model in the field of bioinspired structuring, the realization of man-made cuttlebone-like structures is to date rarely achieved.^[19]

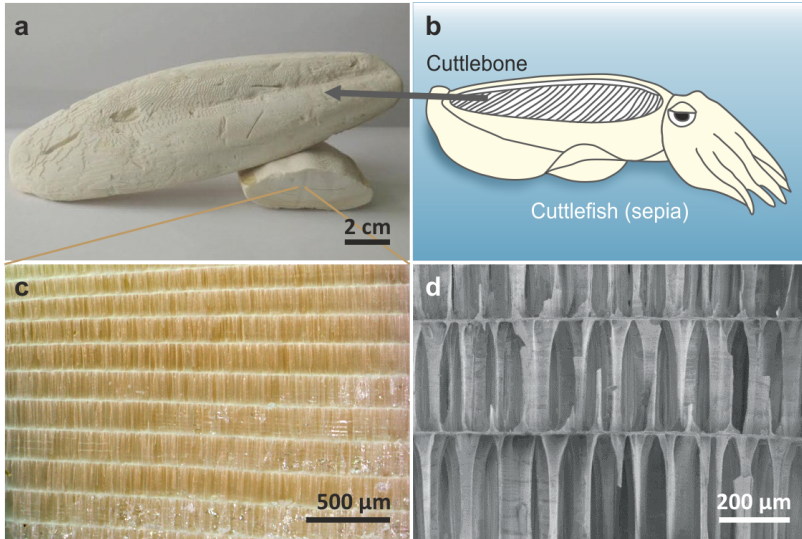


Figure 3.2: (a) Photograph of natural cuttlebone (*sepia officinalis*), which is (b) the buoyancy tank in cuttlefish, also known as sepia. The drawing is adapted from the draft of Birchall and Thomas.^[14] (c) Photograph (by Sven Schildt) and (d) SEM image of cuttlebone's microstructure, revealing lamellas and interconnecting pillars. (d) is adapted and reprinted with permission from Knöller *et al.*^[20] Copyright 2017, Springer Nature.

3.2 Vanadium Pentoxide

Copying the microstructure of natural cellular solids, which unite high porosity and mechanical stability, is of great interest for potential applications, such as catalysis, sensing or energy storage (e.g. lithium-ion batteries (LIBs)) and conversion.^[21,22] These applications typically require a large specific surface area with good accessibility, but at the same time sufficient resilience.

A material, which can find application in all these fields, is vanadium pentoxide.^[23–33] It is an inorganic compound consisting of 2 vanadium and 5 oxygen atoms per unit cell, yielding the chemical formula V_2O_5 and an orthorhombic crystal structure (space group $Pmmn$), as depicted in figure 3.3.^[34–36] The unit cell with the lattice parameters $a = 11.519 \text{ \AA}$, $b = 3.564 \text{ \AA}$ and $c = 4.373 \text{ \AA}$ ^[34] exhibits stacked V_2O_5 sheets, assembled from VO_5 pyramidal units. Such a layered structure provides enough space to accommodate ions,^[37–39] making V_2O_5 extremely interesting as electrode material for electrochemical energy storage.

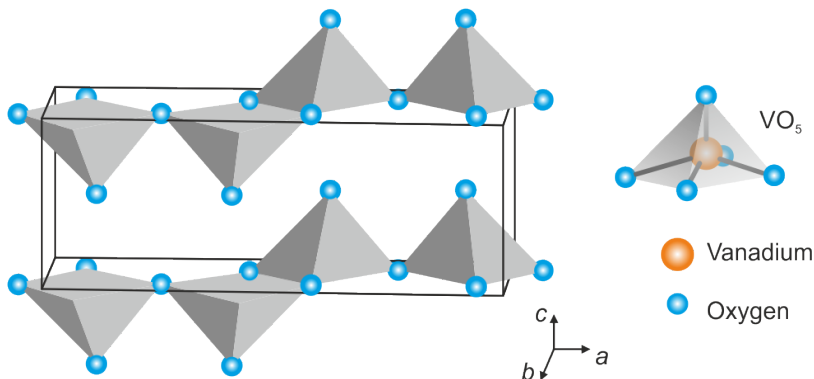


Figure 3.3: Crystal structure of orthorhombic V_2O_5 with the lattice parameters $a = 11.519 \text{ \AA}$, $b = 3.564 \text{ \AA}$ and $c = 4.373 \text{ \AA}$.^[34] The displayed unit cell is adapted from the one of Ma *et al.*^[36]

However, when developing battery electrodes, not only the ability of a material to accommodate ions is important, but also short diffusion paths and good electrical conductivity. Both are crucial to achieve high electrochemical capacities, good cycling stability as well as fast charging rates. Short diffusion paths can be realized by using nanostructured active material.^[40] There are several routes reported to synthesize nanosized V_2O_5 of various shapes and dimensions.^[41–45] In particular, Livage^[41,46] pioneered the synthesis of ribbon-like V_2O_5 nanofibers using a sol-gel method (figure 3.4). In this facile synthesis protocol, the nanofibers were obtained in aqueous solutions from sodium- or ammonium metavanadate precursors. Such vanadate precursors, however, are charged $[H_nVO_4]^{(3-n)}$ and would repel each other, thus inhibit fiber formation. In order to realize charge neutrality, it requires acidification of the solution ($\text{pH} \approx 2$), which can be achieved through a proton ion exchanger. This step is accompanied by a nucleophilic addition of two water molecules to the vana-

date complex, leading to the hexacoordinated species $[\text{VO}(\text{OH})_3(\text{OH}_2)_2]^0$, as depicted in figure 3.4a. Owing to the fact that these species exhibit different bonds along the a - and b -axes, polycondensation reactions occur anisotropically.

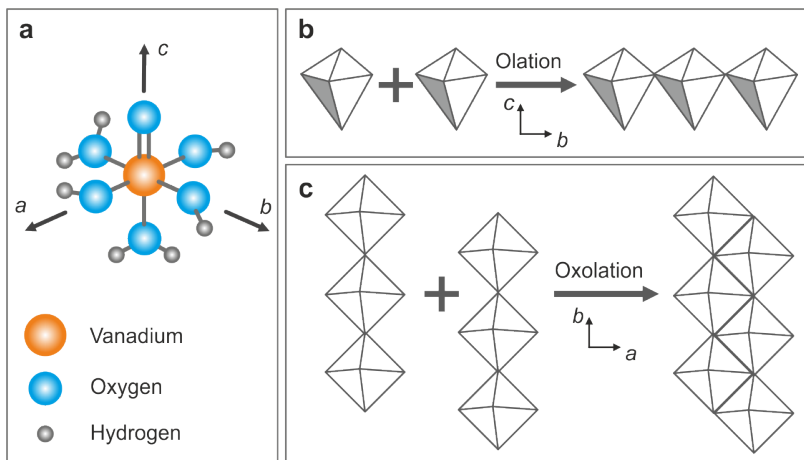
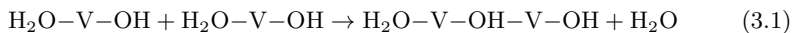
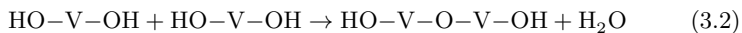


Figure 3.4: (a) Scheme of a 6-fold coordinated V^{5+} with different vanadium-oxygen bonds along the a and b -axes, enabling anisotropic condensation. (b) Fast condensation reactions along the b -axis (olation) lead to corner-shared chains. (c) Slow condensation reactions along the a -axis (oxolation) lead to edge-shared ribbons. The schematics are adapted from the V_2O_5 nanofiber synthesis of Li-vage.^[41,46]

Figure 3.4b schematically displays the faster olation along the b -axis, leading to corner-shared chains *via* the reaction in equation 3.1.



The slower oxolation along the a -axis leads to a broadening of the chains *via* the reaction in equation 3.2, resulting in edge-shared double chains (figure 3.4c).



The combination of these two condensation reactions yields V_2O_5 nanofibers of high aspect ratio.^[41,47] Structural investigations of so-called V_2O_5 xerogels ($\text{V}_2\text{O}_5 \cdot n\text{H}_2\text{O}$, with n = the water fraction per V_2O_5 unit), prepared by simple water evaporation, revealed a crystal structure, which differs from the one of

pristine V_2O_5 . They exhibit a monoclinic unit cell, in which the V_2O_5 sheets (analog to pristine V_2O_5) are separated by a water layer, leading to the lattice parameters $a = 11.722 \text{ \AA}$, $b = 3.570 \text{ \AA}$, $c = 11.520 \text{ \AA}$ and $\beta = 88.65^\circ$.^[35] The pronounced increase in interlayer distance provides even more space for additional ions, thus could lead to an enhanced intercalation capacity.^[48] In addition, the high surface-to-volume ratio of the V_2O_5 nanofibers facilitates the accessibility for the intercalating ions, leading to a high energy density and high rate capability.^[40] Moreover, the uptake of ions is typically accompanied by a volume expansion of the active material, which can lead to mechanical failure due to the induced stresses. Nanostructuring can help minimizing this risk, increasing the cycling stability, thus the lifetime of the electrode material.^[40,49]

The use of the V_2O_5 nanofibers is further advantageous, as the nanofibers exhibit an intrinsic moderate electrical conductivity.^[41,47] This conductivity arises from two complementary mechanisms. First, owing to the synthesis procedure, the V_2O_5 nanofibers contain besides the V^{5+} species a small fraction of V^{4+} . Electrons can hop between these two species, inducing an electrical current. The second mechanism is of ionic nature, driven by proton diffusion through the xerogels' matrix, thus is strongly linked to the xerogels' hydration state.^[41] The intrinsic conductivity of the V_2O_5 nanofibers gives rise to their application also beyond energy storage. For example, Liu *et al.*^[25] reported the V_2O_5 nanofibers' ability to sense ethanol. The exposure to ethanol vapor resulted in a measurable drop in resistance, whereat the magnitude of the drop showed a correlation to the ethanol concentration.

As mentioned above, these applications require a large specific surface area and good accessibility. Both can be achieved by fabricating highly porous materials. However, to date only a limited number of studies report about the fabrication of 3D V_2O_5 and V_2O_5 -based materials.^[50–57] These 3D materials were prepared either *via* freeze drying, supercritical drying or *via* solvent exchange and subsequent drying. The latter leads to so-called ambigels with a random microstructure and a specific surface area of up to $210 \text{ m}^2/\text{g}$.^[51] A likewise random microstructure could be achieved using a freeze drying approach, yielding aerogels with specific surface areas between 42 and $280 \text{ m}^2/\text{g}$.^[51,52,57]

3.3 Fabricating Porous Materials

Freeze drying (also called freeze casting), a well-established technique in the field of powder technology, enables fabricating (ceramic) solids that feature an adjustable, induced porosity.^[58–61] In principle, this technique includes 4 steps: preparation of the slurry, ice-templating, drying and thermal post-treatment, depicted in figure 3.5.

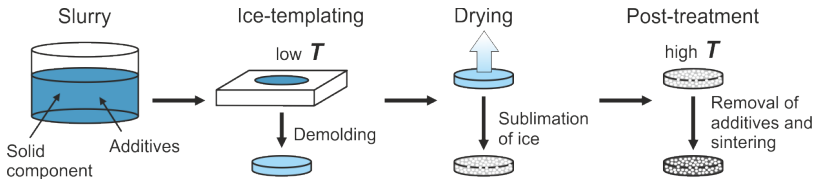


Figure 3.5: Schematic of the freeze drying procedure, divided into 4 steps. The schematic is inspired by the illustration of Li *et al.*^[61]

Conventionally, the slurries are water-based,^[61] but also other solvents, such as camphene,^[62] are possible. They contain a solid component in the form of particles,^[63] platelets^[64,65] or fibers^[66,67] at a defined solid load. The latter renders the porosity of the fabricated cellular solid. Moreover, the slurries typically contain a number of additives, including wetting agents, liquefiers, structuring agents and binders. The choice of additives not only influences the homogeneity and viscosity of the slurry, but also the formation of the microstructure and the stability of the freeze dried green body.^[58,59]

The prepared slurries are then usually poured in a shaping die (mold), in which they are solidified at low temperatures (typically between -10 and -196 °C) (figure 3.5). This step is the crucial one, as it directs the formation of the solids' microstructure. The forming ice crystals (in aqueous slurries) serve as templates for the assembly of the solid components, therefore this step is also called ice-templating. Besides the choice of structuring agents in the slurries, the microstructure is mainly controlled *via* the freezing conditions.^[58,65] Deville^[68] reported the temperature-dependent formation of snowflakes and compared them to pore shapes of cellular solids obtained by ice-templating, visualizing the diversity of fabricable porous structures with this technique. In particular, lamellar porous materials are widely studied.^[63,66,67,69–74] These studies take advantage

of the anisotropic growth kinetics of hexagonal ice, which enables the ice crystals to grow in the shape of plates.^[58] Figure 3.6 schematically depicts such an ice crystal plate with its characteristic features.^[63] The plate has a flat bottom, and a top, which is decorated with an array of dendrites. The dendrite periodicity thereby exhibits a linear relation to the ice crystal thickness^[63] and the latter can be controlled *via* the freezing speed.^[69] In addition, the ice crystal features a row of predominantly round tips along the ice front. The presence of these tips promotes the formation of inter-lamellar bridges.^[66,67]

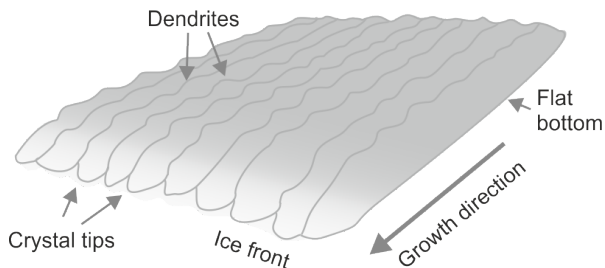


Figure 3.6: Schematic drawing of an ice crystal plate with its characteristic features, as identified by Deville *et al.*^[63]

During the formation of the ice crystals, the solid components become trapped between the plates within the freezing slurries. Subsequently, the frozen slurries are demolded and then dried (figure 3.5). In this step the ice is removed *via* sublimation, meaning the direct transition from the solid to the gaseous phase. The sublimation allows avoiding capillary forces upon water removal, preserving the ice-templated microstructure. Finally, thermal post-treatment is usually necessary to remove the additives and sinter the solid green body, yielding the desired mechanically stable porous materials.^[22,73,75]

3.4 Mechanical Properties of Porous Materials

The mechanical performance of porous scaffolds and foams is mainly a function of the cell wall material (meaning the solid phase, which frames the pores) and microstructure. However, independent from that, the stress-strain curves of all types of cellular solids exhibit a similar shape under compression, as schematically depicted in figure 3.7. Such curves can be divided into 3 regimes:

(i) linear-elastic deformation, (ii) nonlinear deformation and (iii) densification, whereat the extend of each regime is determined by the relative density $\frac{\rho}{\rho_s}$ of the scaffolds/foams.^[76]

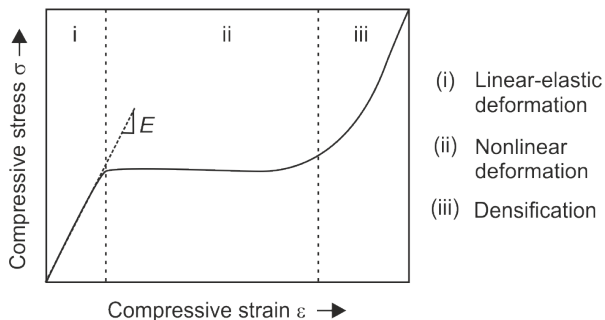


Figure 3.7: Schematic stress-strain curve of a cellular solid under compressive load, exhibiting 3 different regimes: (i) linear-elastic deformation, (ii) nonlinear deformation and (iii) densification. The diagram is adapted from plots reported by Ashby.^[76]

The first regime (i) arises from elastic bending of the cell walls under compressive stress, therefore the slope of this linear part in the stress-strain curve equals the Young's modulus E of the scaffold/foam, according to equation 3.3.^[77]

$$E = \frac{\sigma}{\epsilon} \quad (3.3)$$

where σ is the stress, while ϵ is the strain. Ashby^[76] introduced a mathematical correlation between a scaffold's Young's modulus (respectively the relative Young's modulus $\frac{E}{E_s}$) and its relative density, which is based on an idealized isotropic 3D model of a cubic cell geometry with open cell walls (equation 3.4).

$$\frac{E}{E_s} = C_2 \cdot \left(\frac{\rho}{\rho_s}\right)^2 \quad (3.4)$$

where C_2 is a constant, which equals 1. E and ρ are the Young's modulus and density of the scaffold/foam, respectively. Analog, E_s and ρ_s are the Young's modulus and the density of the scaffold/foam walls, respectively. Plotting $\frac{E}{E_s}$ over $\frac{\rho}{\rho_s}$ of different open-cell polymers,^[78–80] or even ceramic/glass foams^[81] reveals a power function, which appears to be independent from the class of cell wall material.

This material independency does not apply anymore, when exceeding the linear elastic regime. Regime (ii) is characterized by a leveling of the slope (figure 3.7). Dependent on the cell wall material, Ashby^[76] presented different mechanisms responsible for this leveling. Elastomer foams, such as polyurethane (PU), show a nonlinear elastic behavior due to reversible buckling of the cell walls. Foams made from metals or rigid polymers exhibit plastic yielding. Upon compression, such foams create plastic hinges, keeping the compressive stress at a relative constant level. Ceramic scaffolds are assigned to the group of brittle foams that feature brittle crushing. Analog to equation 3.4, the open-cell model allowed to formulate a correlation between a ceramic scaffold's/foam's relative crushing strength $\frac{\sigma_f^*}{\sigma_f}$ and its relative density (equation 3.5).

$$\frac{\sigma_f^*}{\sigma_f} = C_7 \cdot \left(\frac{\rho}{\rho_s}\right)^{3/2} \quad (3.5)$$

where C_7 is a constant with a value of about 0.65. σ_f^* is the foam's crushing strength, ρ and ρ_s are the density of the foam and the cell walls, respectively. σ_f is the modulus of rupture. In case of brittle materials the modulus of rupture is approximately the foam wall material's tensile strength at point of failure. Plotting $\frac{\sigma_f^*}{\sigma_f}$ over the $\frac{\rho}{\rho_s}$ of brittle foams,^[82] likewise resulted in a power law.

Further compression leads to densification of the scaffold/foam in regime (iii), in which the slope of the stress-strain curve (figure 3.7) drastically increases. The mechanical properties of the scaffold/foam approach the ones of the bulk material.

The idealized isotropic 3D model of a cubic cell geometry is widely used, as the mechanical performance of most man-made scaffolds/foams follow its correlations.^[76] However, this model does not simply apply for most anisotropic materials such as freeze dried lamellar scaffolds,^[73] wood or cork.^[76] Bai *et al.*^[73] reported about a dual temperature gradient, which allowed fabricating lamellar scaffolds with a large-scale alignment. The mechanical performance of these scaffolds strongly differ dependent on the orientation of the lamellas to the direction of the applied load. Wood and cork likewise exhibit an anisotropic microstructure, which results in a direction dependent mechanical performance. For such anisotropic materials the mathematical correlations need to be adjusted.^[80,83,84] In contrast, natural cuttlebone behaves differently. Even though

its lamellar microstructure is anisotropic, its macroscopic mechanical properties are mostly direction independent, as obtained by Birchall and Thomas.^[14] This orientation insensitivity is a result of the numerous regularly distributed pillars, which stabilize the lamellar microstructure, making the idealized isotropic 3D model of a cubic cell geometry suitable for this type of biomaterial.

3.5 Mechanical Damping

The compression test in section 3.4 only describe the (quasi-) static mechanical behavior of cellular materials. Damping measurements, on the other hand, address their dynamic mechanical performance. In such measurements the scaffolds/foams are dynamically excited by a harmonic oscillation, leading to dynamic values of compressive stress and strain (figure 3.8). Correspondingly, equation 3.3 needs to be differently defined, resulting in the complex modulus E^* (equation 3.6).^[85]

$$E^* = \frac{\sigma}{\epsilon} = \frac{\sigma_0}{\epsilon_0}(\cos \delta + i \sin \delta) = E' + iE'' \quad (3.6)$$

with σ_0 and ϵ_0 as the stress- and strain amplitude, respectively, as well as the storage modulus E'

$$E' = \frac{\sigma_0}{\epsilon_0} \cos \delta \quad (3.7)$$

the loss modulus E''

$$E'' = \frac{\sigma_0}{\epsilon_0} \sin \delta \quad (3.8)$$

and the phase angle δ . This phase angle originates from a lag between the induced stress and the resulting strain. Considering a harmonic excitation, both curves would be conform in the case of an ideal elastic material, while they would exhibit an offset (δ) in the case of a viscoelastic material (figure 3.8a,b).^[86] The phase lag leads to a hysteresis in the dynamic stress-strain diagram, also called Lissajous figure, in which larger phase angles yield larger areas of the hysteresis loop (figure 3.8d).^[87] These hysteresis loops render a material's loss factor $\tan \delta$, which is a measure for its damping capacity. Dividing the loss modulus by the storage modulus allows calculating $\tan \delta$ (equation 3.9).

$$\tan \delta = \frac{E''}{E'} \quad (3.9)$$

High damping capacities, meaning the elastic strain energy dissipation during mechanical vibration, can be either achieved by intrinsic or external means.^[85] Intrinsic damping, also called material damping, is determined by the choice of material. For example, while polymeric materials, such as PU, exhibit a good mechanical damping behavior, ceramics and metals usually exhibit a poor damping behavior.^[88] The damping capacity can be further enhanced by external means, which can be summarized as structural damping and includes air damping and joint friction, characteristic for porous materials.^[86]

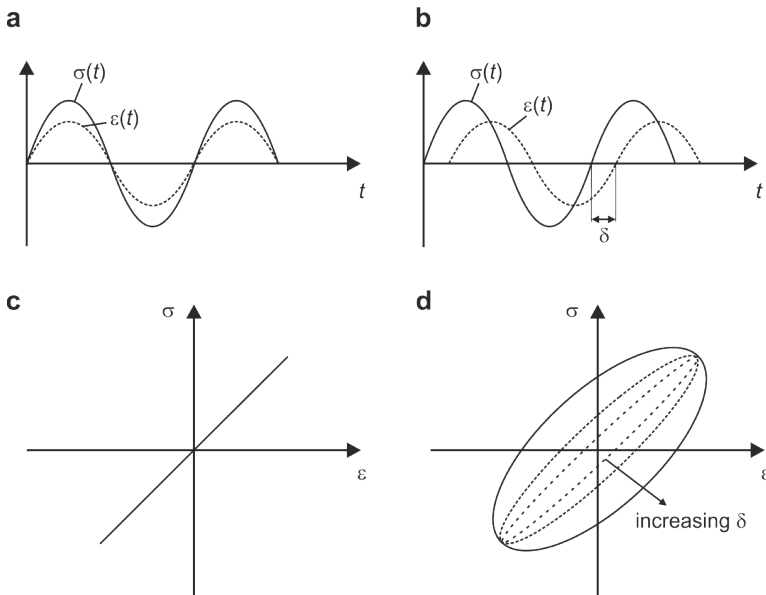


Figure 3.8: Harmonic excitation ($\sigma(t)$) and response ($\epsilon(t)$) of (a) an ideal elastic solid and (b) a viscoelastic solid. The schematics are adapted from the diagrams of Jones.^[86] (c) and (d) Corresponding Lissajous figures, analog to the diagrams of Lakes.^[87]

The viscoelastic response of a scaffold/foam not only depends on the type of material and its microstructure, but also on the test conditions, including applied frequency,^[89,90] temperature,^[90,91] compression state^[92] and strain amplitude.^[89–91,93] These parameters need to be taken into account depending on the respective field of application.

3.6 Fundamental Techniques

3.6.1 Atomic Force Microscopy

Atomic force microscopy (AFM) is a tool developed to investigate surfaces in detail. Its high lateral resolution (0.1 nm) allows visualizing micro- to nanometer sized surface features. Even arrangements of individual atoms can be made visible with this technique. Unlike most other types of microscopes, AFM does not use light or electrons to image a structure. This technique is based on scanning the surface with a sharp probe, which physically "feels" structural unevenness. The probe is attached to a cantilever that can vertically deflect, whereat the extend of deflection depends on the surface below the probe. A laser beam targets the top side of the cantilever, from where it is refracted towards a photo diode. Upon deflection, the motion in the laser beam induces a change in the photo current of the diode. When calibrated, this change in photo current (in mV) can be converted into a distance, leading to a height profile of the surface. By conducting a set of line scans, it is possible to generate color-scaled 2D maps.^[94–96]

AFM can be operated using different modes. In contact mode, the probe is in direct contact with the surface. When scanning an uneven surface, the beam is forced to deflect, as it passes an elevated area. The deflection is then detected with the laser beam. This mode can be used to get information about the topography as well as frictional, magnetic or electrical properties, depending on the used probe and settings.^[97–99] In tapping mode, the cantilever oscillates at its resonance frequency with a defined amplitude. When scanning over an uneven surface, this amplitude is affected, which likewise can be detected with the laser beam. This mode also gives information about the topography, furthermore about mechanical properties.^[100]

3.6.2 Scanning Electron Microscopy

Scanning electron microscopy (SEM) is a well-established technique to visualize 3D structures in the micrometer to nanometer range, using electrons. In this

method, a beam of electrons, which are emitted from a cathode of a so-called electron gun, passes through the evacuated chamber at a defined acceleration voltage and hit the sample. As these primary electrons impinge the surface of the sample, they generate different types of signals (X-rays, Auger electrons, backscattered electrons, secondary electrons), which are emitted by the sample.^[101,102] Most commonly secondary electrons are used for the imaging. Such electrons leave the surface (e.g. the mean escape depth is about 1 nm in case of metals) of the sample with energies below 50 eV and their yield depends on the investigated material as well as on its topography. Detecting these secondary electrons results in high resolution SEM images.^[103]

3.6.3 Brunauer-Emmett-Teller

Brunauer-Emmett-Teller (BET) is an analytical technique, which provides information about the specific surface area and the pore size distribution of materials. It makes use of the adsorption of gases, typically N₂, on the surface of the material.^[104,105] While Langmuir mathematically described the adsorption of only a monomolecular layer,^[106,107] the BET calculation takes in account multimolecular layers, which adsorb *via* physisorption. In general, the BET method is based on several assumptions, including that adsorption and desorption are in a dynamic equilibrium and that the Langmuir isotherm is valid for every single monomolecular layer. In order to characterize a material, the samples are first degassed and then exposed to the adsorbate. The amount of adsorbed molecules is recorded (either volumetrically or gravimetrically) as a function of gas pressure at a constant temperature, leading to adsorption isotherms, which allow calculating the specific surface area.^[108]

3.6.4 Optical Dilatometry

Optical dilatometry enables to monitor the macrostructural development of a material upon thermal treatment. A typical setup consists of a tube furnace, which has the sample placed in its center, a light source and a camera. While the light source is positioned at one end of the tube, the camera is positioned at

the other end. Therefore, the light source illuminates the sample from one side, enabling the camera on the other side to detect the contour of the sample. In this way, the size and shape of a sample can be recorded as a function of temperature.^[109,110] For most materials a shrinkage is being detected upon annealing (respectively sintering^[111]) and assuming the samples shrink isotropically, the volume shrinkage can be calculated from the evolution of shaded area.

3.6.5 Thermogravimetric Analysis

Thermogravimetric analysis (TGA) allows measuring the mass loss upon thermal treatment. In this technique, the sample is placed inside a crucible, which is mounted onto a highly sensitive balance. When increasing the temperature, volatile matter (such as water) is removed from the sample, leading to a reduction in mass, which is recorded by the balance. The mass loss can be plotted over the temperature or time, dependent on the chosen temperature profile. In addition, the thermal treatment can be carried out in different atmospheres, such as inert gas, air or oxygen.^[112] Dependent on the atmosphere, potential chemical reactions can be suppressed or even induced, leading in some case to an increase in mass (e.g. oxidation).^[113]

3.6.6 Differential Scanning Calorimetry

Most TGAs are complemented by a differential scanning calorimetry (DSC) option, allowing measuring phase transformations upon annealing. This technique requires a second, empty crucible, which serves as reference. Both crucibles are simultaneously exposed to the given temperature profile. As soon as the sample starts to undergo an endothermic or exothermic phase transformation, the crucibles do not exhibit the same temperature anymore. Bringing both back to the same temperature requires applying an additional external electrical power. Recording this electrical power as a function of temperature or time yields the typical DSC curve, in which maxima represent endothermic processes, while minima represent exothermic processes.^[112]

3.6.7 X-Ray Powder Diffraction

Analyzing the crystal structure of a material can be achieved by using X-ray powder diffraction (XRPD). In this technique, the sample is exposed to a X-ray beam, which diffracts from the electron clouds around the atoms of the crystalline material.^[114] If X-ray waves diffract, they can interfere with each other and Bragg^[115] formulated an equation for the case of constructive interference of X-rays diffracted from the material (equation 3.10).

$$n\lambda = 2d \sin \theta \quad (3.10)$$

with n as diffraction order (positive integer), λ as the wavelength of the used radiation, d as the interlayer distance and θ as the diffraction angle. By exposing the sample to a X-ray beam with a defined wavelength (monochromatic) under certain diffraction angles, the diffracted waves amplify each other, which results in a distinct peak in the XRPD pattern. These pattern are usually obtained *via* measuring in Bragg-Brentano geometry.^[116] In this geometry, the sample is placed in the center of a goniometer circle and the X-ray source as well as the detector are moved along this goniometer circle. The corresponding angles between sample and source as well as between sample and detector are the same (θ - 2θ method).^[117] The peak position (2θ) of a XRPD pattern allows to calculate the respective interlayer distance, using equation 3.10.

4 Experimental Part

4.1 Scaffold Fabrication

V₂O₅ scaffolds were fabricated following a protocol, which includes the synthesis of the V₂O₅ nanofibers, the freezing of the aqueous nanofiber suspensions (also called ice-templating), the removal of the ice by sublimation (drying) and potentially post-treating the samples thermally.

4.1.1 Synthesis of the V₂O₅ Nanofibers

Colloidal V₂O₅ nanofiber suspensions were prepared by an acid-induced polycondensation reaction derived from the synthesis procedure introduced by Livage.^[41] 1 g NH₄VO₃ and 10 g Dowex 50WX8 50-100 ion exchanger were added to 200, 75 or 50 ml deionized H₂O. The mixtures were stirred in an oil bath at 80 °C for 10 min to initiate the fiber formation. This initiation is accompanied by a discoloration of the aqueous solution towards dark red. Subsequent aging at room temperature for 2 weeks led to fiber lengths of up to several micrometers. After the aging time of 2 weeks, the nanofiber suspensions were separated from the ion exchanger by decantation. The resulting V₂O₅ nanofiber concentration of the three different suspensions (C1, C2 and C3', respectively) was evaluated gravimetrically (table 4.1). Furthermore, C3' was diluted with deionized water to become the final concentration C3. This final concentration C3 represents the maximum concentration for preparing V₂O₅ scaffolds, which can be mechanically investigated with the used NanoBionix system (figure 4.5).

Table 4.1: V_2O_5 nanofiber concentration of the synthesized colloidal suspensions.

Suspension	deionized H_2O (ml)	V_2O_5 nanofiber concentration (mg/ml)
C1	200	3.55 ± 0.04
C2	75	7.64 ± 0.04
C3'	50	19.36 ± 1.36
C3	diluted C3'	14.51 ± 1.36

4.1.2 Fabrication of the Molds

In order to obtain V_2O_5 scaffolds with a defined geometry, suitable molds are required. Such molds were prepared from silicone rubber (Wacker Silicones Elastosil RT 675 A/B). The silicone rubber was cast around a metal rod, which had a length and diameter of 8 mm, and then cured at room temperature for one day. Removing the metal rod resulted in a flexible negative of the desired sample geometry. The molds were placed in Petri dishes, which sealed the bottom of the molds, and then stored in a climatic chamber (Vötsch VC 7018) at $-25^\circ C$, making them ready to be filled.

4.1.3 Ice-Templating

In general, ice-templating involves the freezing of the aqueous V_2O_5 nanofiber suspensions, in which the forming ice crystals served as template for the V_2O_5 nanofibers. By varying the freezing condition, thus the ice crystal formation, different microstructures could be achieved. The first batch of samples were prepared by filling the molds with V_2O_5 nanofiber suspension and then slowly freezing them in the climatic chamber at $-25^\circ C$. After 1 hour freezing time, the frozen samples were demolded with the help of a metal rod, which pushed the frozen scaffolds out of the molds. The free-standing frozen samples were subsequently dried, as described in section 4.1.4. This freezing condition was only used for freezing the C1 suspension and the resulting samples served as randomly structured reference scaffolds V_2O_5-0 (table 4.3).

The following batches of samples were produced by filling the silicone molds with V_2O_5 nanofiber suspensions and then completely dipping them in liquid N_2 to shock-freeze the suspensions at -196°C (figure 4.1). Subsequent storage of the frozen samples in the climatic chamber at -25°C for 15 min softened the cold molds without melting the frozen samples, thus facilitated the demolding process. The free-standing frozen samples were then dried analog to the first batch. This freezing condition was used to fabricate scaffolds of the concentrations C1, C2 and C3 (table 4.1), leading to the scaffolds V_2O_5 -1, V_2O_5 -2 and V_2O_5 -3, respectively (table 4.3).

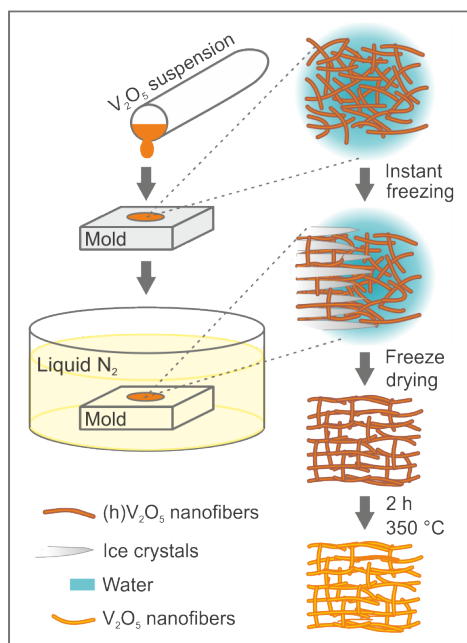


Figure 4.1: Schematic depiction of the scaffold fabrication: Aqueous V_2O_5 nanofiber suspension was poured into the cylindrical cavity (length and diameter of 8 mm) of the mold, which was then immersed in liquid N_2 to instantly freeze the aqueous suspension (ice-templating step). Subsequent drying led to a self-supporting, hydrated V_2O_5 scaffold ($V_2O_5 \cdot nH_2O$) with the ice-templated microstructure and the same dimension as the cylindrical cavity of the mold. Potential annealing at 350°C yielded a phase pure V_2O_5 scaffold with preserved microstructure. This figure is adapted and reprinted with permission from Knöllner *et al.*,^[118] Copyright 2018, American Chemical Society.

4.1.4 Drying

The frozen samples were placed in a pre-cooled (-50°C) freeze dryer (P4K Peter Piatkowski) to avoid melting. The drying itself was achieved using the program listed in table 4.2, which involves slowly raising the temperature at a chamber pressure of $30\ \mu\text{bar}$. This gentle way to remove the ice *via* sublimation resulted in the as-prepared (hydrated) cylindrical V_2O_5 scaffolds with a length and diameter of 8 mm.

Table 4.2: Applied freeze drying program to obtain V_2O_5 scaffolds.

Precess step	Time (h)	Temperature ($^{\circ}\text{C}$)	Vacuum (μbar)
Freezing	1	-50	0
Vacuum	2	-50	30
Sublimating	5	-40	30
	5	-25	30
	3	-10	30
	3	10	30
	3	23	30

4.1.5 Post-Treatment

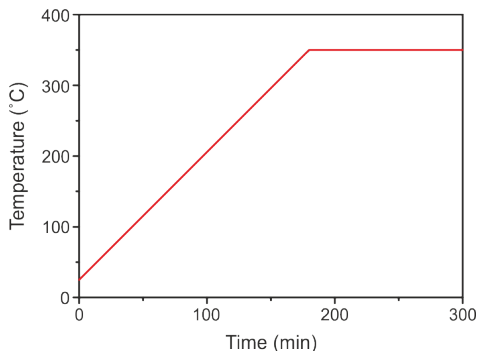


Figure 4.2: Temperature profile of the post-treatment step.

Complementary to the as-prepared hydrated V_2O_5 scaffolds, one batch of V_2O_5 -1 scaffolds was in addition thermally post-treated, as depicted in figure 4.1. The samples were heated in air with a heating rate of 3 K/min to 350 °C, where they were kept for two hours (figure 4.2), and then slowly cooled to room temperature, yielding the phase pure scaffolds V_2O_5 -1A (table 4.3).

Table 4.3: Overview of all types of fabricated samples.

Sample name	Concentration	Freezing temperature (°C)	Post-treatment
V_2O_5 -0	C1	-25	-
V_2O_5 -1	C1	-196	-
V_2O_5 -2	C2	-196	-
V_2O_5 -3	C3	-196	-
V_2O_5 -1A	C1	-196	2h at 350 °C

All samples were gravimetrically investigated with a Mettler Toledo UMX2 microbalance. Their weights in combination with their dimensions allowed calculating the samples' density.

4.1.6 Natural Cuttlebone and Polyurethane Foams

Natural cuttlebone and PU foams served as reference for the mechanical stability and for the damping properties of the V_2O_5 scaffolds, respectively. Complete cuttlebones of *sepia officinalis* were commercially purchased from the local pet shop. All cuttlebones were dry and intact. The used PU foams were standard cushioning mats, a typical packaging material.

4.2 Scaffold Characterization

4.2.1 Structural and Compositional Investigation

Atomic Force Microscopy

The nanofibers' dimensions were investigated topographically, using a Bruker Multimode 8 AFM with Nanoscope V controller and Nanoscope software in tapping mode. Samples of single V_2O_5 nanofibers were prepared by depositing droplets of highly diluted V_2O_5 nanofiber suspensions on boron-doped silicon (100)-wafer (*p*-type, Wacker, Siltronic AG). The wafer were cleaned in advance by ultrasonication in chloroform, acetone and ethanol for 10 min each. Between each step, the wafer were dried in a N_2 flow. The used wafers had dimensions of 10 by 10 mm, suitable for AFM investigations. Slow water evaporation let to randomly oriented single nanofibers attached to the wafer's surface. While the length of the nanofibers was directly accessible through the recorded AFM images, height profiling gave information about the nanofibers' thickness.

Scanning Electron Microscopy

In order to investigate the microstructures of the V_2O_5 scaffolds with an SEM, frozen samples were fractured prior to their drying, making different viewing directions accessible. After drying, the fragments were glued on standard SEM sample holders using electrically conductive carbon tape. For better imaging, the fragments were subsequently sputtered (Leica EM ACE600) with 1.5 nm iridium, which made their surface electrically conductive.

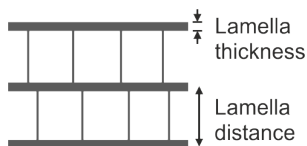


Figure 4.3: Structural features of cuttlebone and cuttlebone-like microstructures.

The imaging itself was carried out with a Zeiss Merlin SEM at 1 kV and a working distance of about 3 mm, using an inlens detector. The images also provided information about the size of the structural features, such as lamella thickness and lamella distance (figure 4.3), measured with a Digital Image Processing System 2.9 software.

Besides standard imaging, samples' mechanical deformation could be investigated *in situ* by SEM. For this technique, two standard micromanipulators (Kleindiek Nanotechnik) were installed inside the SEM chamber (figure 4.4, left image). Both micromanipulators (figure 4.4, yellow circle) could be independently moved, using two attached PlayStation2 controllers. Their fine, needle-like tips (figure 4.4, green circle), made from tungsten, enabled precisely deforming the scaffolds. The SmartSEM software was equipped with a video tool, which allowed recording the *in situ* deformation. However, owing to the fact that the used micromanipulators did not have a load cell add-on, simultaneous load recording was not possible.

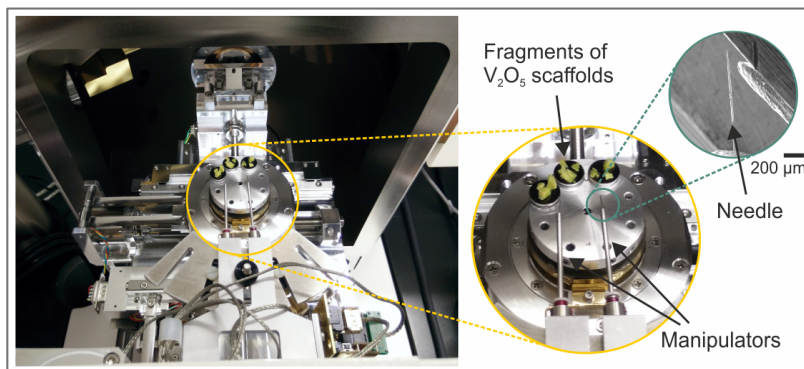


Figure 4.4: Inside view of a SEM chamber (left image). The two manipulators are mounted onto the door of the chamber and are coupled to the SEM sample stage (yellow circle). They are further equipped with fine tungsten needles (green circle), making them capable to precisely manipulate.

Brunauer-Emmett-Teller Analysis

The specific surface area of the V₂O₅ scaffolds was determined through the adsorption of N₂, using a Quantachrome Autosorb Automated Gas Sorption

System. The scaffolds were degassed at 30 °C for 1 hour. The actual analysis time, during which the N₂ was adsorbed, accounted 4 hours.

Optical Dilatometry

For optical dilatometry investigation, the scaffolds were placed in the center of a tube furnace (Gero) and heated in air with a constant heating rate of 3 K/min to 600 °C. The evolution of the scaffolds' shape was recorded with a Sony Hyper HAD B&W video camera, which took an image of the scaffolds' profile every 10 seconds, and the used software (EMI-Erhitzungsmikroskop-Messung&Auswertung) allowed to extract the scaffolds' dimensions from the recorded images.

Thermogravimetric Analysis/Differential Scanning Calorimetry

Simultaneous TGA/DSC measurements were carried out with a Netsch STA 449C under oxygen atmosphere. The scaffolds were pressed into an Al₂O₃ crucible (covered with a lid to avoid possible mass loss due to the applied oxygen flow) and then heated with a heating rate of 2 K/min to 400 °C. This final temperature was kept for 2 hours. In addition, an empty crucible was measured with the same temperature profile and atmosphere, serving as reference.

X-Ray Powder Diffraction

In order to investigate the V₂O₅ scaffolds with XRPD, the scaffolds were compressed with a glass plate, resulting in flat disks. Data collection was carried out with a Bruker D-8 Advance diffractometer (Cu K α ₁ radiation ($\lambda = 1.54056 \text{ \AA}$) from Ge(111) Johansson type monochromator and V $\dot{\text{A}}$ NTEC position sensitive detector) in Bragg-Brentano geometry. XRPD measurements on frozen V₂O₅ suspensions were carried out on an analog system, which was in addition equipped with a closed cycle helium cryostat (Phenix, Oxford Cryosystems). For such measurements, the frozen suspensions were loaded in a pre-cooled (to

avoid melting) copper sample holder. The cooling chamber was then evacuated and set to a temperature of 100 K, at which the data collection was carried out.

4.2.2 Mechanical Investigation

Mechanical Testing of Cuttlebone

Uniaxial compression test were conducted on cubic cuttlebone samples (width, length and height of 6 mm), which were cut out with a razor blade from the center of the bone. Both, lamella orientation perpendicular as well as parallel to the direction of compression, were considered. Owing to the excellent mechanical stability of this biomaterial, the measurements were conducted with a BOSE ElectroForce 3200 Series III (equipment of Prof. Spatz at the MPI-IS), capable to bear 220 N and operating with a WinTest7 control system. The cuttlebone samples were compressed up to 50 % with strain rates of $8 \cdot 10^{-3}$ and $4 \cdot 10^{-3}$ mm/s. The latter (slower) rate was chosen to minimize the setbacks in the stress-strain curves, which arise from the implosion of lamellas upon compression.

Mechanical Testing of V_2O_5 scaffolds and PU foams

Mechanical characterization of the V_2O_5 scaffolds and PU foams were conducted with a Keysight UTM150 NanoBionix, operating with a NanoSuite software. While measurements were performed on cylindrical V_2O_5 scaffolds (section 4.1), the PU foams had a cubic shape with a width, length and height of 10 mm. All samples were uniaxially compressed up to 50 % with a strain rate of $8 \cdot 10^{-3}$ mm/s. The used equipment had a maximum load L of 0.5 N and a load resolution of 50 nN, suitable to investigate ultra light and highly porous materials. The maximum load of 0.5 N renders the maximum density of the V_2O_5 scaffolds at the given sample dimension (cross-section area A), which can be investigated with this machine, according to equation 4.1.

$$L = \sigma \cdot A \quad (4.1)$$

As the compressive stress σ is a function of the scaffolds' density, the V_2O_5 -3 scaffolds represent the upper limit, as displayed in figure 4.5. Complementary, cyclic compression tests were conducted using the same strain rate. After a pre-compression of about 5 %, the samples were cycled in a range of 3 % for 100 cycles.

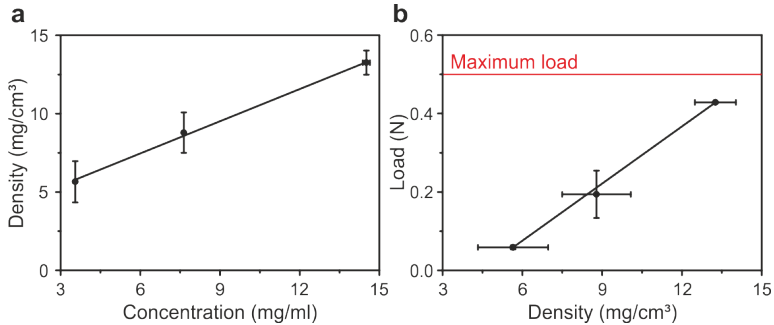


Figure 4.5: Correlation of (a) scaffold density and V_2O_5 nanofiber concentration as well as (b) load on specimen and scaffold density. The red line represents the maximum load the NanoBionix system is capable of.

The NanoBionix system was in addition equipped with a CDA control unit, which allowed performing damping experiments on the V_2O_5 scaffolds and PU foams. Using a modified test method, it was possible to investigate the viscoelastic properties of each sample as a function of compressive strain and frequency. Figure 4.6a visualizes the principle of this type of measurement. In this method, the samples were compressed to 5 % with a strain rate of $8 \cdot 10^{-3}$ mm/s. After 1 minute holding at this first compressive strain, a harmonic oscillation force of 4.5 mN was applied at 6 different frequencies (5, 10, 20, 30, 40 and 45 Hz, 10 seconds each). Subsequently, the samples were further compressed to 10, 20, 30 and 50 %. At each of these compressive strains the same frequency sweep was applied, leading to a compression- and frequency dependent map with 30 points of measurements (figure 4.6b). The storage modulus E' and the loss modulus E'' were automatically calculated with the NanoSuite software, using equations 4.2 and 4.3.

$$E' = \frac{l}{A} \left(\frac{F_0}{z_0} \cos \delta \right) \quad (4.2)$$

$$E'' = \frac{l}{A} \left(\frac{F_0}{z_0} \sin \delta \right) \quad (4.3)$$

with l and A as the instantaneous height and cross-section area of the scaffold,

respectively. F_0 embodies the amplitude of the force oscillation and z_0 the one of the resulting displacement oscillation. The latter lags behind by the phase angle δ . For better visualization, the areas between the measuring points were interpolated, resulting in color-scaled 2D maps.

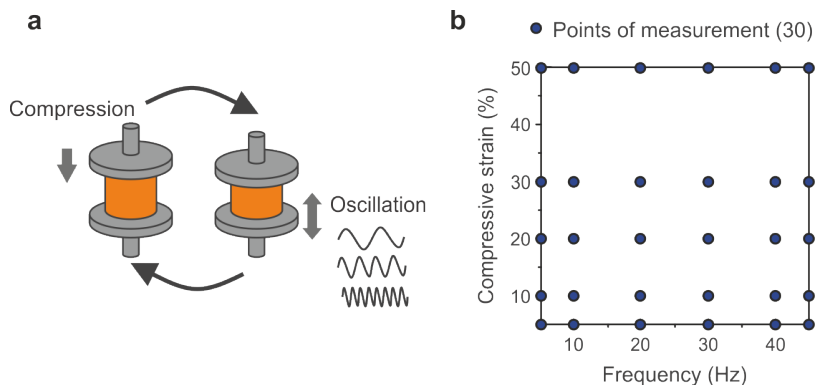


Figure 4.6: Generation of the damping maps: (a) Stepwise compression, which includes a frequency sweep at each compressive strain. (b) Position of the conducted points of measurements (30 in total). This figure is adapted and reprinted with permission from Knöller *et al.*,^[118] Copyright 2018, American Chemical Society.

4.2.3 Contributions

Bernhard Fenk, the technician at the MPI-FKF Nanostructuring Lab of Prof. Jürgen Weis, installed the micromanipulators in the SEM and assisted the handling. M.Sc. Achim M. Diem, a PhD student at the Institute for Materials Science, helped controlling the micromanipulators. Annette Fuchs, the technician from the MPI-FKF department of Prof. Joachim Maier, conducted the BET measurements. TGA/DSC measurements were carried out by Dr. Marc Widenmeyer, who is a postdoc at the Institute for Materials Science. XRPD measurements were conducted by Frank Adams, the technician of Prof. Robert E. Dinnebier at the MPI-FKF Scientific Service Group Diffraction and results were evaluated by Dr. Tomče Runčevski from the Department of Chemistry of the University of California, Berkeley. Dr. Holger Pfaff from Keysight Technologies provided the damping test method and M.Sc. Stefan Kilper, a PhD student at the Institute for Materials Science, helped editing it.

5 Results and Discussion

5.1 Natural Cuttlebone

Natural cuttlebone is an ideal role model for the development of light weight and stable functional materials, such as V_2O_5 scaffolds, due to its unique combination of ultrahigh porosity and mechanical stability. However, to date there is only little research done on the mechanical performance of natural cuttlebone.^[14,15,17] In order to better evaluate the mechanical properties of the novel cuttlebone-like V_2O_5 scaffolds, purchased natural cuttlebone (*sepia officinalis*, figure 3.2a) was mechanically investigated. As the cuttlebone's lamellar microstructure is highly anisotropic, mechanical characterization was conducted on rectangular samples in dependence of its orientation. The two limit cases, namely applying the load perpendicular (figure 5.1a) *vs.* parallel (figure 5.1d) to the lamellas, were considered. In the first case the samples mainly fractured during the measurements, while the second case showed a comparably smooth compaction. Investigating the samples after compression with SEM revealed that in both cases the cuttlebone failed stepwise, meaning only local destruction occurred from one side of the sample, while the majority of the cuttlebone stayed intact (figures 5.1b,e). However, owing to the anisotropic microstructure, the local destruction showed some differences. Figure 5.1c displays the top of a sample, which exhibits fragments of pillars, still attached to the lamella below. The top lamella completely imploded, as mechanical load was applied perpendicular to it, leaving only these few fragments behind. In contrast, figure 5.1f displays a pile-up of loose fragments lying on top of the sample due to a more progressive crushing of the lamellas and pillars. These findings are also reflected in the samples corresponding stress-strain curves (figure 5.2). Initially, both curves show a similar linear trend with predominantly elastic deformation. At higher compressive strains (20 to 50%) the curves reach a plateau with a

frayed progression, which is assigned to brittle crushing^[76] of the dry, ceramic-based cuttlebone. Moreover, at these compressive strains, the influence of the lamella orientation on the local destruction becomes more pronounced. While the stress of the sample compressed parallel to the lamellas stays constant, the plateau of the sample compressed perpendicular to the lamellas is decorated with setbacks, which arise from abrupt destruction of single lamellas. During this pulverization of the whole lamella, the testing machine shortly lost contact to the sample, which temporarily reduced the measured stress. However, for both orientations, the values for strength and Young's modulus of the tested samples are in a similar range, implying that the pillars are as stable as the lamellas. The measurements thus resulted in average values of 1.17 ± 0.13 MPa and 22.86 ± 4.60 MPa, respectively (table 5.2).

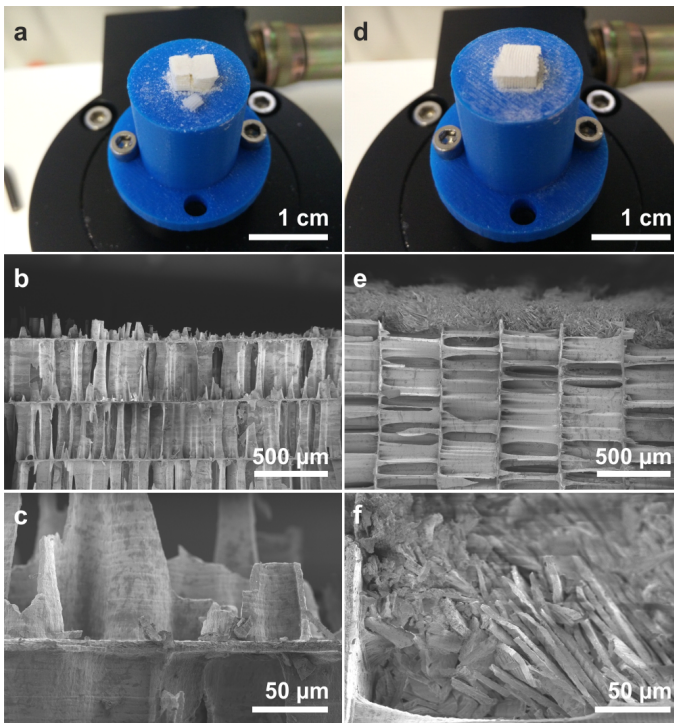


Figure 5.1: Mechanical compression of natural cuttlebone (a) perpendicular and (d) parallel to the lamella orientation. (b,c) and (e,f) Corresponding SEM images after mechanical investigation.

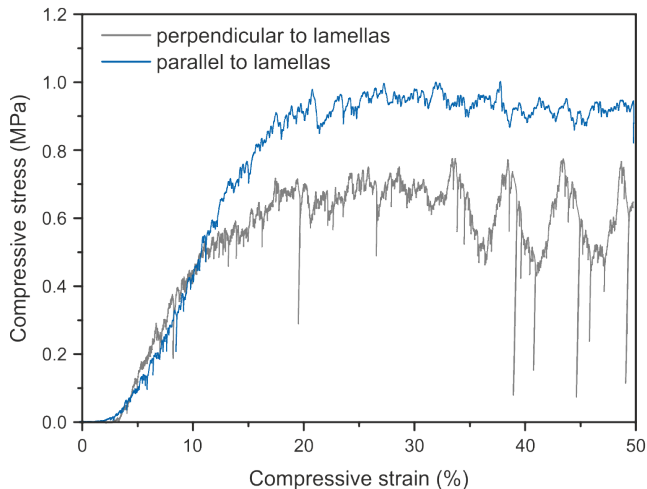


Figure 5.2: Stress-strain curves of natural cuttlebone in dependence of the lamella orientation.

Birchall and Thomas^[14] reported a similar mechanical performance of this type of sepia and the same compressive strength (1.1 ± 0.4 MPa). They also claimed that there is no significant difference in strength between both limit cases. In fact, this predominantly orientation independent mechanical stability is essential for the survival of the sepia, as they are constantly exposed to the hydrostatic pressure coming from the surrounding water. This hydrostatic pressure renders the maximum depth, at which the sepia can survive. Sherrard^[15] investigated different species and correlated their capture depth to their cuttlebone's microstructure. Structural investigation by confocal microscopy revealed that species living in greater depths exhibited thicker lamellas, smaller lamella distances as well as smaller distances between neighboring pillars, which increase the stability^[17] against implosion, but most likely also the density of the cuttlebone. In contrast, the cuttlebone used in this work (*sepia officinalis*) is domiciled in more shallow water with an estimated maximum depth of 189 m.^[15] It exhibits a comparably wider microstructure (table 5.1), setting the compressive strength to the measured 1.17 ± 0.13 MPa, coupled with a remarkably high porosity of 92.7%. The combination of these two contrary properties therefore renders natural cuttlebone to be a perfect role model for the fabrication of functional cellular solids with enhanced mechanical stability.

5.2 Cuttlebone-like V_2O_5 Scaffolds

Mimicking the sophisticated microstructure of natural cuttlebone to design functional materials with a comparable structure-mechanics relation requires an adequate alternative for the ceramic building blocks as well as a suitable structuring protocol. Based on the work of Livage^[41] and Burghard *et al.*,^[47] V_2O_5 nanofibers appear to be appropriate substitutes for the aragonite fibers. Processing these nanofibers by using a freeze drying approach opens the possibility to generate the desired microstructure.

5.2.1 V_2O_5 Nanofiber Building Blocks

The V_2O_5 nanofibers used in this work were fabricated with a sol-gel method analog the one of Livage.^[41] This acid-induced polycondensation of a vanadate precursor in aqueous suspension led to ribbon-like nanofibers with a width in nanometer range and a length of up to several micrometers. The length of the nanofibers can be controlled either *via* the aging time of the resulting suspension or *via* the temperature, whereat the latter shows a stronger influence.^[119] The fiber dimensions were determined by AFM measurements on single nanofibers, which were deposited on a silicon wafer, as displayed in figure 5.3a. The nanofibers appear to be mechanically flexible,^[120] which is reflected in the curved appearance of the displayed V_2O_5 nanofiber. Such mechanical behavior is in principle atypical for ceramics, as they are known to be stiff and brittle. However, these conventional characteristics only apply for bulk ceramics. Scaling down to diameters in nanometer range, coupled with a high aspect ratio, unlocks alternative mechanical characteristics similar to what was found in nature,^[7] making ceramic materials not only mechanical flexible, but also insensitive to flaws.^[121]

AFM height profiling of a nanofiber's cross-section revealed a thickness of about 1.5 nm, corresponding to two corrugated sheets assembled from VO_5 pyramidal units, which further host water molecules in between (figure 5.3b).^[35,41] Thus, these nanofibers do not exhibit the orthorhombic crystal structure of phase pure V_2O_5 , they exist in the form of hydrated V_2O_5 ($V_2O_5 \cdot nH_2O$). The latter

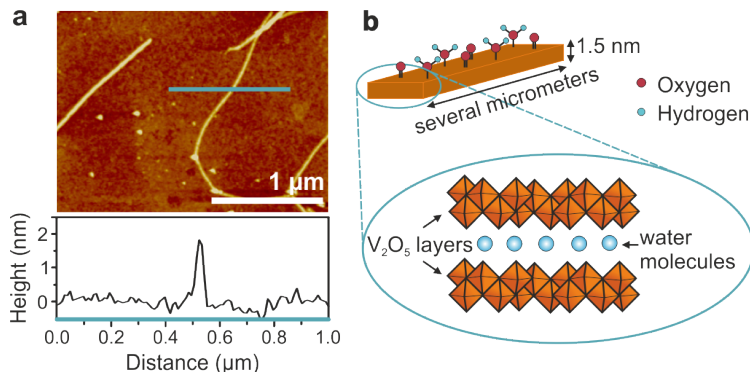


Figure 5.3: (a) AFM image of V_2O_5 nanofibers deposited on a silicon wafer. The height profile reveals a nanofiber thickness of 1.5 nm. (b) Scheme of a V_2O_5 nanofiber, showing the oxygen-functionality at the surface, its double-layered nature and intercalated water molecules. The structure is adapted from the crystal structure found by Petkov *et al.*^[35] This figure is adapted and reprinted with permission from Knöller *et al.*,^[20] Copyright 2017, Springer Nature.

likewise differ in density from the phase pure V_2O_5 (3.36 g/cm^3). The crystal structure solved by Petkov *et al.*^[35] led to a density of 2.78 g/cm^3 , which is in good agreement with the density measured by Liu *et al.* ($\sim 2.5 \text{ g/cm}^3$).^[122] Furthermore, the amount of intercalated water affects the distance of the two corrugated sheets, correspondingly the nanofiber thickness. Livage^[41] investigated the interlayer distance of so-called $V_2O_5 \cdot nH_2O$ xerogels as a function of their hydration state, revealing an increase in the interlayer distance with uptake of water. The exact amount of water within the assembled V_2O_5 scaffolds as well as its removal upon thermal treatment will be discussed in section 5.3.

Another characteristic feature is that the V_2O_5 nanofibers are decorated with oxygen-functionalities on their surfaces (figure 5.3b), which promote the formation of hydrogen bonds (H-bonds). The nanofibers thus can interact with the surrounding water molecules, stabilizing the aqueous suspensions, in which they were synthesized. This stabilization against agglomeration preserves the physical properties of these suspensions for several years.^[123] Moreover, when being assembled, they likewise interact with each other, forming a self-supporting H-bond network.^[47] The combination of their small dimensions, high aspect ratio, mechanical flexibility and surface functionality qualifies the V_2O_5 nanofibers to be a close-to-ideal candidate for the fabrication of complex and sophisticated

microstructures. Therefore, the nanofibers appear to be a suitable substitute for the aragonite building blocks towards the fabrication of artificial cuttlebone.

5.2.2 Ice-Templating of V_2O_5 Nanofibers

Besides the proper choice of building blocks, also the structuring procedure plays a major role for the fabrication of cuttlebone-like cellular solids. Numerous groups already reported the possibility to generate lamellar ceramic microstructures using ice-templating.^[58,70–74] Such ceramic-based scaffolds were typically fabricated by freezing aqueous slurries, which contained ceramic particles and numerous additives. Since the V_2O_5 nanofibers already exist in the form of a stable aqueous suspensions, no additives, such as dispersants are necessary, allowing a direct interaction between the V_2O_5 nanofibers and the forming ice template.

In general, the ice-templating of V_2O_5 nanofibers includes three different zones along the temperature gradient, as depicted in figure 5.4.^[124] The liquid zone embodies the aqueous V_2O_5 nanofiber suspension, in which the nanofibers are randomly oriented. When freezing the suspension, ice crystals form in the so-called freezing zone, leading to a local increase in the nanofiber concentration between the crystals. Owing to the presence of oxygen-containing functional groups at their surface, the nanofibers assemble to bundles,^[47] which further partake in H-bonds with the ice crystal surface. Finally, in the frozen zone, the temperature gradient decreases, leading to an expansion of the ice crystals in the directions perpendicular to the gradient. During this ice crystal expansion the ice template-directed nanofiber assemblies get trapped between the ice crystals, shaping the V_2O_5 nanofiber scaffold. In the ice-templating process, the size of the ice crystals is strongly triggered by the freezing temperature. The ice-templated microstructure is a result of the competitive balance between ice crystal nucleation and ice crystal growth. Xie *et al.*^[65] investigated the temperature dependent structuring of graphene sponges, fabricated by freeze-drying. They report that the ice crystal growth dominates at higher freezing temperatures ($-40\text{ }^\circ\text{C}$), while the ice crystal nucleation dominates at lower freezing temperatures ($-170\text{ }^\circ\text{C}$).

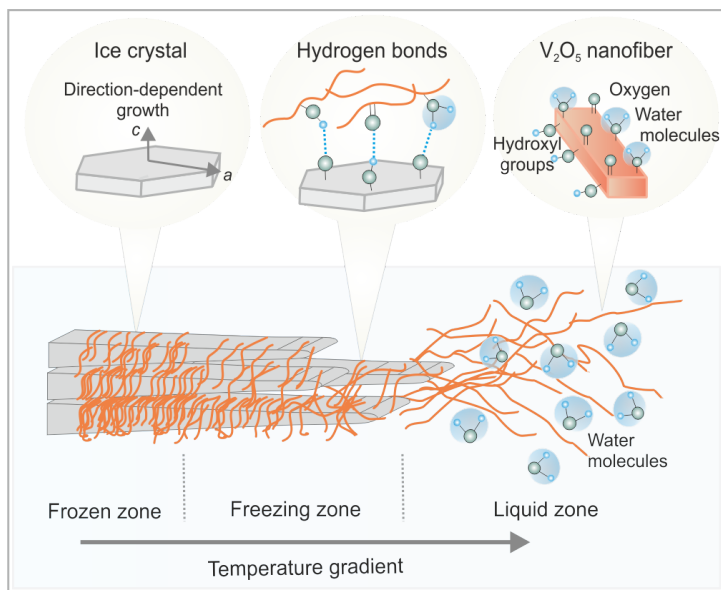


Figure 5.4: Three zones of ice-templating along the temperature gradient.^[124] In the liquid zone V_2O_5 nanofibers are randomly oriented in aqueous suspension, stabilized *via* oxygen-containing functional groups at the nanofibers' surface. Assembling of the nanofibers and attaching of the assemblies to the ice crystals' surface occur in the freezing zone. As the ice crystal front proceeds, the temperature gradient decreases in the frozen zone, allowing the crystals to also grow in the direction perpendicular to the gradient, thus trapping and compacting the nanofiber assemblies. This figure is adapted and reprinted with permission from Knöller *et al.*,^[20] Copyright 2017, Springer Nature.

Therefore, an increased ice crystal nucleation leads to numerous small crystals, which barely grow, resulting in a lot of small pores. High freezing temperatures, on the other hand, lead to fewer nuclei, which grow much bigger. Such trend can also be observed for the present V_2O_5 scaffolds. Analog, slow solidification of the V_2O_5 nanofiber suspension at $-25\text{ }^\circ\text{C}$ led to scaffolds with randomly oriented, several tens of micrometer large and irregularly shaped pores (figure 5.5a), which further exhibited strongly inhomogeneous scaffold walls (figure 5.5b). At this temperature ice crystal nucleation appeared to occur homogeneously throughout the complete volume of the sample. As these nuclei grew mainly undirected, the V_2O_5 nanofibers got trapped in between, forming such a random scaffold structure (V_2O_5 -0).

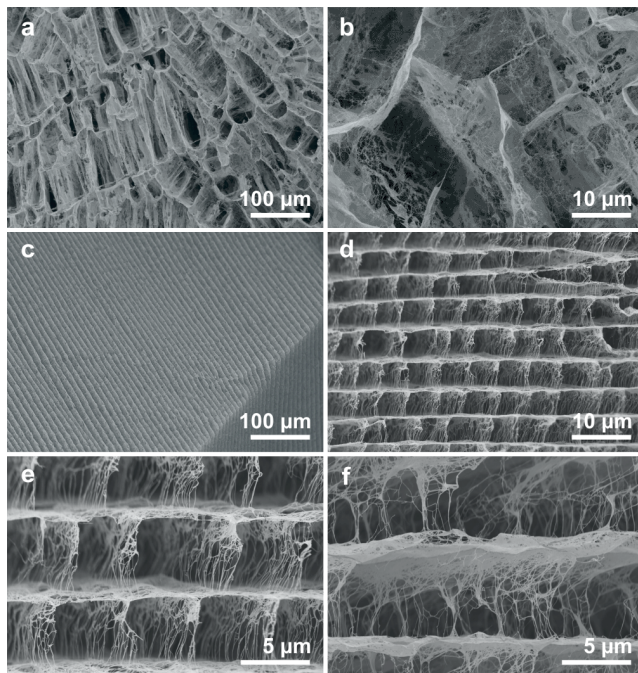


Figure 5.5: SEM images of (a,b) a V_2O_5 nanofiber scaffold slowly frozen at -25°C , showing a random pore size and geometry (V_2O_5 -0), (c-f) a V_2O_5 nanofiber scaffold instantly frozen with liquid N_2 , showing a sophisticated lamellar microstructure (V_2O_5 -1). (e) displays the structure in freezing direction, while (f) displays the structure perpendicular to the freezing direction. (e) is adapted and reprinted with permission from Knöller *et al.*,^[20] Copyright 2017, Springer Nature.

However, when using liquid N_2 , meaning instant freezing the V_2O_5 nanofiber suspension at -196°C , the scaffold exhibit an extremely sophisticated microstructure (figures 5.5c-f). The scaffolds appear to have a regular lamellar structure with interconnecting pillars (V_2O_5 -1). Immersing the V_2O_5 nanofiber suspension in liquid N_2 initiates ice crystal nucleation at the wall of the cylindrical mold. The liquid N_2 -induced temperature gradient from the mold's wall (-196°C) to the center of the suspension (room temperature) causes the ice crystals to grow towards the mold's center (figure 5.6), similar to a previously reported porous Y_2SiO_5 ceramic.^[74] The lamellas of the resulting scaffolds are likewise oriented in a centrosymmetric manner. However, these scaffolds were prepared from slurries containing a high load of Y_2SiO_5 particles and several

additives, including dispersant and binder. Such a slurry composition is typical for conventional freeze drying protocols to fabricate mechanically stable green bodies. [58,70,71,73] Subsequent sintering removes the additives and stabilizes the resulting scaffold. In the case of the Y_2SiO_5 scaffolds this procedure led to irregularly shaped, lamellar pores with lamella distances of about 20 to 50 μm . The lamellas themselves exhibited a thickness of up to several micrometers, a granular structure and had only a few randomly distributed ceramic bridges between them. [74] This microstructure does not represent a detailed negative of the ice crystal plates, [63] which channeled through the slurry upon freezing at -196°C . In contrast, the V_2O_5 scaffolds, in which the nanofiber assembly is strongly guided by the ice crystal formation, display all structural features of the ice crystal plates.

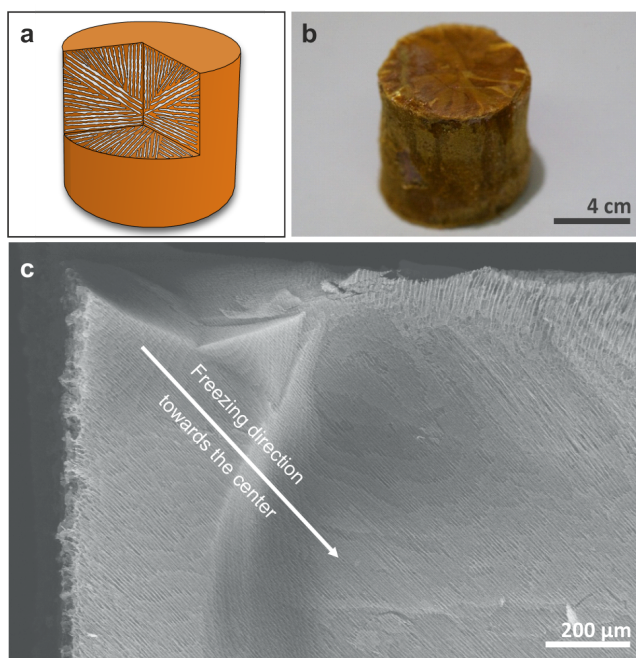


Figure 5.6: (a) Scheme of the centrosymmetric ice crystal plate orientation, (b) optical image of a V_2O_5 -1 nanofibers scaffold, (c) SEM image of the scaffold's cross-section, verifying the ice-templated centrosymmetric lamella orientation. This figure is adapted and reprinted with permission from Knöller *et al.*, [20] Copyright 2017, Springer Nature.

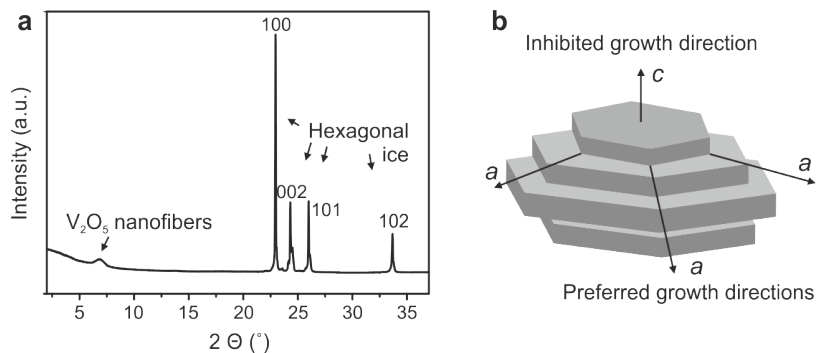


Figure 5.7: (a) XRPD pattern of a V_2O_5 nanofiber suspension (V_2O_5 -1) frozen with liquid N_2 , revealing the characteristic peaks of hexagonal ice.^[125] (b) Schematic depiction of the growth kinetic of hexagonal ice, leading to plate-like ice crystals, as adapted from the scheme of Deville.^[58] (a) is adapted and reprinted with permission from Knöller *et al.*,^[20] Copyright 2017, Springer Nature.

In detail, the formation of the sophisticated lamellar microstructures of V_2O_5 -1 scaffolds is achieved through the synergistic contributions of (i) the physics of ice, (ii) the freezing conditions, (iii) the chemistry of the system and (iv) the mechanical flexibility of the used nanofibers.^[68] XRPD analysis on a instantly frozen sample revealed that the ice crystals exist in its hexagonal modification (figure 5.7a).^[125] Due to the growth kinetics of hexagonal ice, the growth rate in the a -directions is about two orders of magnitude faster than the growth in the c -direction, leading to plate-shaped ice crystals (figure 5.7b).^[58] Moreover, if the temperature gradient, meaning the driving force for the ice crystal growth, is pronounced in one predominant direction, the ice crystals expand also differently in different a -directions. When freezing the V_2O_5 nanofiber suspension with liquid N_2 , these crystal plates exhibit a thickness of about $5\ \mu\text{m}$, a width of tens of micrometers and a length of several hundreds of micrometers. Zhang *et al.*^[69] correlated the average spacing (meaning the ice-crystal thickness) with the freezing rate for poly(vinyl alcohol) in water, as displayed in figure 5.8. Extrapolating their power-law relation towards the lamella distance found in the V_2O_5 scaffolds ($5\ \mu\text{m}$) leads to an estimated freezing speed of $375\ \mu\text{m/s}$. Most commonly reported freezing speeds are in the range of 1 - $100\ \mu\text{m/s}$ and result in lamella distances that are one order of magnitude larger than in the here presented ice-templated scaffolds, highlighting this sophisticated microstructure.^[22]

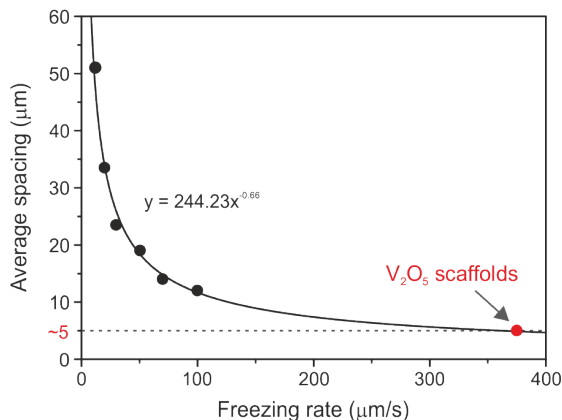


Figure 5.8: Average lamella spacing as a function of freezing rate of poly(vinyl alcohol) in water, extracted from the work of Zhang *et al.* [69]. The fitted curve extrapolates the estimated freezing speed, which led to a lamella distance of about $5\ \mu\text{m}$ within the V_2O_5 scaffolds, indicated by the red point.

The formation of the V_2O_5 lamellas is complemented by the appearance of regularly arranged nanofiber pillars, which interconnect neighboring lamellas. While the lamellas were compacted between the ice crystal plates, the nanofiber pillars were trapped within the plates, as depicted in figure 5.9a. Deville *et al.* [63] investigated the formation of ice crystal plates, which grew in a colloidal silica suspension, using X-ray computed tomography. Extracted from their work, such an ice crystal plate features a smooth surface on the bottom, while the top is covered with a regular arrangement of vertically oriented dendrites (ridges). In addition, the ice crystal plate exhibits several round crystal tips lined up along its front (figure 3.6). In the freezing zone these tips are surrounded by randomly distributed V_2O_5 nanofibers (figure 5.4). As the nanofibers interact with the ice crystal surface *via* H-bonds, they get attached also in the gaps between adjacent tips, which are geometrically oriented in *c*-direction. Therefore, the attached nanofibers exhibit likewise a predominant orientation parallel to the *c*-direction, in which they become trapped within the ice crystal plate in the frozen zone. The fact that the instant freezing with liquid N_2 results in a lamella distance of about $5\ \mu\text{m}$ correlates well with the maximum length of the fabricated V_2O_5 nanofibers. The similar dimensions allow the nanofiber assemblies to fully bridge the distance between the lamellas in the resulting scaffolds. This structural feature of the scaffolds is highlighted with dashed

yellow lines in figure 5.9b. They display the widths (several tens of micrometers) of some ice crystal plates, proving the presence of numerous pillars within each plate. In addition, while the geometry of the crystal tips is responsible for the pillar formation, the unequal surface configuration of the ice crystal plate's top and bottom is responsible for structural variations along the pillars, which can be seen in figures 5.5e,f. The upper part of the pillars exhibits a highly concentrated nanofiber network, evolving in fewer straight nanofiber bundles towards the lower end. The smooth bottom of one plate and the dendritic top of a second plate,^[63] which is located directly below, form small coniform cavities. These cavities serve as collecting basins for the V_2O_5 nanofibers, resulting in a higher V_2O_5 nanofiber concentration at the top part of the pillars. With all their detailed structural features, the V_2O_5 -1 scaffolds closely adapted the structure of the ice crystal plates.

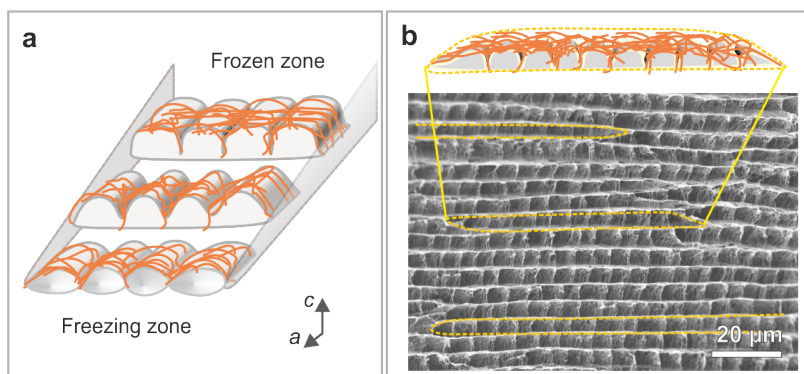


Figure 5.9: (a) V_2O_5 nanofibers arrange perpendicular to the ice crystal's growth direction between neighboring tips of one ice crystal plate and get trapped, as the freezing front proceeds. (b) Resulting V_2O_5 scaffold (V_2O_5 -1) revealing the perpendicular nanofiber arrangements in the form of regularly distributed pillars within the ice crystal plates. This figure is adapted and reprinted with permission from Knöller *et al.*,^[20] Copyright 2017, Springer Nature.

5.2.3 Artificial Cuttlebone

The resulting V_2O_5 -1 scaffolds exhibit a regular lamellar structure with interconnecting pillars (figures 5.5c-f) and a water content of 13.47 wt.%, as obtained by TGA measurements (figure 5.19, see also section 5.3.2). It therefore not only

exhibits a microstructure similar to the one of natural cuttlebone (figure 3.2d), but also a certain amount of soft fraction, analog to the organic phase within the aragonite-based cuttlebone.^[14] However, there are several differences between the two related microstructures. Most obvious, both microstructures strongly differ in lamella orientation and size of the microstructural features. While the lamellas in cuttlebone exhibit one preferred orientation, the centrosymmetric arrangement of the lamellas within the V_2O_5 -1 scaffolds shows all kinds of orientations. A recent publication reports highly anisotropic lamellar microstructures and disclose their strongly orientation dependent mechanical performance.^[73] But, these porous materials lack in interconnecting pillars, the structural features, which provide natural cuttlebone with predominantly isotropic mechanical stability.^[14] Since the V_2O_5 -1 scaffolds also exhibit such supporting pillars, a comparable orientation insensitivity could be likewise expected.

Table 5.1: Structural parameters of V_2O_5 scaffolds and natural cuttlebone.

Sample	Porosity (%)	Lamella thickness (nm)	Lamella distance (μm)
V_2O_5 -0	99.8	-	-
V_2O_5 -1	99.8	58.0 ± 6.0	5.3 ± 0.5
V_2O_5 -2	99.7	84.6 ± 7.7	5.1 ± 0.5
V_2O_5 -3	99.5	120.0 ± 19.8	5.5 ± 0.9
Cuttlebone	92.7	7000 ± 1387	317.2 ± 30.9

The lamella thickness of the V_2O_5 -1 scaffolds (figures 5.5c-f) is 58.0 ± 6.0 nm and the interlayer distance is 5.3 ± 0.5 μm , which would be about 120 and 60 times smaller than what was found in natural cuttlebone (table 5.1), respectively. This downscaling might be beneficial in terms of mechanical stability, analog to cuttlebone species, which are domiciled in greater depths than the *sepia officinalis* used in this work.^[15,17] The difference in dimension is accompanied by a difference in porosity. While natural cuttlebone has a porosity of 92.7%, the V_2O_5 -1 scaffolds reach a porosity of 99.8% (table 5.1). The latter is given by the used concentration of the V_2O_5 nanofiber suspension (C1). The scaffolds' porosity was calculated using their density (as derived from each sample's weight and volume) and the density of the cell walls, which equals the density of the hydrated V_2O_5 nanofibers (2.78 g/cm^3).^[35] Dividing the scaffolds' density by

the wall density results in the scaffolds' relative density ρ_{rel} , which further leads to the value for the porosity P *via* equation 5.1.^[126]

$$P = (1 - \rho_{rel}) \cdot 100 \quad (5.1)$$

The porosity of the V_2O_5 -1 scaffolds can be seen as total porosity, comprising the microscopic pores (the stacked cavities) as well as the porosity of the scaffolds' walls (permeable lamellas and pillars), yielding a specific surface area of $121 \text{ m}^2/\text{g}$, obtained by BET. This value is in the range of previously reported porous V_2O_5 materials,^[51,52,57] being especially close to the one reported by Zhu *et al.*^[52] ($133 \text{ m}^2/\text{g}$). Such a 3D structure was constructed from V_2O_5 nanosheets, which were also assembled *via* ice-templating (frozen with liquid N_2). However, the resulting structure strongly differs from the here presented hierarchically organized cuttlebone-like microstructure (V_2O_5 -1). In fact, the V_2O_5 nanosheet assembly shows a similar random microstructure with undirected pores as graphene sponges, ice-templated at -170°C .^[65] In both cases the porous structures were fabricated by freezing gels, which contained sheet-like nanostructures. It can be assumed that the fast freezing at low temperatures does not give the nanosheets within the gels enough time to rearrange and follow the shape of the forming ice crystals. More likely the nanosheet assemblies within the gels guide the ice crystals' shapes. Comparing the V_2O_5 nanosheet assembly to the here reported V_2O_5 -1 scaffolds therefore highlights the sensitivity of structural evolution to parameters such as viscosity and nanostructure shape. Surveying liquid N_2 -induced ice-templating of aqueous suspensions of other fiber-like nanostructures, including cellulose microfibrils^[67] and multi-walled carbon nanotubes-chitosan^[66] (MWCNT/CHI), revealed that these scaffolds display comparable lamellar microstructures. Especially the MWCNT-based scaffolds exhibited a predominantly regular distribution of interconnecting pillars,^[66] similar to the V_2O_5 -1 scaffolds and natural cuttlebone. This finding further verifies the impact of viscosity and nanostructure shape on the ice-templating approach and simultaneously addressing another important factor, namely the surface chemistry of the fiber-like nanostructures. Carbon nanotubes (CNTs) are naturally hydrophobic, thus would strongly agglomerate in water. Surface functionalization with nitric acid, as in the case of the MWCNTs,^[66] introduces oxygen-containing functional groups on the surface of the nanotubes.^[127] Such a surface functionality allows dispersing the MWCNTs in water and enables their interaction with the forming ice crystals *via* H-bonds,

as also observed in the case of the V_2O_5 nanofibers. The MWCNT/CHI- as well as the V_2O_5 -1 scaffolds exhibit porous scaffold walls, embodying another difference from natural cuttlebone, which exhibits predominantly dense lamellas and pillars. In order to approach the density of natural cuttlebone and mimic its dense lamellas and pillars more closely, the V_2O_5 nanofiber concentration was increased by factors of 2 (V_2O_5 -2) and 4 (V_2O_5 -3), respectively, prior to the ice-templating process. Such an increase in the V_2O_5 nanofiber concentration was achieved by varying the water volume in the synthesis protocol of the V_2O_5 nanofibers (section 4.1.1). After two weeks of growth, the resulting nanofiber concentration exhibits an exponential relation to the used volume of water (figure 5.10). This trend arises, because the probability that two monomers or oligomers meet drastically increases with decreasing water volume, meaning space. The latter therefore facilitates the nanofiber formation.

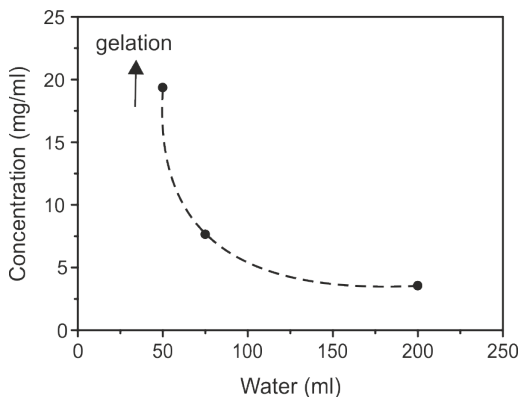


Figure 5.10: Exponential relation between the water volume, used for the synthesis, and the final V_2O_5 nanofiber concentration after two weeks of growth. A further decrease of water volume, would lead to gelation of the nanofiber suspension, as indicated by the arrow.

Figure 5.11 shows the evolution of the V_2O_5 scaffolds' microstructure upon increasing the nanofiber concentration. All samples exhibit the desired cuttlebone-like microstructure with a comparable lamella distance. Latter arises because the freezing condition, meaning the ice crystal dimensions, were the same for all three different samples. However, the samples strongly differ in lamella thickness, which increased from $58.0 \pm 6.0 \mu\text{m}$ to $120.0 \pm 19.8 \mu\text{m}$ along with the nanofiber concentration (table 5.1). Moreover, the connection between lamel-

las and pillars becomes more pronounced (figures 5.11d-f), which should have a positive impact on the mechanical stability of the scaffolds. With the increase in nanofiber concentration the porosity of the scaffold walls becomes reduced, thus reduce the scaffolds' overall porosity. Thereby, the concentration and resulting porosity exhibit a linear relation, similar to other ice-templated, ceramic-based scaffolds.^[58]

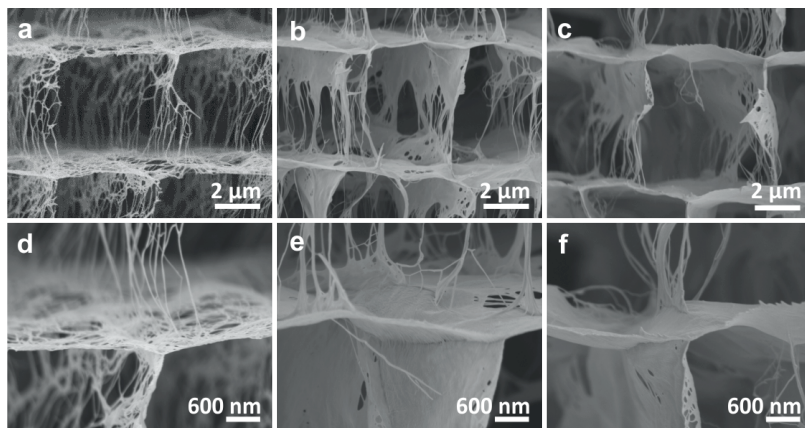


Figure 5.11: (a-c) SEM images of cuttlebone-like V_2O_5 nanofiber scaffolds prepared with different concentrations: (a) C1 = 3.5 mg/ml (V_2O_5 -1); (b) C2 = 7.6 mg/ml (V_2O_5 -2) and (c) C3 = 14.5 mg/ml (V_2O_5 -3). (d-f) Corresponding SEM images at higher magnification, showing the detailed structure of the scaffolds' lamellas and the pillars. This figure is adapted and reprinted with permission from Knöller *et al.*,^[20] Copyright 2017, Springer Nature.

Plotting the lamella thickness and distance as a function of sample porosity (figure 5.12) visualizes that the lamella thickness increases linearly, while the lamella distance stays constant. As the microscopic porosity is unaffected, the decrease in overall porosity is attributed to a reduced wall porosity that can be also seen in figures 5.11a-c. Even though the density of the scaffold walls is shown to be tailorable towards natural cuttlebone, an increase in V_2O_5 nanofiber concentration by a factor 4 leads only to a slight decrease of 0.3% in porosity. This porosity is still much higher than the one of natural cuttlebone. A further decrease of water volume in the synthesis protocol would result in highly concentrated V_2O_5 nanofiber suspensions, but at the same time would lead to gelation (figure 5.10). Such gels are difficult to cast and, in addition, could yield an alternative microstructure. The latter could arise, as the ice

crystals might be sterically hindered to channel through the gel upon freezing, similar to the fabrication of graphene sponges^[65] and 3D structured V_2O_5 ^[52] from their gels. As the used V_2O_5 nanofiber synthesis protocol limits the possible minimum scaffold porosity, approaching the density of natural cuttlebone closely would not be possible with this approach.

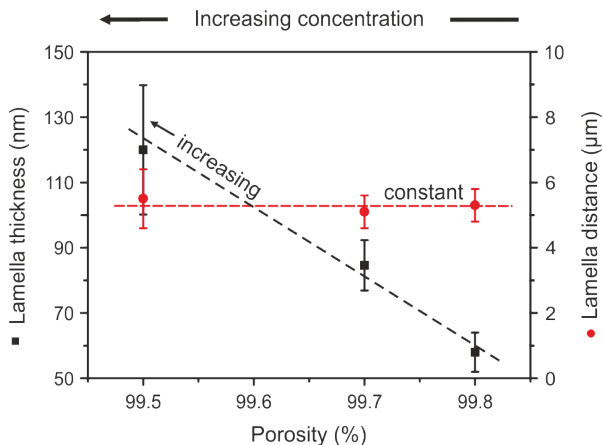


Figure 5.12: Lamella thickness and distance plotted over the samples porosity, as prepared from V_2O_5 nanofiber suspensions of different concentrations.

5.2.4 Structure-Mechanics Relation

In order to investigate the microstructural influence on the mechanical performance of the V_2O_5 scaffolds, uniaxial compression tests were conducted on samples, which exhibit the cuttlebone-like microstructure (V_2O_5 -1), compared to randomly oriented reference samples (V_2O_5 -0). Figure 5.13 displays the stress-strain curves of the two different samples, correlated to their microstructures. Samples V_2O_5 -1 exhibit a compressive strength, which is about doubled, compared to the one of V_2O_5 -0. The Young's modulus exhibits even a tenfold enhancement (table 5.2). This enhancement originates from the combination of the scaffold walls' configuration and the pore size as well as from the pore geometry. V_2O_5 -0 exhibit strongly inhomogeneous scaffold walls with poorly connected areas, which act as weak points. Their random pore geometry and comparably larger size makes them further prone to collapsing, leading to lower

values of Young's modulus.^[128,129] V_2O_5-1 , on the other hand, show a more regular scaffold wall structure and the ordered, close-to-rectangular units of the scaffolds provide a more sufficient stability.^[130] In addition, the comparably smaller pore sizes minimize shear,^[17] further enhancing the mechanical stability. As both types of samples were fabricated from suspensions with the same nanofiber concentration, they exhibit the same calculated porosity. The difference in mechanical performance solely comes from the variation of the microstructure, proving the superiority of the cuttlebone-like design.

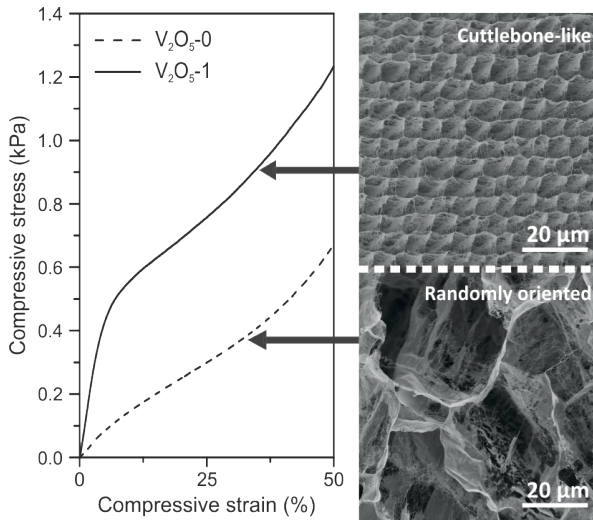


Figure 5.13: Stress-strain curves of cuttlebone-like V_2O_5-1 , compared to randomly oriented V_2O_5-0 , which exhibits the same porosity. The two curves are correlated to the samples' microstructures, as observed by SEM. This figure is adapted and reprinted with permission from Knöllner *et al.*,^[20] Copyright 2017, Springer Nature.

Structural modulation *via* increasing the solid load (figure 5.11) allows further tuning the mechanical performance of the V_2O_5 scaffolds. Figure 5.14a displays the stress-strain curves of the three samples with variation in initial V_2O_5 nanofiber concentration. Their courses show pronounced similarities to stress-strain curves of other cellular solids.^[76] In general, such curves can be divided into 3 different regimes, (i) linear elastic deformation, (ii) plateau with predominant constant stress and (iii) densification (figure 3.7).

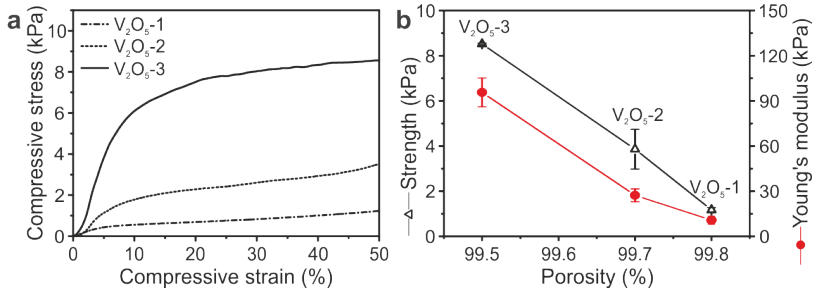


Figure 5.14: (a) Stress-strain curves of the cuttlebone-like V_2O_5 scaffolds of different initial nanofiber concentration. (b) Compressive strength and Young's modulus of the corresponding samples. This figure is adapted and reprinted with permission from Knöller *et al.*,^[20] Copyright 2017, Springer Nature.

(i) At lower compressive strains, the scaffold walls slightly bend and the scaffolds behave linear-elastic. The linear increase of the stress-strain curves in this regime represents the Young's modulus. Ashby^[76] proposed a correlation between a scaffold's/foam's relative Young's modulus and its relative density, which is given by equation 3.4. This correlation is subject in several publications.^[71–73,128] They all show a decrease in Young's modulus with increasing porosity, analog to the V_2O_5 scaffolds. A twofold and fourfold increase in V_2O_5 nanofiber concentration causes a decrease in porosity, which leads to steeper linear-elastic regimes alongside with an increase in Young's modulus of about one order of magnitude from V_2O_5 -1 to V_2O_5 -3 (figure 5.14b).

(ii) The first regime is followed by a regime, in which the stress-strain curves have a more leveled slope. Similar to equation 3.4, Ashby postulated a correlation between a ceramic scaffold's/foam's relative crushing strength and its relative density *via* equation 3.5.^[76] Analog to the trend of the Young's modulus, also the compressive strength increases with decreasing porosity (figure 5.14b). However, even though the V_2O_5 scaffolds are assembled from ceramic nanofibers, brittle crushing such as in natural cuttlebone (figure 5.2) could not be observed, making equation 3.5 invalid for this type of ceramic scaffolds. The single V_2O_5 nanofibers exhibit a pronounced mechanical flexibility and are insensitive to flaws, as already discussed in section 5.2.1, unlocking alternative deformation mechanisms to brittle crushing. Thereby, three major deformation mechanisms could be identified, which are displayed in figure 5.15. Some

lamellas smoothly compacted, whilst the surrounding lamellas appear to stay intact, comparable to what was observed in natural cuttlebone.^[14] This deformation mechanism preferably occurs in areas where the lamellas are oriented predominantly perpendicular to the direction of compression (figures 5.15a,b). If the lamellas are mainly oriented parallel to the direction of compression, tensile stresses can arise between single lamellas, thus rip them apart (figures 5.15c,d). This splitting could initiate mechanical failure of the complete scaffold, when the compression proceeds. Diagonal lamella orientation mostly leads to bending/folding and sliding effects (figures 5.15e,f). The latter is most likely accompanied by breaking of the pillars that interconnected the different lamellas. Since the V_2O_5 scaffolds exhibit all kinds of lamella orientations (figure 5.6), all identified deformation mechanisms coexist and contribute to the energy dissipation upon deformation.

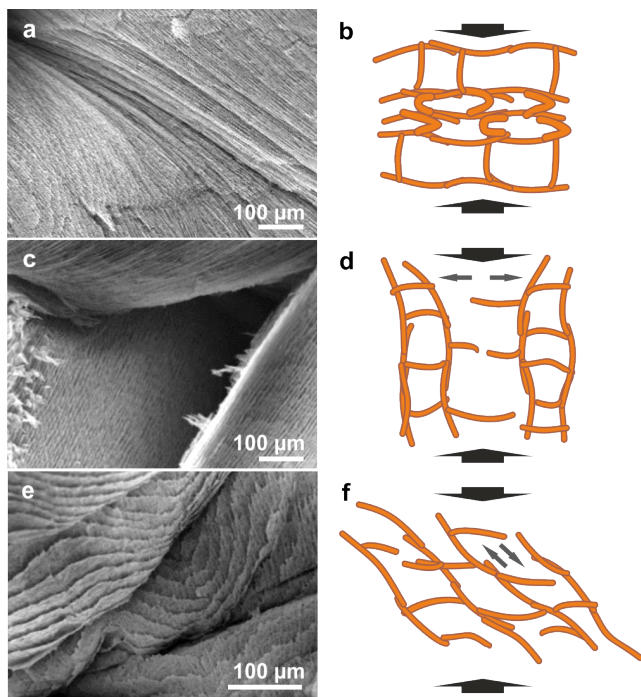


Figure 5.15: Different deformation mechanisms in V_2O_5 scaffolds (V_2O_5 -1) depending on the direction load is applied: (a,b) local compaction, (c,d) splitting of lamellas and (e,f) bending/folding and sliding of lamellas.

(iii) Following the deformation regime, the final regime represents the densification of the material, at which the slope of the stress-strain curves is becoming again steeper. Accordingly, the foams start approaching the mechanical characteristics of a bulk material.^[76] Owing to the fact that the V_2O_5 scaffolds exhibit an ultrahigh porosity (table 5.1) and the compression tests were conducted to only 50 % compressive strain, which is still in the deformation regime, the corresponding stress-strain curves do not show any pronounced densification.

Comparing the mechanical performance of the V_2O_5 scaffolds to the one of other lamellar ceramic-based scaffolds,^[71–74] reveals that the V_2O_5 scaffolds exhibit the lowest Young’s modulus, but at the same time by far the highest porosity (figure 5.16a). These pronounced differences in porosity make it difficult to assess the mechanical properties of the different types of scaffolds. One way to exclude the influence of the porosity for this assessment would be to compare the mechanical performance of the scaffolds’ cell walls by transforming equation 3.4 towards E_S , the Young’s modulus of the scaffold walls (wall modulus), in equation 5.2:

$$E_S = \frac{E}{C_2 \cdot \left(\frac{\rho}{\rho_S}\right)^2} \quad (5.2)$$

Figure 5.16b displays the wall moduli of the three different V_2O_5 scaffolds compared to the one of natural cuttlebone and highly porous Al_2O_3 -based scaffolds.^[72] The wall modulus of the V_2O_5 scaffolds increases from 2.68 ± 0.62 GPa (V_2O_5 -1) to 4.15 ± 0.42 GPa (V_2O_5 -3) with the increasing lamella thickness and the decreasing of scaffold wall porosity. The latter value approaches the Young’s modulus (4.8 GPa) measured for 11 μm thick papers composed of randomly oriented V_2O_5 nanofibers.^[131] This value is likewise comparable to the wall modulus found for natural cuttlebone (table 5.2), in which the structural features are also several micrometers in thickness (table 5.1).

Lin-Gibson *et al.*^[132] investigated the influence of porosity and strut (cell wall) thickness on the mechanical stability of randomly pored dimethacrylate-based scaffolds. They observed that an increase in porosity and an increase in strut thickness led to an opposed influence of the Young’s modulus. While the increasing porosity reduces the mechanical stability, analog to the discussion above, an increase in strut thickness increases the mechanical stability. Both investigated parameters allowed to tune the mechanical performance, however the porosity

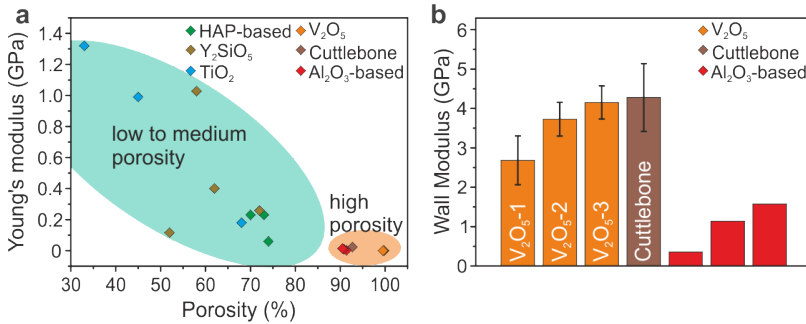


Figure 5.16: (a) Young's modulus as a function of porosity of various lamellar, ceramic-based scaffolds.^[71–74] (b) Wall modulus of the V₂O₅ scaffolds, natural cuttlebone and Al₂O₃-based scaffolds (high porosity scaffolds).^[72] This figure is adapted and reprinted with permission from Knöller *et al.*,^[20] Copyright 2017, Springer Nature.

embodies the major influencing factor. Their findings are consistent with the mechanical behavior of the V₂O₅ scaffolds. This behavior was also observed in case of the Al₂O₃-based scaffolds.^[72] Three different scaffolds were fabricated from different Al₂O₃ particle sizes: 400 nm, bimodal 400 nm and 10 μm (30:70) and 10 μm. The scaffold containing the 400 nm large particles exhibited the highest overall porosity as well as the thickest scaffold walls, but also the lowest Young's modulus (2.62 MPa). The scaffolds containing the 10 μm large particles exhibited the opposing trend with the highest Young's modulus modulus (14.22 MPa). Applying equation 5.2, results in wall moduli of 0.35 GPa and 1.58 GPa, respectively. It appears that using larger Al₂O₃ particles is advantageous for the mechanical stability of the scaffold walls, minimizing interfaces, which seems to be the weak point of this system.

Compared to the Al₂O₃-based scaffolds,^[72] the V₂O₅ scaffolds exhibit by far superior wall moduli. Even though both types of scaffolds were fabricated in a similar way (using ice-templating) and were not thermally post-treated, the different wall moduli most likely arise from differences in composition and microstructure. While the V₂O₅ scaffolds have only water as soft fraction incorporated, the Al₂O₃-based scaffolds contain chitosan and gelatin at a comparably higher volume fraction, reducing the wall modulus of the composite. Moreover, the ice-templating of this ternary mixture led to a predominantly inhomogeneous lamellar microstructure and only a few irregularly distributed

interconnecting walls between the lamellas. However, as known from natural cuttlebone, a regular ordering of the structural features is crucial for an enhanced mechanical performance, as it is proven by the cuttlebone-like V_2O_5 scaffolds.

Table 5.2: Mechanical parameters of V_2O_5 scaffolds and natural cuttlebone.

Sample	Strength (kPa)	Young's modulus (kPa)	Wall modulus (GPa)
V_2O_5 -0	0.63 ± 0.15	1.73 ± 0.71	0.43 ± 0.18
V_2O_5 -1	1.17 ± 0.10	10.73 ± 2.49	2.68 ± 0.62
V_2O_5 -2	3.86 ± 1.20	27.24 ± 4.26	3.73 ± 0.43
V_2O_5 -3	8.52 ± 0.04	95.66 ± 9.58	4.15 ± 0.42
Cuttlebone	1171 ± 125	22857 ± 4598	4.29 ± 0.86

5.3 Towards All-Ceramic Scaffolds

As mentioned in section 5.2.2, the ice-templating of the V_2O_5 nanofibers occurs in the absence of any additive, such as binder, leading to self-supporting scaffolds. Thermal post-treatment such as sintering is therefore redundant. However, in terms of technical applications, including LIBs,^[26,30] the presence of water could have a negative influence on the functionality^[133] of the V_2O_5 , making the impact of thermal post-treatment on the V_2O_5 scaffolds worth investigating.

5.3.1 Thermal Stability

The macroscopic impact of thermal post-treatment on the V_2O_5 scaffolds was investigated using optical dilatometry. The initially detected black area, which corresponds to the sample size (figure 5.17a) stayed nearly constant up to 400 °C (figure 5.17b). Exceeding this temperature led to a drastic shrinkage of the sample (figure 5.17c). The corresponding shrinkage curve in figure 5.17d exhibits a maximum value of about 45 % after 550 °C.

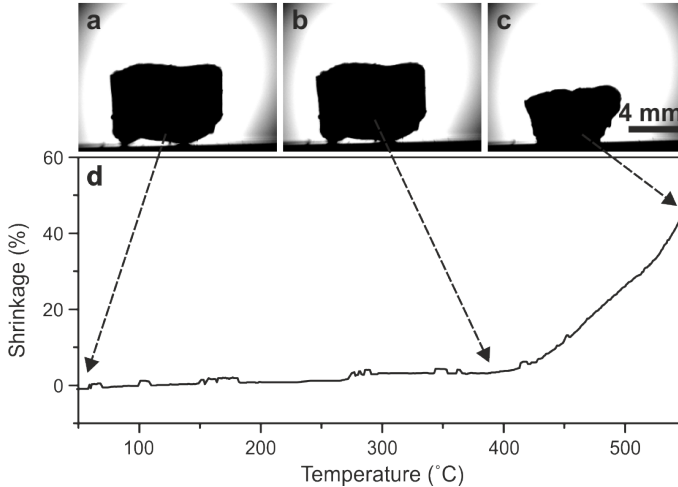


Figure 5.17: (a-c) Evolution of a V_2O_5 -1 scaffold's macroscopic shape, obtained by optical dilatometry. (d) Corresponding shrinkage curve.

Shrinkage is a typical phenomenon when sintering green bodies, which occurs usually at homologous temperatures $T_H (= \frac{T}{T_s})$ between 0.7 and 0.8 for oxide ceramics.^[134] The melting temperature T_s of V_2O_5 is 690°C ^[30] and therefore the sintering temperature results in values between 483 and 552°C , correlating well with the pronounced shrinkage in figure 5.17d. Sintering not only affects the macroscopic shape, but also changes the microstructure, obtained by SEM (figure 5.18). As the initial porosity of the V_2O_5 -1 scaffolds is 99.8% (table 5.1), a macroscopic volume shrinkage of about 45% of the V_2O_5 scaffolds does not result in a compact material, they still exhibit a pronounced porosity. Moreover, even though the lamellar microstructure of the cuttlebone-like V_2O_5 scaffolds is still partially visible (figures 5.18a,b), the defined pillars of the as-prepared scaffolds mostly vanished and the lamellas got transformed into a branched network (figure 5.18c), in which the V_2O_5 nanofibers completely lost their identity. They now appear as chains of predominantly rectangular nanocrystals (figure 5.18d), which correlates with the orthorhombic crystal structure of phase pure V_2O_5 .^[35] These findings indicate that the V_2O_5 scaffolds sinter alongside with a phase transformation, which is further underscored by the fact that the scaffolds underwent a color change from red-brown (figure 5.6b) to bright yellow (figure 5.21a).

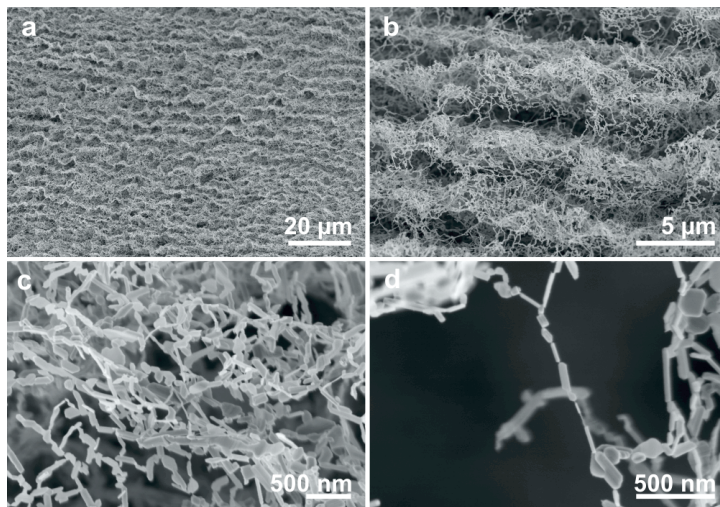


Figure 5.18: SEM images of a V_2O_5 -1 scaffold after heating to 600 °C: (a) Lamellar microstructures still partially present, (b,c) lamellas and pillars strongly differ from the initial microstructure, (d) nanofibers lost their identity.

5.3.2 Phase Transformation

Simultaneous TGA and DSC analysis was conducted to investigate the phase change of the V_2O_5 -1 scaffolds upon thermal post-treatment. The TGA curve in figure 5.19 exhibits a total weight loss of 13.47 wt.%, corresponding to the removal of water. The as-prepared V_2O_5 scaffolds therefore contain 1.6 mol water per V_2O_5 unit ($V_2O_5 \cdot 1.6H_2O$). The weight loss occurs in two steps, analog to observations reported by Livage.^[41] The first step, which reaches a plateau at about 150 °C, is assigned to the removal of physisorbed water. This type of loosely bound water is located within the double-layered structure of the V_2O_5 nanofibers, as already mentioned in section 5.2.1, and is reversibly intercalatable.^[135] After heating to 150 °C the scaffolds exhibit the composition $V_2O_5 \cdot 0.8H_2O$. Further increasing the temperature led to the second step, which is assigned to the removal of chemisorbed water.

This second step is accompanied by two phase transitions, as obtained by DSC (figure 5.19). The curve exhibits two temperature dependent exothermic peaks at 295 and 339 °C. The first peak is associated with cross-linking of the single

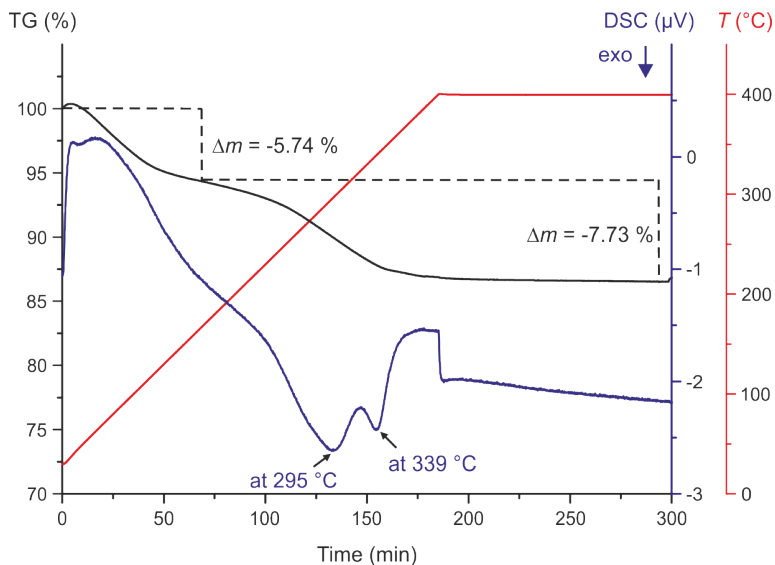


Figure 5.19: TGA and DSC curve of V_2O_5 -1 scaffolds revealing a water loss in two steps as well as two phase transitions. This figure is adapted and reprinted with permission from Knöller *et al.*,^[118] Copyright 2018, American Chemical Society.

V_2O_5 nanofibers *via* a polycondensation reaction,^[41] converting V-O-H bindings into V-O-V ones. Owing to the fact that the V-O bonds (dissociation energy $D_0 = 644(21)$ kJ/mol)^[136] are more stable than the initial O-H bonds (dissociation energy $D_0 = 428(21)$ kJ/mol),^[136] the V-O bond formation occurs exothermally, yielding amorphous V_2O_5 scaffolds. Further increase in temperature initiates recrystallization into phase pure, orthorhombic V_2O_5 ,^[135] which corresponds to the second exothermic peak in the DSC curve. Complementary, *ex situ* XRPD measurements were carried out on V_2O_5 scaffolds directly after fabrication (as-prepared) and thermally treated scaffolds (2 h at 150 °C and 2 h at 350 °C). The temperatures of the thermally treated scaffolds were chosen on the base of the previous TGA/DSC results. Figure 5.20a displays the XRPD pattern of the differently post-treated V_2O_5 scaffolds. The as-prepared V_2O_5 scaffolds exhibit a broad peak at 8.587°. This peak position 2θ is connected to the interlayer distance d within the V_2O_5 nanofibers *via* the Bragg equation.^[115] Applying equation 3.10 leads to an interlayer distance of 10.3 Å for the as-prepared V_2O_5 scaffolds. As already mentioned in section 5.2.1, Li-

vage^[41] investigated the interlayer distance as a function of water fraction in $V_2O_5 \cdot nH_2O$ xerogels. Their initial water fraction accounted for $V_2O_5 \cdot 1.8H_2O$ and an interlayer distance of 11.5 \AA , when drying the V_2O_5 nanofiber suspension to fabricate a xerogel. Both, water fraction and interlayer distance, can be tuned by either increasing the humidity or thermally treating the xerogel. While first leads to an increase in both features, the latter decreases them. His findings are displayed in figure 5.20b.^[41] The as-prepared scaffolds with the interlayer distance of 10.3 \AA and the composition $V_2O_5 \cdot 1.6H_2O$, which equals 13.47 wt.% water, is in good agreement with the correlation found by Livage. The water fraction of the V_2O_5 scaffolds is lower than the one obtained for the xerogels, revealing that the sublimation of water in the drying step, which involves vacuum, is more efficient in the removal of physisorbed water. Annealing the V_2O_5 scaffolds for 2 hours at 150°C led to a shift of this first peak from 8.578° to 8.734° (10.1 \AA), implying a loss of water (figure 5.20a). After 2 hours at 350°C this peak completely vanished due to the complete removal of water. At the same time three new peaks arose, corresponding to the orthorhombic V_2O_5 phase with the space group $Pmmn$.^[34,35]

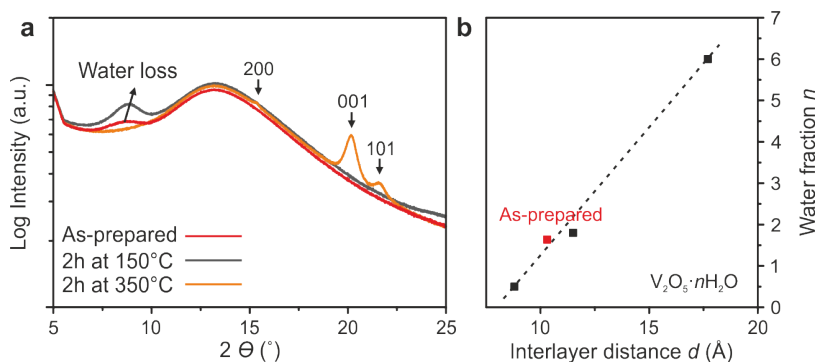


Figure 5.20: (a) *Ex situ* XRPD spectra of the V_2O_5 -1 scaffolds showing the structural evolution upon thermal post-treatment after 2 hours at 150 and 2 hours at 350°C , respectively. (b) Correlation between the $V_2O_5 \cdot nH_2O$ xerogel's interlayer distance d and its water fraction n , according to the observations of Livage.^[41] (a) is adapted and reprinted with permission from Knöller *et al.*,^[118] Copyright 2018, American Chemical Society.

5.3.3 Phase Pure V_2O_5 Scaffolds

As a result of optical dilatometry, TGA/DSC and XRPD measurements the V_2O_5 scaffolds annealed at $350\text{ }^\circ\text{C}$ (V_2O_5 -1A) were further investigated in terms of microstructural and mechanical analysis. Figure 5.21a shows such a phase pure V_2O_5 -1A scaffold. It exhibits macroscopically the same dimensions as the untreated scaffolds, suitable for mechanical characterization. This shape stability is guaranteed, as the chosen temperature does not reach the sinter temperature discussed in section 5.3.1.

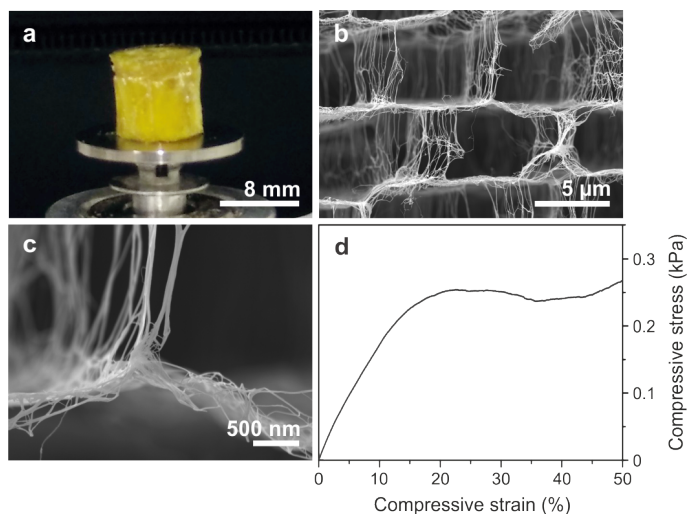


Figure 5.21: (a) Optical photograph of a V_2O_5 -1 scaffolds after annealing at $350\text{ }^\circ\text{C}$ (V_2O_5 -1A). SEM images showing that (b) the cuttlebone-like structure is preserved and (c) the V_2O_5 nanofiber assemblies are fused together. (d) Corresponding stress-strain curve of a V_2O_5 -1A scaffold. This figure is adapted and reprinted with permission from Knöller *et al.*,^[118] Copyright 2018, American Chemical Society.

Structural investigation using SEM revealed that the cuttlebone-like microstructure is also preserved (figure 5.21b). However, closer inspection of the microstructure shows that the V_2O_5 nanofiber assemblies of the annealed scaffolds appear to be fused together, but the fibrous nature is still visible (figure 5.21c). Comparing this microstructure to the one annealed at $600\text{ }^\circ\text{C}$ (figure 5.18) indicates that even though DSC and XRPD show peaks at $350\text{ }^\circ\text{C}$ corre-

lated to crystalline V_2O_5 , the majority of the scaffolds is still amorphous. This assumption also explains the presence of the big and broad scattering peak in the XRPD pattern, which does not vary with thermal post-treatment (figure 5.20).

The V_2O_5 -1A scaffolds were mechanically investigated using uniaxial compression tests, as displayed in figure 5.21d. The curve shows a similar progression as observed for the untreated scaffolds V_2O_5 -1 (figure 5.14a), but exhibits comparably lower values in mechanical parameters. The strength and Young's modulus amount to 0.20 ± 0.04 kPa and 2.17 ± 0.99 kPa, respectively. However, at the same time the porosity increases to 99.9%, as the macroscopic dimensions stay constant, while the mass decreases due to the removal of water. In order to compare the mechanical performance independently from the porosity, equation 5.2 was again applied, leading to a wall modulus of 2.63 ± 1.20 GPa. This value conforms to the wall modulus of the initial V_2O_5 -1 scaffolds (2.68 ± 0.62 GPa), implying that the water within the nanofibers, respectively its removal, has no significant influence on the stiffness/flexibility of the scaffold walls.

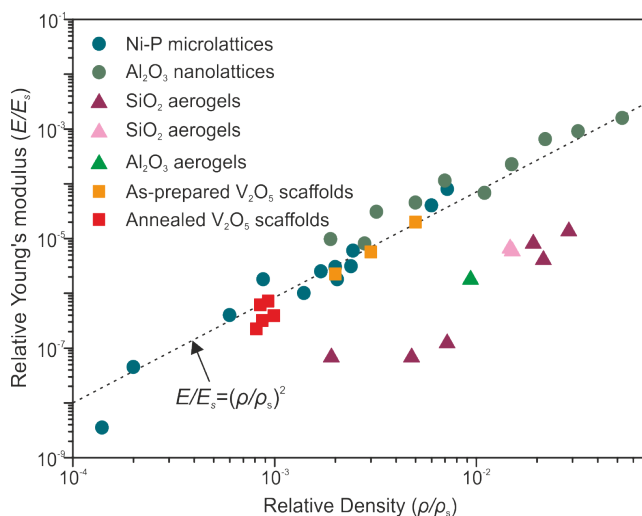


Figure 5.22: Ashby plot of highly porous microstructures. The Ni-P microlattices,^[137] the Al_2O_3 nanolattices^[138] and the V_2O_5 scaffolds exhibit ordered microstructures, while the SiO_2 ^[139,140] and Al_2O_3 aerogels^[140] exhibit random microstructures. This figure is adapted and reprinted with permission from Knöllner *et al.*,^[118] Copyright 2018, American Chemical Society.

Comparing the mechanical properties of the V_2O_5 -1A (and as-prepared) scaffolds to other ultra-porous lattices^[137,138] and aerogels^[139,140] in an Ashby plot (figure 5.22) reveals that all materials, which exhibit a highly ordered microstructure, nicely follow the correlation postulated by Ashby^[76] (equation 3.4) for the idealized isotropic 3D model of a cubic cell geometry with open cell walls. In addition, they exhibit a superior mechanical stability, as compared to the ceramic aerogels, which featured a random microstructure. This superiority is attributed to the hierarchically structuring of the lattices (which are inspired by diatoms^[141] and radiolarians^[142]) and scaffolds, analog to the one of their biological role models.^[14,137,143]

Figure 5.22 effectively demonstrates that the all-ceramic V_2O_5 -1A scaffolds with their porosity of 99.9% and excellent mechanical stability play in the major league of ultraporous structural materials.

5.4 Dynamic Mechanical Behavior

The previous sections demonstrated the successful implementation of V_2O_5 scaffolds with enhanced mechanical properties inspired by the microstructure of natural cuttlebone. The use of V_2O_5 nanofibers, which are mechanically flexible (figure 5.3a), opens further mechanical characteristic beyond bioinspiration. Their assembly into a highly porous, filigree microstructure renders the scaffolds to be a good mechanical damping material, as it will be discussed in detail in the following.

5.4.1 Elastic Deformation

Conventional ceramics are known to be stiff and brittle, making them prone to abrupt mechanical failure when being exposed to mechanical shock or vibrations. This is not the case for the here presented V_2O_5 scaffolds. Section 5.2.4 already opened the discussion about the atypical compressive behavior of the scaffolds and alternative deformation mechanisms, compared to brittle ceramics scaffolds.^[76] In addition, the V_2O_5 scaffolds' stress-strain curves exhibit a

pronounced linear elastic regime, making them interesting to be investigated in terms of their cyclic stability. Such a cyclic compression test result is displayed in figure 5.23a.

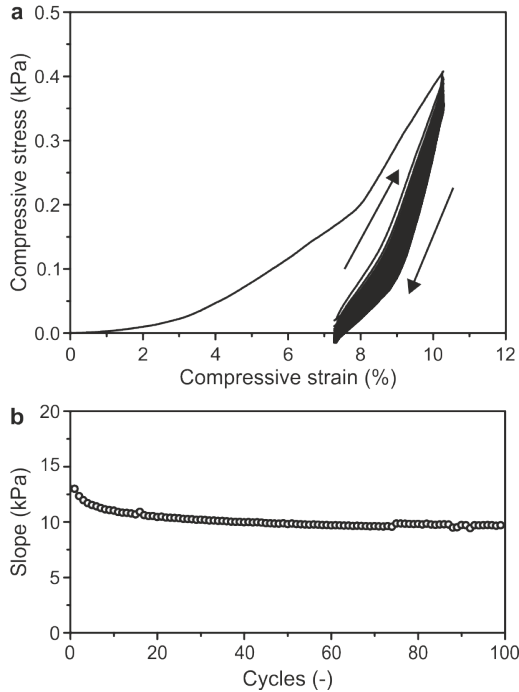


Figure 5.23: (a) Cyclic stress-strain curves of cuttlebone-like V_2O_5 -1. Displayed are 100 tested cycles, which show a reversible deformation of about 3%. (b) Corresponding slope of each cycle as a function of cycle number.

After an initial pre-load, the sample was cycled 100 times over a range of about 3% (between 7 and 10%). A comparable elastic deformation has been so far only observed in so-called structural metamaterials.^[138,143,144] Such materials are composed of periodically arranged hollow struts, assembled into three-dimensional nanolattices. Jang *et al.*^[143] reported about TiN nanolattices with a wall thickness (of the hollow struts) of 80 nm, (comparable to the lamella thickness of the V_2O_5 -2 scaffolds (84.6 ± 7.7 nm)), which resulted in partial reversible deformations between 1% and 1.5%. Compared to the cyclic deformation of the V_2O_5 -1 scaffold (lamella thickness of 58.0 ± 6.0 nm) presented in figure 5.23a, these values are inferior. Moreover, the cyclic stress-strain curves of the TiN

nanolattices exhibited a distinct remanent deformation after each cycle. They attributed this displacement offset to irreversible nanocracking of the ceramic struts within the nanolattices. In contrast, the V_2O_5 -1 scaffolds did not show such a pronounced offset along the x -axis, they only show minor, steady degradation, which resulted in an overlap of the cycles and a slight decrease in the slopes of the stress-strain curves (figure 5.23b). The use of flexible nanofibers, instead of more rigid hollow struts, makes the V_2O_5 scaffolds less brittle than the TiN nanolattices. However, the rigidity of the hollow struts can be decreased by downscaling their wall thickness, which then improves their reversibility, as reported for Al_2O_3 nanolattices.^[138] However, it has to be furthermore mentioned that the fabrication procedure for obtaining such nanolattices limits their sample size to be in the range of up to 100 μm , their field of possible application is also limited to the microscopic level. Alternatively, ice-templating of V_2O_5 nanofibers enables fabricating macroscopic samples, which allows applying such structural ceramics in macroscopic functional devices.

Complementary to the cyclic compression tests, SEM *in situ* mechanical deformation of a small volume within the V_2O_5 -1 scaffolds was conducted to visualize their elastic deformation. Figures 5.24a-c display the compression perpendicular to the lamella orientation. The top image (figure 5.24a) shows the initial scaffold right before deformation. Compressing the microstructure led to a bending of the pillars (figure 5.24b), which deform reversibly, as the load is removed, returning to its initial state (figure 5.24c). Analog to this deformation, figures 5.24d-f display the compression parallel to the lamella orientation, in which the lamellas appear to buckle. This mechanical deformation is likewise reversible. It therefore can be concluded that the mechanical flexibility of the V_2O_5 nanofibers is transferred to the macroscopic level. The reversible scaffold wall buckling reminds of the non-linear elastic buckling found in PU foams.^[76] Figure 5.25a displays the light microscope image of a conventional PU foam, revealing a random network of PU struts, which frame open pores of different size and shape. Such a foam exhibits a porosity of 98.3%, as calculated with the help of equation 5.1. The relative density of the foams accounted 0.017, when using the estimated density of PU ($1.18 g/cm^3$).^[145] Upon compression, the PU struts begin to elastically buckle, according to the scheme displayed in figure 5.25b, leading to a compacted microstructure (figure 5.25c). While compressing the PU foams is fully reversible, the V_2O_5 -1 scaffolds macroscopically

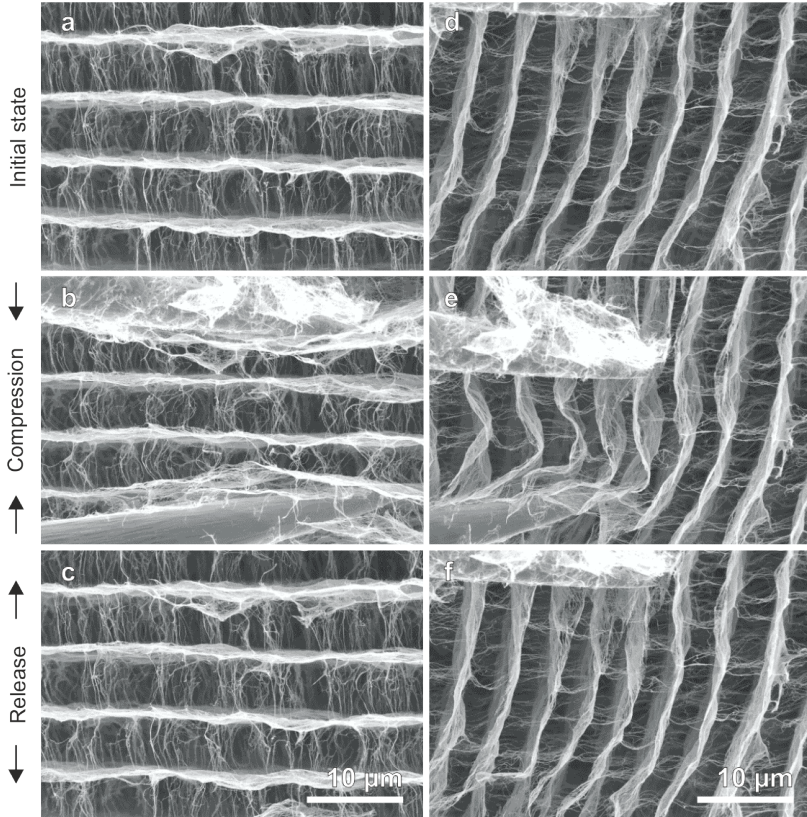


Figure 5.24: SEM images showing *in situ* mechanical deformation of a V_2O_5-1 scaffold, using two micromanipulators. (a-c) deformation with load applied perpendicular to the lamella orientation, (d-f) deformation with load applied parallel to the lamella orientation. In both cases, the upper images display the initial state before compression, the middle images display the actual compression and the bottom two images display the release, which results in a fully reversibly deformation.

only partially recover due to the irreversible deformation mechanisms described in section 5.2.4. Nevertheless, this finding qualifies the V_2O_5 -1 scaffolds to be a promising damping material, with a comparable viscoelastic response as PU foams.^[92,93] PU foams are famous for their high damping capacities, which enables to cushion an external mechanical impact.

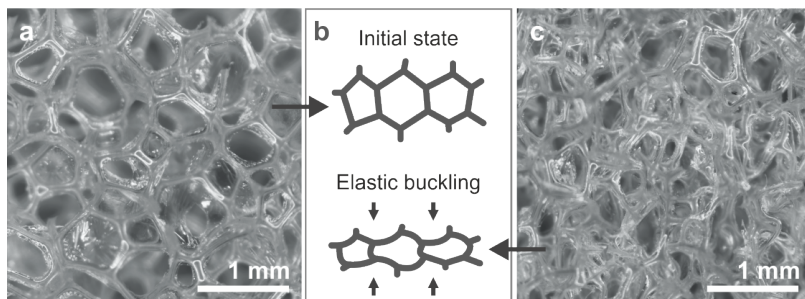


Figure 5.25: Light microscope images displaying (a) the microstructure of a conventional PU foam and (c) the same foam in compressed state. (b) Corresponding schematic microstructure (top) and elastic cell wall buckling upon compression (bottom), adapted from the drawing of Ashby.^[76]

5.4.2 Damping of PU foams

The viscoelastic behavior of a material can be investigated as a function of several parameters (section 3.5), including frequency and compressive strain. Figure 5.26a displays the storage and loss modulus of a PU foam at a fixed compressive strain, but variable frequency, while figure 5.26b displays the opposite case. Depending on the parameter, the absolute values and evolution of viscoelastic response strongly differ, making it important to simultaneously consider both parameters.

In order to get a more complete picture of the foams' viscoelastic behavior, the damping map is introduced (figure 4.6), which displays the viscoelastic response as a function of compressive strain and frequency (figure 5.27). According to figure 5.27a, it appears that the compressive strain has a larger impact on the storage modulus than the frequency (in the investigated range), which can be also extracted from figure 5.26. The compressive strain dependent values reach

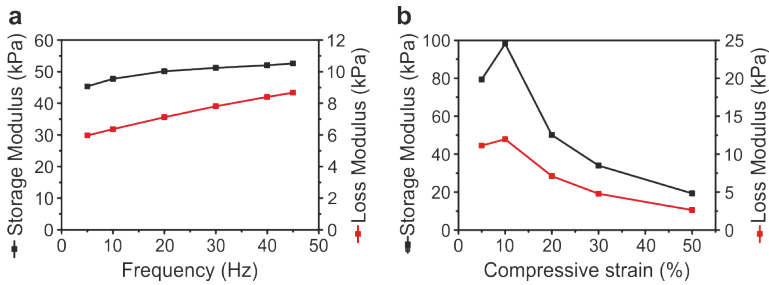


Figure 5.26: Storage and Loss modulus of PU (a) at 20% compressive strain as a function of frequency and (b) at 20 Hz frequency as a function of compressive strain.

a maximum at 10%, analog to the progression of PU's stress-strain curve (figure 5.27b). Below 10% compressive strain, the foams deform linear elastic under compressive load. Correspondingly, their storage modulus increases.^[92] However, when exceeding 10% compressive strain, the foam walls begin to buckle, as reflected in the drastically changing slope of the stress-strain curve. This buckling likewise reduces the storage modulus. The loss modulus shows a similar trend, but with up to one order of magnitude lower absolute values. This difference is attributed to the fact that the PU foams are fully elastic, leading to a far superior capability to elastically store energy rather than to dissipate it.

The frequency only shows a subordinated influence on storage and loss modulus (figures 5.26a and 5.27a,c). The slight increase in storage modulus with frequency (respectively strain rate) originates from variations in the foam's stiffness. At higher frequencies the scaffolds cannot instantly follow the applied oscillation, resulting in an increased stiffness, respectively in a higher Young's modulus. As the latter is in the same range as the initial storage modulus (at 0% compressive strain), also the storage modulus increases.^[92] Along this line, upon oscillation at higher frequencies, the response of the material tend to lack behind larger phase angles, which generates a larger hysteresis in the Lissajous figure (figure 3.8d).^[87] The area within the loop can be correlated to the damping capacity, therefore larger hysteresis yields a larger loss modulus.

Complementary to the maps of storage and loss modulus, figure 5.27d displays

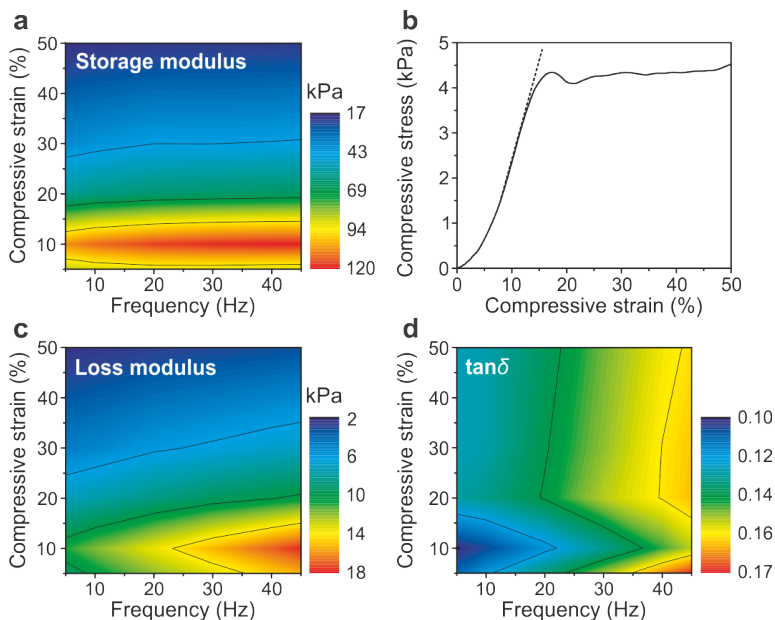


Figure 5.27: Color-scaled 2D maps showing the viscoelastic behavior of PU foams as a function of compressive strain and frequency: (a) Storage modulus, (b) corresponding stress-strain curve (c) loss modulus and (d) loss factor $\tan \delta$. This figure is adapted and reprinted with permission from Knöller *et al.*,^[118] Copyright 2018, American Chemical Society.

the loss factor $\tan \delta$, meaning the damping capacity, as a function of compressive strain and frequency. The map reveals a slight increase in $\tan \delta$ with increasing frequency, which can be explained by the individual trends of storage and loss modulus in figure 5.26a. The loss modulus increases slightly faster with frequency than the storage modulus. Owing to the fact that the loss factor is the ratio of loss to storage modulus, $\tan \delta$ also slightly increases. More pronounced is the prompt drop in $\tan \delta$ at 10% compressive strain, which can be explained with the help of figure 5.26b. At the end of the linear elastic regime (figure 5.26b), the storage modulus reaches its absolute maximum. This maximum is much more pronounced than the maximum of the loss modulus at the same compressive strain, yielding an opposing trend in $\tan \delta$. In general, all values are in the range of 0.10 and 0.17, which is in good agreement with damping capacities of previous reports.^[92,93]

5.4.3 Damping of V_2O_5 Scaffolds

Analog to the PU foams, viscoelastic measurements were conducted on the V_2O_5 scaffolds. Figures 5.28a-c display the damping maps of V_2O_5 -1 scaffolds. The scaffolds' storage and loss modulus exhibit a similar trend to what was found for PU foams (figure 5.27a). However, the V_2O_5 -1 scaffolds' storage moduli are much lower, while their loss moduli are in a similar range (comparing the color scales of figures 5.27a,c and 5.28a,b). In general, differences in storage and loss modulus can be related to the type of material, its microstructure as well as its density (respectively its porosity). The circumstance that the V_2O_5 -1 scaffolds exhibit much lower storage moduli than the PU foams, but similar loss moduli, most likely originates from two competing influencing factors. First, both materials show differences in porosity (PU 98.3% *vs.* V_2O_5 -1 99.8%), which has a tremendous impact on the absolute values along with the foams'/scaffolds' Young's modulus (figure 5.14b).^[76,92] The V_2O_5 scaffolds therefore should exhibit lower values, which they do only in case of the storage modulus. Second, the V_2O_5 -1 scaffolds are partially elastic (about 3%), in contrast to fully elastic PU foams, restricting the elastic portion of the V_2O_5 -1 scaffolds, but boosting the viscous (irreversible) portion, meaning the loss modulus. The latter leads to an increased loss to storage modulus ratio.

Besides differences in the absolute values, the storage modulus shows a shift in maximum values towards lower compressive strains (5%, figure 5.28a) than in PU foams (10%) as well as a broadening of the area with maximum values (red area) in the loss modulus map (figure 5.28b). Both findings can be explained with the help of the scaffolds' stress-strain curve (figure 5.13) The linear elastic regime ends at about 5% compressive strain, rendering the compression dependent storage modulus maximum, analog to the discussion for PU foams in the previous section 5.4.2. The increased area of loss modulus maxima at higher compressive strains than 5% originates from predominantly irreversible deformation in this region, giving rise to an increased energy dissipation, e.g. due to friction.^[86]

The frequency dependency of storage and loss modulus appears to be slightly more pronounced in the V_2O_5 -1 scaffolds than in the PU foams, indicated by the contour lines of the maps, which run more diagonally, especially in the case

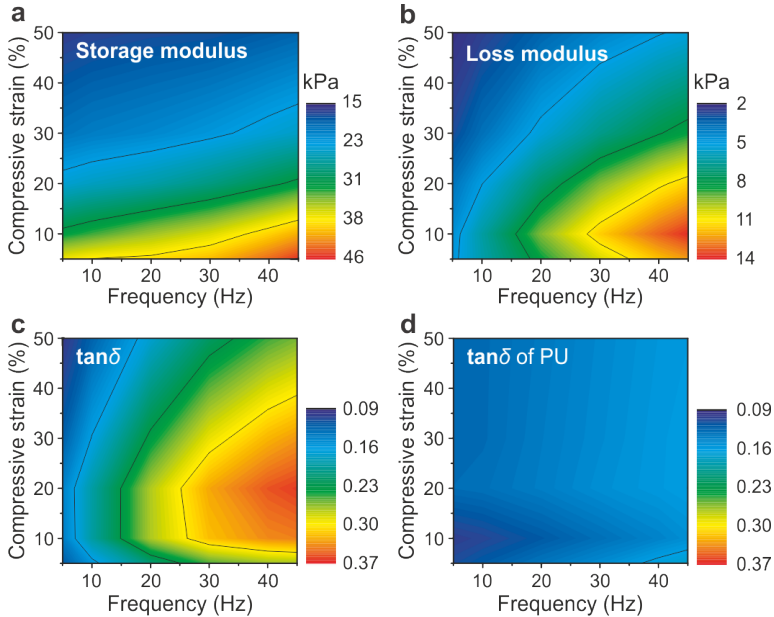


Figure 5.28: Color-scaled 2D maps showing the viscoelastic behavior of V_2O_5 -1 scaffolds: (a) Storage modulus, (b) loss modulus and (c) loss factor $\tan \delta$ as a function of compressive strain and frequency. (d) loss factor $\tan \delta$ of PU foams for direct comparison.

of the loss modulus (figure 5.28b). Two characteristics mainly contribute to a scaffold's vibrational behavior, identified as stiffness and mass.^[86] Ceramics are in general much harder and stiffer than elastomeric polymers, such as PU, which should lead to a vibration insensitivity of the V_2O_5 -1 scaffolds. However, owing to the higher porosity, respectively the lower mass, the V_2O_5 -1 scaffolds appear to be comparably more sensitive to vibrations than the softer PU foams. Figures 5.28c,d display the $\tan \delta$ maps of V_2O_5 -1 scaffolds and PU foams, respectively, using the same color scale for direct comparison. While the PU foams show only slight variations in $\tan \delta$ with values between 0.10 and 0.17, the V_2O_5 -1 scaffolds show a much larger variety of values with a maximum of 0.37 at 20% compressive strain and a frequency of 45 Hz. This maximum arises from the compression dependent offset of the storage and loss modulus peaks (5% vs. 10% compressive strain, respectively) coupled with a comparably more frequency sensitive loss modulus.

In order to evaluate if the trends of measured viscoelastic responses are only a matter of type material or also of microstructure, the viscoelastic measurements were repeated on the V_2O_5 -0 scaffolds, which served as reference sample in section 5.2.4. Figure 5.29 displays the corresponding damping maps. As the V_2O_5 -1 and V_2O_5 -0 scaffolds are prepared from the same material, even the same initial suspension, these scaffolds only differ in their microstructure (figure 5.13). According to the color scales, the V_2O_5 -0 scaffolds show lower values in storage and loss modulus than the V_2O_5 -1 scaffolds, which originates from the structure-related lower Young's modulus (table 5.2). Moroni *et al.*^[146] reported a similar observation in 3D fiber-deposited scaffolds. An increase in fiber spacing, which renders the pore size of their scaffolds, led to a decrease in storage modulus.

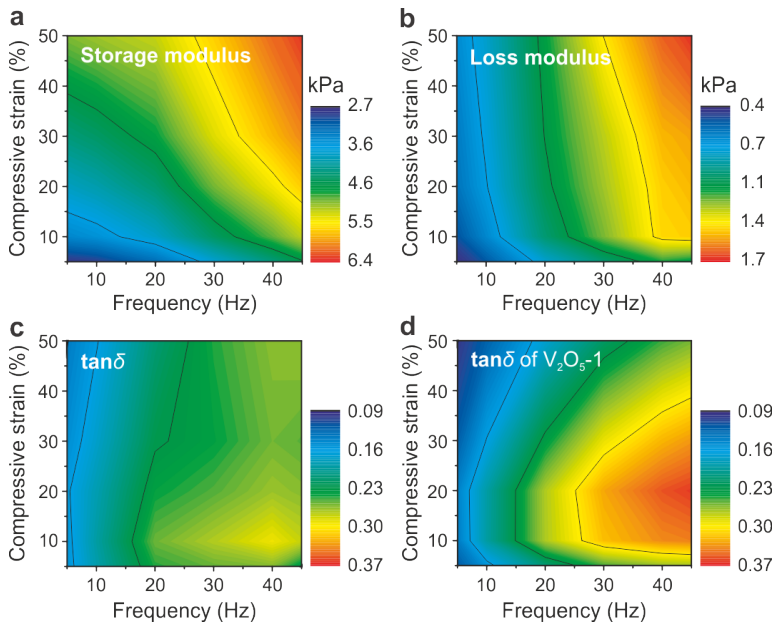


Figure 5.29: Color-scaled 2D maps showing the viscoelastic behavior of V_2O_5 -0 scaffolds: (a) Storage modulus, (b) loss modulus and (c) loss factor $\tan \delta$ as a function of compressive strain and frequency. (d) loss factor $\tan \delta$ of V_2O_5 -1 scaffolds for direct comparison.

More importantly, the V_2O_5 -0 scaffolds exhibit completely different trends in storage and loss modulus, compared to PU foams and V_2O_5 -1 scaffolds. The

storage modulus increases with compressive strain and frequency (figure 5.29a) to roughly the same extent, as indicated by the predominantly diagonal contour lines. The increase towards higher compressive strains can be correlated to the stress-strain curve of the V_2O_5 -0 scaffolds (figure 5.13), which does not exhibit a clear transition from the linear elastic regime to the irreversible deformation. The increase in storage modulus goes along with the rather smooth increase in stress. The pronounced frequency dependency can also be explained by the scaffolds' microstructure. As mentioned above, the mass and the stiffness contribute to a scaffold's vibrational behavior.^[86] The impact of the mass can be neglected, as it is the same for both, the V_2O_5 -1 and the V_2O_5 -0 scaffolds, but here the stiffness plays a major role. The V_2O_5 -0 scaffolds with their irregular scaffold walls, show inferior values in Young's modulus (table 5.2 and figure 5.13), making them more sensitive to vibrations, thus to the applied oscillation frequency. This sensitivity is also visible in the loss modulus map of the V_2O_5 -0 scaffolds (figure 5.29b). It appears that the frequency dependency outperforms the compression dependency, as illustrated by the predominantly vertical contour lines. The trends of viscoelastic responses are indeed a matter of type material and microstructure. Comparing the loss factor $\tan \delta$ maps of V_2O_5 -0 and V_2O_5 -1 scaffolds reveals a similar appearance, but the maximum value of the V_2O_5 -1 scaffolds (0.37) exceeds the one of the V_2O_5 -0 scaffolds (0.29) by about 28%. The damping capacity of a given material can therefore be tuned by external means, yielding structural damping.^[85]

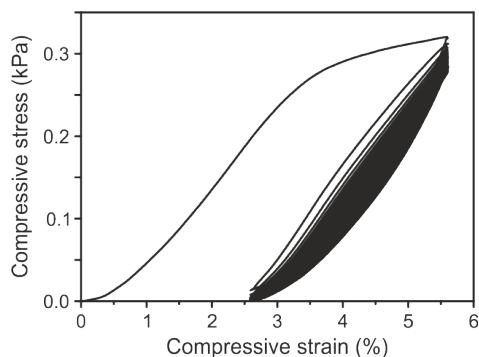


Figure 5.30: Cyclic stress-strain curves of a thermally post-treated cuttlebone-like V_2O_5 scaffold (V_2O_5 -1A). Displayed are 100 tested cycles, which still show a reversible deformation of about 3%. This figure is adapted and reprinted with permission from Knöller *et al.*^[118] Copyright 2018, American Chemical Society.

Complementing structural damping, the damping capacity can also be tuned by internal means, so-called material damping.^[85] In this context the thermally post-treated scaffolds V_2O_5 -1A were dynamically investigated. Figure 5.30 displays the cyclic stress-strain curve of such a scaffold, which exhibit a reversible deformation of about 3% similar to the untreated scaffolds V_2O_5 -1 (figure 5.23). This reversibility is likewise constant over all 100 tested cycles.

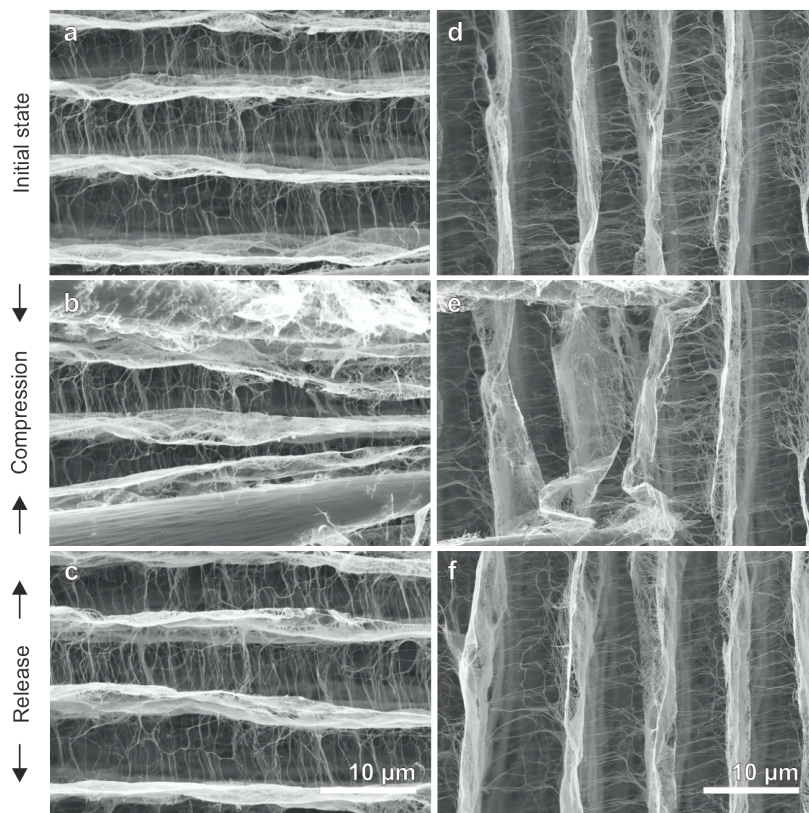


Figure 5.31: SEM images showing *in situ* mechanical deformation of a V_2O_5 -1A scaffold, using two micromanipulators. (a-c) deformation with load applied perpendicular to the lamella orientation, (d-f) deformation with load applied parallel to the lamella orientation. In both cases, the upper images display the initial state before compression, the middle images display the actual compression and the bottom two images display the release, which results in a fully reversibly deformation. This figure is adapted and reprinted with permission from Knöllner *et al.*,^[118] Copyright 2018, American Chemical Society.

In analogy, figure 5.31 displays the SEM *in situ* mechanical deformation of a V_2O_5 -1A scaffold, visualizing that the partial elastic deformation of scaffold is preserved upon thermal post-treatment. The phase pure scaffolds show the same bending of pillars and buckling of lamellas as the initial V_2O_5 -1 scaffolds. These observations follow the conclusion of section 5.3.3, that the removal of water has no significant influence on the flexibility of the scaffold walls, qualifying these annealed scaffolds to also exhibit a comparable damping behavior. Indeed, figure 5.32 displays the damping maps of the V_2O_5 -1A scaffolds, which exhibit strong similarities to the maps displayed in figure 5.28.

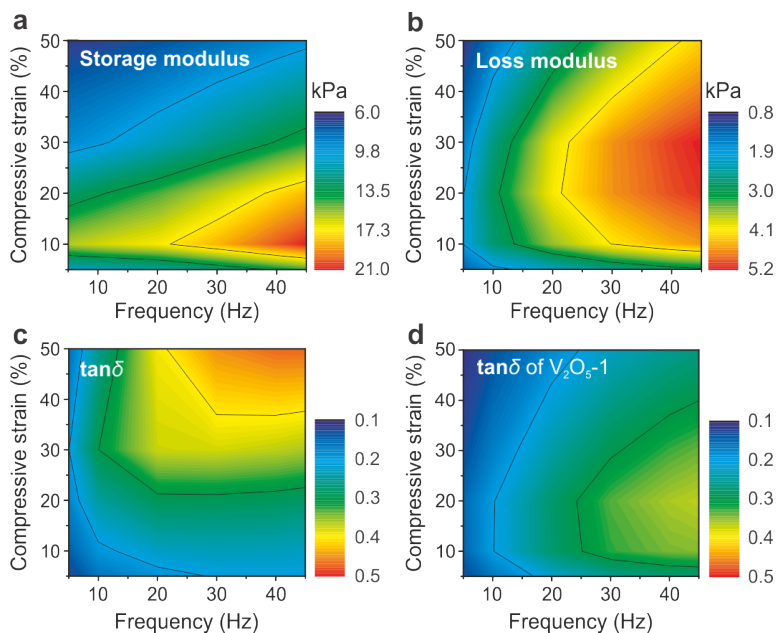


Figure 5.32: Color-scaled 2D maps showing the viscoelastic behavior of V_2O_5 -1A scaffolds: (a) Storage modulus, (b) loss modulus and (c) loss factor $\tan \delta$ as a function of compressive strain and frequency. (d) loss factor $\tan \delta$ of V_2O_5 -1 scaffolds for direct comparison. This figure is adapted and reprinted with permission from Knöller *et al.*,^[118] Copyright 2018, American Chemical Society.

However, the absolute values are lower, originating from the higher porosity of the post-treated samples (99.9%, section 5.3.3 *vs.* 99.8% of V_2O_5 -1). In addition, the maxima of storage and loss modulus appear to be shifted towards larger compressive strains. This shift correlates to the stress-strain curve of the

V_2O_5 -1A scaffolds, which shows a linear elastic regime up to about 10% compressive strain, compared to the 5% compressive strain of the V_2O_5 -1 scaffolds (figure 5.33). Ashby^[76] plotted the stress over the compressive strain of plastic (e.g. metal) foams, which exhibit variations in relative density. In the group of highly porous foams, they observed an elongation of the linear elastic regime with decreasing relative density, thus increasing porosity (figure 5.33). Similar tendencies seem to also apply in case of the V_2O_5 scaffolds.

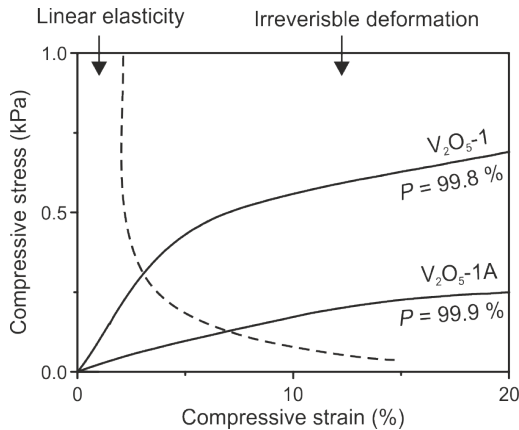


Figure 5.33: Stress-strain curves of a V_2O_5 -1A and a V_2O_5 -1 scaffold, revealing an elongation of the linear elastic regime with higher porosity, analog to the findings of Ashby (dashed line).^[76]

In addition to the shift of maxima, the loss modulus map (figure 5.32) has a larger area with maximum values (red area), implying a more pronounced energy dissipation. It can be assumed that breaking the fused nanofibers within the V_2O_5 -1A scaffolds (figure 5.21c) consumes more energy when the scaffold is being irreversibly deformed than the breaking the H-bonds within the V_2O_5 -1 scaffolds, as extracted from the DSC curve in section 5.3.2 (figure 5.19).

In contrast to the comparison of the V_2O_5 -1 and V_2O_5 -0 scaffolds, the more pronounced frequency sensitivity of the V_2O_5 -1A scaffolds (in comparison to V_2O_5 -1) is attributed only to the difference in mass. The impact of the stiffness of the scaffold walls can be neglected in this case, as the wall moduli of both scaffolds are alike (section 5.3.3). On the other hand, the impact of the mass is reflected in the samples' porosity, arising from the water loss of 13.47 wt%

and phase transformation upon thermal post-treatment (section 5.3.2). The V_2O_5 -0 scaffolds show inferior values in Young's modulus (table 5.2) due to the higher porosity, making them slightly more sensitive to the applied oscillation frequency. Consequently, the V_2O_5 -1A scaffolds show a shifted maximum area of the loss factor $\tan \delta$ towards higher compressive strains and a slight expansion towards lower frequencies (figures 5.32c,d) as well as an maximum value of up to 0.47, which is 27% higher than the one of the V_2O_5 -1 scaffolds. The damping capacity was therefore tunable also by internal means, yielding enhanced material damping.^[85]

5.4.4 Assessment of Damping Capacities

Owing to the fact that ceramics are typically poor damping materials, there is so far only limited work, which focuses on their damping capacities,^[85] but comparing the presented results to the damping capacities of other foams/scaffolds beyond PU foams would help classifying them. Figure 5.34 displays the assessment of $\tan \delta$ values of foams/scaffolds made from different material classes as well as their composite materials.^[89-93,137] It has to be mentioned that the damping capacities of the assessed materials were determined with different characterization tools, which allowed extracting the $\tan \delta$ as a function of different parameters, including composition, compressive strain, frequency or/and temperature. The compression- and frequency dependency of the PU foams (figures 5.26 and 5.27) already illustrated that the viscoelastic response of a given material can vary dependent on the chosen conditions. Hence, the boxes in the block diagram of figure 5.34 embody the range of all determined values. As the assessed foams/scaffolds vary in material, microstructure as well as measurement parameters, a direct comparison of the absolute values is difficult. However, figure 5.34 helps identifying the key parameters to design high damping materials and better judging the damping properties of the V_2O_5 scaffolds.

Due to the high intrinsic damping behavior of polymeric materials, PU and Al-PU foams show superior damping capacities,^[89,92,93] compared to most reported metal foams.^[89,90] Liu *et al.*^[89] impregnated aluminum foams with PU, leading to up to a five-fold improvement in the damping capacity with respect to

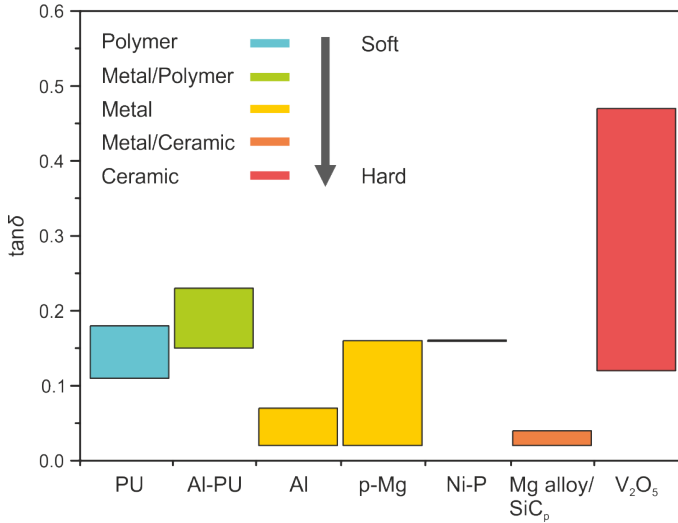


Figure 5.34: Assessment of the loss factor $\tan \delta$ of various scaffolds and foams made from different material classes (polymers, metals, ceramics).^[89–93,137] This figure is adapted and reprinted with permission from Knöller *et al.*,^[118] Copyright 2018, American Chemical Society.

the initial aluminum foam, thus taking advantage of the good material damping of PU. Metals and ceramics, on the other hand, usually show poor intrinsic/material damping behavior,^[85] as reflected in the comparably low $\tan \delta$ values of the highly porous Mg alloy/SiC_p foams (the p stands for particles) reported by Huang *et al.*^[91] In this case the measured $\tan \delta$ is mainly based on air damping. The impact of the medium (air, phosphate-buffered saline (PBS) and polyvinylpyrrolidone (PVP) solution) on the damping capacity was investigated by Moroni *et al.*,^[146] who conducted viscoelastic measurements on 3D fiber deposited block-copolymer scaffolds. They observed damping capacities of the scaffolds in air, which are up to doubled compared to the ones of the scaffolds in PBS or PVP, proving the superiority of air damping.

Although the Mg alloy/SiC_p foams^[91] are porous, they exhibit thick and dense cell walls, restricting pronounced structural damping effects besides air damping. However, the damping capacities of metals and ceramics can be tuned by fabricating more filigree microstructures, unlocking further damping effects, as in the case of metallic Ni-P microlattices.^[137] Cyclic measurements on these

Ni-P microlattices show a transition from metallic (plastic) deformation behavior towards full recovery upon increasing the porosity and reducing the wall thickness. Such fully reversible deformation reminds of the one of PU foams^[92] and also their damping capacities are in the same range (around $\tan \delta = 0.16$ in figure 5.34). The superior elastic portion (in comparison to energy dissipation), in both cases, inhibits obtaining larger damping capacities than the ones observed. In contrast, the here presented V_2O_5 scaffolds unite a filigree microstructure (structural damping), assembled from flexible nanofibers (material damping) and partial elastic deformation (enhanced energy dissipation). This combination yields all-ceramic scaffolds with exceptional viscoelastic properties, overcoming the brittleness and improving the damage tolerance of ceramics.

6 Conclusion

This dissertation addressed the bioinspired design of highly porous V_2O_5 scaffolds, using natural cuttlebone as role model, and the exploration of their microstructure, chemical composition, thermal stability as well as their mechanical properties.

The symbiosis of the chosen high-aspect ratio building blocks and the structuring protocol enables fabricating ceramic scaffolds, which resemble the microstructure of natural cuttlebone. This symbiosis arises from the perfect combination of the physics of ice, the freezing conditions, the chemistry of the system as well as the mechanical flexibility of the used V_2O_5 nanofibers, allowing the nanofibers to closely adapt the structural features given by the ice template. The resulting microstructure has regularly stacked lamellas, which are interconnected by numerous evenly distributed pillars. Analog to the structure-mechanics relation of natural cuttlebone, these cuttlebone-like V_2O_5 scaffolds exhibit an enhanced mechanical performance, as compared to V_2O_5 scaffolds with a random microstructure. Further tuning the structure can be achieved by increasing the V_2O_5 nanofiber concentration, which leads to an increase in strength and Young's modulus along with the increasing lamella thickness.

Owing to the chosen synthesis method, the V_2O_5 nanofibers exhibits a hydrated state, meaning water molecules being intercalated in the layered crystal structure. These water molecules represent the soft fraction of the system, analog to the presence of soft biopolymers in natural cuttlebone. Upon thermally post-treating the V_2O_5 scaffolds, this water can be removed, which is accompanied by a phase change towards phase pure V_2O_5 scaffolds. At the same time, it is achieved that the cuttlebone-like microstructure is preserved, thus also preserves the desired structure-mechanics relation of natural cuttlebone.

The choice of the high-aspect ratio V_2O_5 nanofibers not only allows fabricating such filigree and mechanically stable microstructures, but also introduces a certain mechanical flexibility to the scaffolds, which is atypical for most all-ceramic scaffolds. This anomaly renders the V_2O_5 scaffolds to be excellent mechanical dampers. In addition, their viscoelastic properties can be tuned by varying the microstructure, thermal post-treatment, compressive strain and the applied frequency. In all cases, the viscoelastic properties of the V_2O_5 scaffolds appear to outperform the ones of conventional PU foams by up to 300 %.

This work therefore successfully transfers the structure-mechanics relation of natural cuttlebone to a technically relevant system and simultaneously introduces a remarkable vibration resistance, laying the foundation for the development of long-living functional materials for various applications, including catalysis, sensing and energy storage.

Bibliography

- [1] AP Jackson, JFV Vincent, and RM Turner. The mechanical design of nacre. *Proceedings of the Royal Society of London B: Biological Sciences*, 234(1277):415–440, 1988.
- [2] M Sarikaya, KE Gunnison, M Yasrebi, and IA Aksay. Mechanical property-microstructural relationships in abalone shell. *MRS Online Proceedings Library Archive*, 174, 1989.
- [3] MA Meyers, P-Y Chen, AY-M Lin, and Y Seki. Biological materials: structure and mechanical properties. *Progress in Materials Science*, 53(1):1–206, 2008.
- [4] Z Burghard, L Zini, V Srot, P Bellina, PA van Aken, and J Bill. Toughening through nature-adapted nanoscale design. *Nano Letters*, 9(12):4103–4108, 2009.
- [5] F Barthelat. Nacre from mollusk shells: a model for high-performance structural materials. *Bioinspiration & biomimetics*, 5(3):035001, 2010.
- [6] Y Shao, H-P Zhao, X-Q Feng, and H Gao. Discontinuous crack-bridging model for fracture toughness analysis of nacre. *Journal of the Mechanics and Physics of Solids*, 60(8):1400–1419, 2012.
- [7] H Gao, B Ji, IL Jäger, E Arzt, and P Fratzl. Materials become insensitive to flaws at nanoscale: lessons from nature. *Proceedings of the National Academy of Sciences*, 100(10):5597–5600, 2003.
- [8] SE Naleway, JRA Taylor, MM Porter, MA Meyers, and J McKittrick. Structure and mechanical properties of selected protective systems in ma-

- rine organisms. *Materials Science and Engineering: C*, 59:1143–1167, 2016.
- [9] A Knöller, CP Lampa, F von Cube, TH Zeng, DC Bell, MS Dresselhaus, Z Burghard, and J Bill. Strengthening of ceramic-based artificial nacre *via* synergistic interactions of 1d vanadium pentoxide and 2d graphene oxide building blocks. *Scientific Reports*, 7:40999, 2017.
- [10] M Plötze and P Niemz. Porosity and pore size distribution of different wood types as determined by mercury intrusion porosimetry. *European Journal of Wood and Wood Products*, 69(4):649–657, 2011.
- [11] X Wang and Q Ni. Determination of cortical bone porosity and pore size distribution using a low field pulsed NMR approach. *Journal of Orthopaedic Research*, 21(2):312–319, 2003.
- [12] P-Y Chen and J McKittrick. Compressive mechanical properties of demineralized and deproteinized cancellous bone. *Journal of the Mechanical Behavior of Biomedical Materials*, 4(7):961–973, 2011.
- [13] UGK Wegst and MF Ashby. The mechanical efficiency of natural materials. *Philosophical Magazine*, 84(21):2167–2186, 2004.
- [14] JD Birchall and NL Thomas. On the architecture and function of cuttlefish bone. *Journal of Materials Science*, 18(7):2081–2086, 1983.
- [15] KM Sherrard. Cuttlebone morphology limits habitat depth in eleven species of sepia (cephalopoda: Sepiidae). *The Biological Bulletin*, 198(3):404–414, 2000.
- [16] J Cadman, S Zhou, Y Chen, W Li, R Appleyard, and Q Li. Characterization of cuttlebone for a biomimetic design of cellular structures. *Acta Mechanica Sinica*, 26(1):27–35, 2010.
- [17] J Cadman, C-C Chang, J Chen, Y Chen, S Zhou, W Li, and Q Li. Bioinspired lightweight cellular materials - understanding effects of natural variation on mechanical properties. *Materials Science and Engineering: C*, 33(6):3146 – 3152, 2013.

- [18] AG Checa, JHE Cartwright, I Sánchez-Almazo, JP Andrade, and F Ruiz-Raya. The cuttlefish *sepia officinalis* (sepiidae, cephalopoda) constructs cuttlebone from a liquid-crystal precursor. *Scientific Reports*, 5, 2015.
- [19] J Cadman, YH Chen, SW Zhou, and Q Li. Creating biomaterials inspired by the microstructure of cuttlebone. In *Materials Science Forum*, 2010.
- [20] A Knöller, T Runčevski, RE Dinnebier, J Bill, and Z Burghard. Cuttlebone-like V_2O_5 nanofibre scaffolds - advances in structuring cellular solids. *Scientific Reports*, 7:42951, 2017.
- [21] CMA Parlett, K Wilson, and AF Lee. Hierarchical porous materials: catalytic applications. *Chemical Society Reviews*, 42(9):3876–3893, 2013.
- [22] R Liu, T Xu, and C-A Wang. A review of fabrication strategies and applications of porous ceramics prepared by freeze-casting method. *Ceramics International*, 42(2, Part B):2907 – 2925, 2016.
- [23] M Ponzi, C Duschatzky, A Carrascull, and E Ponzi. Obtaining benzaldehyde *via* promoted V_2O_5 catalysts. *Applied Catalysis A: General*, 169(2):373–379, 1998.
- [24] SH Lim, BK Kim, and WY Yoon. Catalytic behavior of V_2O_5 in rechargeable Li-O₂ batteries. *Journal of Applied Electrochemistry*, 42(12):1045–1048, 2012.
- [25] JF Liu, X Wang, Q Peng, and Y Li. Vanadium pentoxide nanobelts: highly selective and stable ethanol sensor materials. *Advanced Materials*, 17(6):764–767, 2005.
- [26] S Wang, Z Lu, D Wang, C Li, C Chen, and Y Yin. Porous monodisperse V_2O_5 microspheres as cathode materials for lithium-ion batteries. *Journal of Materials Chemistry*, 21(17):6365–6369, 2011.
- [27] V Modafferi, G Panzera, A Donato, PL Antonucci, C Cannilla, N Donato, D Spadaro, and G Neri. Highly sensitive ammonia resistive sensor based on electrospun V_2O_5 fibers. *Sensors and Actuators B: Chemical*, 163(1):61–68, 2012.

- [28] A-M Cao, J-S Hu, H-P Liang, and L-J Wan. Self-assembled vanadium pentoxide (V_2O_5) hollow microspheres from nanorods and their application in lithium-ion batteries. *Angewandte Chemie International Edition*, 44(28):4391–4395, 2005.
- [29] H Wang, D Ma, Y Huang, and XB Zhang. Electrospun V_2O_5 nanostructures with controllable morphology as high-performance cathode materials for lithium-ion batteries. *Chemistry-A European Journal*, 18(29):8987–8993, 2012.
- [30] YN Ko, YC Kang, and SB Park. A new strategy for synthesizing yolk-shell V_2O_5 powders with low melting temperature for high performance Li-ion batteries. *Nanoscale*, 5(19):8899–8903, 2013.
- [31] D Su and G Wang. Single-crystalline bilayered V_2O_5 nanobelts for high-capacity sodium-ion batteries. *ACS Nano*, 7(12):11218–11226, 2013.
- [32] B Saravanakumar, Kamatchi K Purushothaman, and G Muralidharan. Interconnected V_2O_5 nanoporous network for high-performance supercapacitors. *ACS Applied Materials & Interfaces*, 4(9):4484–4490, 2012.
- [33] D Wei, MRJ Scherer, C Bower, P Andrew, T Ryhänen, and U Steiner. A nanostructured electrochromic supercapacitor. *Nano Letters*, 12(4):1857–1862, 2012.
- [34] RWG Wyckoff. *Crystal structures*, volume 2. Interscience New York, 1964.
- [35] V Petkov, PN Trikalitis, ES Bozin, SJL Billinge, T Vogt, and MG Kanatzidis. Structure of $V_2O_5 \cdot nH_2O$ xerogel solved by the atomic pair distribution function technique. *Journal of the American Chemical Society*, 124(34):10157–10162, 2002.
- [36] WY Ma, B Zhou, JF Wang, XD Zhang, and ZY Jiang. Effect of oxygen vacancy on Li-ion diffusion in a V_2O_5 cathode: a first-principles study. *Journal of Physics D: Applied Physics*, 46(10):105306, 2013.
- [37] MS Whittingham. Lithium batteries and cathode materials. *Chemical Reviews*, 104(10):4271–4302, 2004.

- [38] NA Chernova, M Roppolo, AC Dillon, and MS Whittingham. Layered vanadium and molybdenum oxides: batteries and electrochromics. *Journal of Materials Chemistry*, 19(17):2526–2552, 2009.
- [39] A Mukherjee, N Sa, PJ Phillips, A Burrell, J Vaughey, and RF Klie. Direct investigation of Mg intercalation into the orthorhombic V_2O_5 cathode using atomic-resolution transmission electron microscopy. *Chemistry of Materials*, 29(5):2218–2226, 2017.
- [40] Y Wang and G Cao. Developments in nanostructured cathode materials for high-performance lithium-ion batteries. *Advanced Materials*, 20(12):2251–2269, 2008.
- [41] J Livage. Vanadium pentoxide gels. *Chemistry of Materials*, 3:578–593, 1991.
- [42] BC Satishkumar, A Govindaraj, EM Vogl, L Basumallick, and CNR Rao. Oxide nanotubes prepared using carbon nanotubes as templates. *Journal of Materials Research*, 12(3):604–606, 1997.
- [43] B Li, Y Xu, G Rong, M Jing, and Y Xie. Vanadium pentoxide nanobelts and nanorolls: from controllable synthesis to investigation of their electrochemical properties and photocatalytic activities. *Nanotechnology*, 17(10):2560, 2006.
- [44] F Zhou, X Zhao, C Yuan, and L Li. Vanadium pentoxide nanowires: hydrothermal synthesis, formation mechanism, and phase control parameters. *Crystal Growth and Design*, 8(2):723–727, 2007.
- [45] M Zeng, H Yin, and K Yu. Synthesis of V_2O_5 nanostructures with various morphologies and their electrochemical and field-emission properties. *Chemical Engineering Journal*, 188:64–70, 2012.
- [46] J Livage. Sol-gel chemistry and electrochemical properties of vanadium oxide gels. *Solid State Ionics*, 86:935–942, 1996.
- [47] Z Burghard, A Leineweber, PA van Aken, T Dufaux, M Burghard, and

- J Bill. Hydrogen-bond reinforced vanadia nanofiber paper of high stiffness. *Advanced Materials*, 25:2468–2473, 2013.
- [48] K West, B Zachau-Christiansen, T Jacobsen, and S Skaarup. Thin-film vanadium oxide electrodes for lithium batteries. *Journal of Power Sources*, 43(1-3):127–134, 1993.
- [49] JR Szczech and S Jin. Nanostructured silicon for high capacity lithium battery anodes. *Energy & Environmental Science*, 4(1):56–72, 2011.
- [50] M Giorgetti, S Passerini, WH Smyrl, S Mukerjee, XQ Yang, and J McBreen. *In situ* X-ray absorption spectroscopy characterization of V_2O_5 xerogel cathodes upon lithium intercalation. *Journal of the Electrochemical Society*, 146(7):2387–2392, 1999.
- [51] G Sudant, E Baudrin, B Dunn, and J-M Tarascon. Synthesis and electrochemical properties of vanadium oxide aerogels prepared by a freeze-drying process. *Journal of The Electrochemical Society*, 151(5):A666–A671, 2004.
- [52] J Zhu, L Cao, Y Wu, Y Gong, Z Liu, HE Hoster, Y Zhang, S Zhang, S Yang, Q Yan, et al. Building 3d structures of vanadium pentoxide nanosheets and application as electrodes in supercapacitors. *Nano letters*, 13(11):5408–5413, 2013.
- [53] H Zhang, A Xie, C Wang, H Wang, Y Shen, and X Tian. Bifunctional reduced graphene oxide/ V_2O_5 composite hydrogel: fabrication, high performance as electromagnetic wave absorbent and supercapacitor. *ChemPhysChem*, 15(2):366–373, 2014.
- [54] Q Liu, Z-F Li, Y Liu, H Zhang, Y Ren, C-J Sun, W Lu, Y Zhou, L Stanciu, EA Stach, et al. Graphene-modified nanostructured vanadium pentoxide hybrids with extraordinary electrochemical performance for Li-ion batteries. *Nature Communications*, 6:6127, 2015.
- [55] A Moretti, F Maroni, I Osada, F Nobili, and S Passerini. V_2O_5 aerogel as a versatile cathode material for lithium and sodium batteries. *Chem-ElectroChem*, 2(4):529–537, 2015.

- [56] G Ye, Y Gong, K Keyshar, EAM Husain, G Brunetto, S Yang, R Vajtai, and PM Ajayan. 3d reduced graphene oxide coated V_2O_5 nanoribbon scaffolds for high-capacity supercapacitor electrodes. *Particle & Particle Systems Characterization*, 32(8):817–821, 2015.
- [57] K Zhu, C Zhang, S Guo, H Yu, K Liao, G Chen, Y Wei, and H Zhou. Sponge-like cathode material self-assembled from two-dimensional V_2O_5 nanosheets for sodium-ion batteries. *ChemElectroChem*, 2(11):1660–1664, 2015.
- [58] S Deville. Freeze-casting of porous ceramics: a review of current achievements and issues. *Advanced Engineering Materials*, 10(3):155–169, 2008.
- [59] E Munch, E Saiz, AP Tomsia, and S Deville. Architectural control of freeze-cast ceramics through additives and templating. *Journal of the American Ceramic Society*, 92(7):1534–1539, 2009.
- [60] L Qian and H Zhang. Controlled freezing and freeze drying: a versatile route for porous and micro-/nano-structured materials. *Journal of Chemical Technology and Biotechnology*, 86(2):172–184, 2011.
- [61] WL Li, K Lu, and JY Walz. Freeze casting of porous materials: review of critical factors in microstructure evolution. *International Materials Reviews*, 57(1):37–60, 2012.
- [62] J-H Song, Y-H Koh, H-E Kim, L-H Li, and H-J Bahn. Fabrication of a porous bioactive glass - ceramic using room-temperature freeze casting. *Journal of the American Ceramic Society*, 89(8):2649–2653, 2006.
- [63] S Deville, J Adrien, E Maire, M Scheel, and M Di Michiel. Time-lapse, three-dimensional *in situ* imaging of ice crystal growth in a colloidal silica suspension. *Acta Materialia*, 61(6):2077–2086, 2013.
- [64] PM Hunger, AE Donius, and UGK Wegst. Platelets self-assemble into porous nacre during freeze casting. *Journal of the mechanical behavior of biomedical materials*, 19:87–93, 2013.
- [65] X Xie, Y Zhou, H Bi, K Yin, S Wan, and L Sun. Large-range control of

- the microstructures and properties of three-dimensional porous graphene. *Scientific Reports*, 3, 2013.
- [66] A Abarrategi, MC Gutiérrez, C Moreno-Vicente, MJ Hortigüela, V Ramos, JL López-Lacomba, ML Ferrer, and F del Monte. Multiwall carbon nanotube scaffolds for tissue engineering purposes. *Biomaterials*, 29(1):94–102, 2008.
- [67] J Lee and Y Deng. The morphology and mechanical properties of layer structured cellulose microfibril foams from ice-templating methods. *Soft Matter*, 7(13):6034–6040, 2011.
- [68] S Deville. Ice-templating, freeze casting: Beyond materials processing. *Journal of Materials Research*, 28(17):2202–2219, 2013.
- [69] H Zhang, I Hussain, M Brust, MF Butler, SP Rannard, and AI Cooper. Aligned two- and three-dimensional structures by directional freezing of polymers and nanoparticles. *Nature Materials*, 4(10):787–793, 2005.
- [70] S Deville, E Saiz, RK Nalla, and AP Tomsia. Freezing as a path to build complex composites. *Science*, 311(5760):515–518, 2006.
- [71] J Chen, G Liu, and TW Button. Mechanical properties of porous TiO₂ ceramics fabricated by freeze casting process. *Advances in Applied Ceramics*, 112(7):436–441, 2013.
- [72] PM Hunger, AE Donius, and UGK Wegst. Structure-property-processing correlations in freeze-cast composite scaffolds. *Acta Biomaterialia*, 9(5):6338–6348, 2013.
- [73] H Bai, Y Chen, B Delattre, AP Tomsia, and RO Ritchie. Bioinspired large-scale aligned porous materials assembled with dual temperature gradients. *Science Advances*, 1(11), 2015.
- [74] R Zhang, B Han, D Fang, and Y Wang. Porous Y₂SiO₅ ceramics with a centrosymmetric structure produced by freeze casting. *Ceramics International*, 41(9):11517–11522, 2015.

- [75] X Liu, W Xue, C Shi, and J Sun. Fully interconnected porous Al_2O_3 scaffolds prepared by a fast cooling freeze casting method. *Ceramics International*, 41(9, Part B):11922 – 11926, 2015.
- [76] MF Ashby. The mechanical properties of cellular solids. *Metallurgical Transactions A*, 14(9):1755–1769, 1983.
- [77] R Hooke. *De potentia restitutiva, or of spring. Explaining the power of springing bodies*. London, UK: John Martyn, 1678.
- [78] AN Gent and AG Thomas. The deformation of foamed elastic materials. *Journal of Applied Polymer Science*, 1(1):107–113, 1959.
- [79] JM Lederman. The prediction of the tensile properties of flexible foams. *Journal of Applied Polymer Science*, 15(3):693–703, 1971.
- [80] LJ Gibson. *The elastic and plastic behaviour of cellular materials*. PhD thesis, University of Cambridge, 1981.
- [81] JB Walsh, WF Brace, and AW England. Effect of porosity on compressibility of glass. *Journal of the American Ceramic Society*, 48(12):605–608, 1965.
- [82] PH Thornton and CL Magee. Deformation characteristics of zinc foam. *Metallurgical and Materials Transactions A*, 6(9):1801–1807, 1975.
- [83] X Badiche, S Forest, T Guibert, Y Bienvenu, J-D Bartout, P Ienny, M Croset, and H Bernet. Mechanical properties and non-homogeneous deformation of open-cell nickel foams: application of the mechanics of cellular solids and of porous materials. *Materials Science and Engineering: A*, 289(1):276–288, 2000.
- [84] TG Nieh, K Higashi, and J Wadsworth. Effect of cell morphology on the compressive properties of open-cell aluminum foams. *Materials Science and Engineering: A*, 283(1):105–110, 2000.
- [85] J Zhang, RJ Perez, and EJ Lavernia. Documentation of damping capacity

- of metallic, ceramic and metal-matrix composite materials. *Journal of Materials Science*, 28(9):2395–2404, 1993.
- [86] DIG Jones. *Handbook of viscoelastic vibration damping*. John Wiley & Sons, 2001.
- [87] RS Lakes. *Viscoelastic materials*. Cambridge University Press, 2009.
- [88] BJ Lazan. Damping of materials and members in structural mechanics. *Pergamon Press LTD, Oxford, England*, 317, 1968.
- [89] S Liu, A Li, S He, and P Xuan. Cyclic compression behavior and energy dissipation of aluminum foam-polyurethane interpenetrating phase composites. *Composites Part A: Applied Science and Manufacturing*, 78:35–41, 2015.
- [90] Q Li, G Jiang, J Dong, J Hou, and G He. Damping behavior and energy absorption capability of porous magnesium. *Journal of Alloys and Compounds*, 680:522–530, 2016.
- [91] W Huang, H Luo, H Lin, Y Mu, and B Ye. Compressive behavior and damping property of Mg alloy/SiCp composite foams. *Journal of Materials Engineering and Performance*, 25(2):587–593, 2016.
- [92] S Basu. Quasi-static and dynamic compression behavior of flexible cellular material. *Agilent Technologies*, 2012.
- [93] F Scarpa, LG Ciffo, and JR Yates. Dynamic properties of high structural integrity auxetic open cell foam. *Smart Materials and Structures*, 13(1):49, 2003.
- [94] G Binnig, CF Quate, and C Gerber. Atomic force microscope. *Physical Review Letters*, 56(9):930, 1986.
- [95] G Kaupp. *Atomic force microscopy, scanning nearfield optical microscopy and nanoscratching: application to rough and natural surfaces*. Springer Science & Business Media, 2006.

-
- [96] P Eaton and P West. *Atomic force microscopy*. Oxford University Press, 2010.
- [97] D Rugar, HJ Mamin, P Guethner, SE Lambert, JE Stern, I McFadyen, and T Yogi. Magnetic force microscopy: General principles and application to longitudinal recording media. *Journal of Applied Physics*, 68(3):1169–1183, 1990.
- [98] D Sarid, R Coratger, F Ajustron, and J Beauvillain. Scanning force microscopy-with applications to electric, magnetic and atomic forces. *Microscopy Microanalysis Microstructures*, 2(6):649–649, 1991.
- [99] DF Ogletree, RW Carpick, and M Salmeron. Calibration of frictional forces in atomic force microscopy. *Review of Scientific Instruments*, 67(9):3298–3306, 1996.
- [100] JP Cleveland, B Anczykowski, AE Schmid, and VB Elings. Energy dissipation in tapping-mode atomic force microscopy. *Applied Physics Letters*, 72(20):2613–2615, 1998.
- [101] CW Oatley, WC Nixon, and RFW Pease. Scanning electron microscopy. *Advances in Electronics and Electron Physics*, 21:181–247, 1966.
- [102] R Reichelt. Scanning electron microscopy. In *Science of microscopy*, pages 133–272. Springer, 2007.
- [103] H Seiler. Secondary electron emission in the scanning electron microscope. *Journal of Applied Physics*, 54(11):R1–R18, 1983.
- [104] S Brunauer, PH Emmett, and E Teller. Adsorption of gases in multimolecular layers. *Journal of the American Chemical Society*, 60(2):309–319, 1938.
- [105] S Brunauer and L Copeland. Physical adsorption of gases and vapors on solids. In *Symposium on Properties of Surfaces*. ASTM International, 1963.
- [106] I Langmuir. The constitution and fundamental properties of solids and

- liquids. II. liquids. *Journal of the American Chemical Society*, 39(9):1848–1906, 1917.
- [107] I Langmuir. The adsorption of gases on plane surfaces of glass, mica and platinum. *Journal of the American Chemical Society*, 40(9):1361–1403, 1918.
- [108] G Fagerlund. Determination of specific surface by the BET method. *Materials and Structures*, 6(3):239–245, 1973.
- [109] AR Boccaccini and B Hamann. Review *in situ* high-temperature optical microscopy. *Journal of Materials Science*, 34(22):5419–5436, 1999.
- [110] F Raether, R Springer, and S Beyer. Optical dilatometry for the control of microstructure development during sintering. *Materials Research Innovations*, 4(4):245–250, 2001.
- [111] S-JL Kang. *Sintering: densification, grain growth and microstructure*. Butterworth-Heinemann, 2004.
- [112] S Gaisford, V Kett, and P Haines. *Principles of thermal analysis and calorimetry*. Royal Society of Chemistry, 2016.
- [113] J Lin, B Mishra, JJ Moore, and WD Sproul. A study of the oxidation behavior of CrN and CrAlN thin films in air using DSC and TGA analyses. *Surface and Coatings Technology*, 202(14):3272–3283, 2008.
- [114] HP Klug, LE Alexander, et al. *X-ray diffraction procedures*, volume 2. Wiley New York, 1954.
- [115] WH Bragg and WL Bragg. The reflection of X-rays by crystals. *Proceedings of the Royal Society of London. Series A, Containing Papers of a Mathematical and Physical Character*, 88(605):428–438, 1913.
- [116] J Brentano. Focussing method of crystal powder analysis by X-rays. *Proceedings of the Physical Society of London*, 37(1):184, 1924.

- [117] VK Pecharsky and PY Zavaliij. *Fundamentals of powder diffraction and structural characterization of materials*, volume 69. Springer, 2009.
- [118] A Knöller, S Kilper, AM Diem, M Widenmeyer, T Runčevski, RE Dinnebier, J Bill, and Z Burghard. Ultrahigh damping capacities in lightweight structural materials. *Nano Letters*, 2018.
- [119] SJ Park, JS Ha, YJ Chang, and GT Kim. Time dependent evolution of vanadium pentoxide nanowires in sols. *Chemical Physics Letters*, 390(1):199–202, 2004.
- [120] AR Bunsell, M-H Berger, and A Kelly. Fine ceramic fibers. *CRC Press*, pages 1–62, 1999.
- [121] CQ Chen and J Zhu. Bending strength and flexibility of ZnO nanowires. *Applied Physics Letters*, 90(4):043105, 2007.
- [122] Y-J Liu, JA Cowen, T Kaplan, DC DeGroot, J Schindler, CR Kannewurf, and MG Kanatzidis. Investigation of the alkali-metal vanadium oxide xerogel bronzes: $A_xV_2O_5 \cdot nH_2O$ ($A = K$ and Cs). *Chemistry of Materials*, 7(9):1616–1624, 1995.
- [123] B Vigolo, C Zakri, F Nallet, J Livage, and C Coulon. Detailed study of diluted V_2O_5 suspensions. *Langmuir*, 18(24):9121–9132, 2002.
- [124] S Deville, E Maire, G Bernard-Granger, A Lasalle, A Bogner, C Gauthier, J Leloup, and C Guizard. Metastable and unstable cellular solidification of colloidal suspensions. *Nature Materials*, 8(12):966–972, 2009.
- [125] V Fuentes-Landete, C Mitterdorfer, PH Handle, GN Ruiz, J Bernard, A Bogdan, M Seidl, K Amann-Winkel, J Stern, S Fuhrmann, et al. Crystalline and amorphous ices. *Water: Fundamentals as the Basis for Understanding the Environment and Promoting Technology*, 187:173, 2015.
- [126] B Wicklein, A Kocjan, G Salazar-Alvarez, F Carosio, G Camino, M Antonietti, and L Bergström. Thermally insulating and fire-retardant lightweight anisotropic foams based on nanocellulose and graphene oxide. *Nature Nanotechnology*, 10(3):277–283, 2015.

- [127] MV Naseh, AA Khodadadi, Y Mortazavi, OA Sahraei, F Pourfayaz, and SM Sedghi. Functionalization of carbon nanotubes using nitric acid oxidation and DBD plasma. *World Academy of Science, Engineering and Technology*, 49:177–179, 2009.
- [128] AP Roberts and EJ Garboczi. Elastic properties of model porous ceramics. *Journal of the American Ceramic Society*, 83(12):3041–3048, 2000.
- [129] CE Wen, Y Yamada, K Shimojima, Y Chino, H Hosokawa, and M Mabuchi. Compressibility of porous magnesium foam: dependency on porosity and pore size. *Materials Letters*, 58(3):357–360, 2004.
- [130] SJ Li, QS Xu, Z Wang, WT Hou, YL Hao, R Yang, and LE Murr. Influence of cell shape on mechanical properties of Ti-6Al-4V meshes fabricated by electron beam melting method. *Acta Biomaterialia*, 10(10):4537–4547, 2014.
- [131] G Gu, M Schmid, P-W Chiu, A Minett, J Fraysse, G-T Kim, S Roth, M Kozlov, E Munoz, and RH Baughmann. V_2O_5 nanofibre sheet actuators. *Nature Materials*, 2:316–319, 2003.
- [132] S Lin-Gibson, JA Cooper, FA Landis, and MT Cicerone. Systematic investigation of porogen size and content on scaffold morphometric parameters and properties. *Biomacromolecules*, 8(5):1511–1518, 2007.
- [133] P Arora, RE White, and M Doyle. Capacity fade mechanisms and side reactions in lithium-ion batteries. *Journal of the Electrochemical Society*, 145(10):3647–3667, 1998.
- [134] H Salmang, H Scholze, R Telle, et al. *Keramik*. Springer, 2007.
- [135] P Aldebert, N Baffier, N Gharbi, and J Livage. Layered structure of vanadium pentoxide gels. *Materials Research Bulletin*, 16(6):669 – 676, 1981.
- [136] JA Dean. Lange’s chemistry handbook. *University of Tennessee, Knoxville: McGrawHill, Inc*, 1999.

- [137] TA Schaedler, AJ Jacobsen, A Torrents, AE Sorensen, J Lian, JR Greer, L Valdevit, and WB Carter. Ultralight metallic microlattices. *Science*, 334(6058):962–965, 2011.
- [138] LR Meza, S Das, and JR Greer. Strong, lightweight, and recoverable three-dimensional ceramic nanolattices. *Science*, 345(6202):1322–1326, 2014.
- [139] TM Tillotson and LW Hrubesh. Transparent ultralow-density silica aerogels prepared by a two-step sol-gel process. *Journal of Non-crystalline Solids*, 145:44–50, 1992.
- [140] JF Poco, JH Satcher, and LW Hrubesh. Synthesis of high porosity, monolithic alumina aerogels. *Journal of Non-crystalline Solids*, 285(1):57–63, 2001.
- [141] N Kröger. Prescribing diatom morphology: toward genetic engineering of biological nanomaterials. *Current Opinion in Chemical Biology*, 11(6):662–669, 2007.
- [142] WJ Robinson and RM Goll. Fine skeletal structure of the radiolarian callimitra carolotae haeckel. *Micropaleontology*, pages 432–439, 1978.
- [143] D Jang, LR Meza, F Greer, and JR Greer. Fabrication and deformation of three-dimensional hollow ceramic nanostructures. *Nature Materials*, 12(10):893–898, 2013.
- [144] LR Meza, AJ Zelhofer, N Clarke, AJ Mateos, DM Kochmann, and JR Greer. Resilient 3d hierarchical architected metamaterials. *Proceedings of the National Academy of Sciences*, 112(37):11502–11507, 2015.
- [145] F Saint-Michel, L Chazeau, J-Y Cavallé, and E Chabert. Mechanical properties of high density polyurethane foams: I. effect of the density. *Composites Science and Technology*, 66(15):2700–2708, 2006.
- [146] Lorenzo Moroni, JR De Wijn, and CA Van Blitterswijk. 3d fiber-deposited scaffolds for tissue engineering: influence of pores geometry and architecture on dynamic mechanical properties. *Biomaterials*, 27(7):974–985, 2006.

Danksagung

Zu allererst möchte ich mich herzlich bei meinem Doktorvater Prof. Dr. Joachim Bill bedanken, dass er mir die Möglichkeit gegeben hat unter seiner Leitung diese Arbeit zu realisieren und mich in meinem Vorhaben stets unterstützt hat. Auch für meinen Auslandsaufenthalt am MIT in Boston konnte ich auf seiner Hilfe zählen. Das hat mir viel bedeutet. Des Weiteren möchte ich Prof. Dr. Siegfried Schmauder und Prof. Dr. Thomas Schleid danken, dass sie den Mitbericht bzw. den Prüfungsvorsitz von meinem Prüfungsausschuss übernommen haben.

Ich möchte zudem allen Stipendiengebern danken, dass sie mir diese Arbeit finanziell gesichert haben. Dazu zählen die Landesgraduiertenförderung, die DFG, der DAAD sowie die IMPRS-AM unter der Leitung von Dr. Hans-Georg Libuda.

Ich danke auch allen Kollegen und Kollaborationspartnern, die mich bei der Umsetzung dieser Arbeit unterstützt haben, insbesondere Prof. Dr. Jürgen Weis und Prof. Dr. Joachim Spatz, die mir Zugang zu ihren Messgeräten gewährt haben, Prof. Dr. Robert Dinnebieer und Frank Adams für die XRPD Messungen, Dr. Marc Widenmeyer für die TGA/DSC Messungen, Annette Fuchs für die BET Messungen, Dr. Holger Pfaff für die Bereitstellung der Dämpfungstestmethode, Traugott Wörner, Bernhard Fenk, Ulrike Waizmann, Ioanis Grigoridis, Samir Hammoud, Ivan Kozmon und Martin Schweizer für ihren meist technischen Support, Juliane Kränzl für ihre administrative Unterstützung, Sven Schildt fürs Bilder machen und Dr. Marko Burghard fürs Korrektur lesen. Vielen Dank auch an die ganzen anderen Kollegen vom Lehrstuhl 3, die mich in dieser Zeit begleitet haben.

Vier Personen, die mich ebenfalls bei der Umsetzung dieser Arbeit unterstützt haben, und zudem über die Jahre enge Freunde geworden sind, möchte ich

besonders danken: Meinen drei Musketiere Tim Jahnke, Achim Diem und Stefan Kilper, für ein super Teamwork bei der Arbeit und die viele schöne Abende und Urlaube außerhalb der Institutswände. Und, Dr. Tomče Runčevski, meinen alten Mitbewohner und Bruder, den ich nie hatte (und nie wollte).

Genauso wichtig wie die fachliche Unterstützung, ist der seelische und moralische Rückhalt. Daher danke ich meiner Familie und meinen Freunden, dass sie mich in der ganzen Zeit in jeglicher Form unterstützt und mir den nötigen Ausgleich zur Arbeit verschafft haben.

Last, but not least: Der größte Dank gilt Dr. Žaklina Burghard, für die ich bereits ab 2009 als Hiwi Studentin gearbeitet habe, die meine Diplomarbeit betreut hat und nun auch meine Dissertation. Über die Jahre ist sie für mich nicht nur auf wissenschaftlicher Ebene eine super Betreuerin gewesen, sondern wurde auch persönlich zu einer wichtigen Bezugsperson für mich. Ich habe viel von ihr gelernt, sie hat sich immer für mich eingesetzt, wir hatten unzählige fachliche Diskussionen, gute persönliche Gespräche, tolle gemeinsame Konferenzen und sie hatte stets ein paar Kekse oder Äpfel für uns parat.

Danke für diese tolle Zeit! Živeli!